



University of  
Stavanger

Faculty of Science and Technology

## MASTER'S THESIS

Study program/ Specialization:

Konstruksjoner og Materialer -  
Maskinkonstruksjoner

Spring semester, 2014

Open / Restricted access

Writer: Vegard Øien

.....  
(Writer's signature)

Faculty supervisor: Vidar Hansen

External supervisor: Atle Sjølyst-Kverneland

Thesis title:

**“Effect of Electron Beam Welding on the  
Microstructure and Mechanical Properties of Nickel Alloys”**

Credits (ECTS): 30

Key words:

*Electron Beam Welding*

*Ni-base Superalloy*

*Inconel 718*

*Custom Age 625 PLUS*

Pages: 63

+ enclosure: 15

Stavanger, .....

Date/year

## **Abstract**

The effect of electron beam welding on the precipitation strengthened Ni-base superalloys Inconel 718 and Custom Age 625 PLUS have been investigated. Solidification of the weld metal in these alloys terminates in a eutectic formation of  $\gamma$ /Laves in the interdendritic constituents. The formation is associated with the strong segregation behavior of the alloying element Nb during solidification. Post-weld heat treatments in the form of solution annealing and age hardening are normally used to dissolve the detrimental Laves phase and to restore the principal strengthening precipitate  $\gamma''$  in the weld metal. The use of heat treatments was omitted in the first part of the investigation in order to examine the alloys as-welded.

The weldability of Custom Age 625 PLUS was shown to be superior to Inconel 718. The amount of interdendritic constituents was estimated to be twice as high in Inconel 718. In addition, HAZ liquation cracks were found in the entire length of the weld, increasing in severity near the top of the weld bead in the “nail head” area. No evidence of cracking was found in the weld metal or HAZ of Custom Age 625 PLUS.

The superior weldability of Custom Age 625 PLUS resulted in 73% higher average tensile strength of the weld metal compared with Inconel 718. Ductile fracture of the tensile specimens was observed for both alloys. However, fractographic examinations revealed higher amounts of plastic deformation of the intervoid material of Custom Age 625 PLUS before fracture.

Post-weld heat treatments were performed subsequent to the initial investigation. The best response to both solution annealing and aging was found in Inconel 718 by the dissolution of most of the original weld metal constituents and a larger increase in weld metal hardness without any loss of base metal hardness. A distinct loss in base metal hardness was observed in Custom Age 625 PLUS.

## **Acknowledgement**

I want to express my gratitude to my professor Vidar Hansen. Vidar has been a tremendous help during most of my years at the University of Stavanger, as both a professor and supervisor for my Bachelor's and Master's thesis.

I would also like to thank my supervisor Atle Sjølyst-Kverneland. I benefited a great deal from the insights of the practical approaches to material investigations as well as the discussions surrounding the metallurgy of these alloys.

Ingunn Cecilie Oddsen's knowledge on metallurgical analyses is a great asset to this university. Fortunately her dedication for working with the scanning electron microscope exceeds her patience with it.

The employees at Quality Lab and Roxar have been helpful and professional in the process of aiding me in this dissertation. I wish both companies the best of luck in their future endeavors.

## Table of Contents

1.	Introduction.....	1
2.	Theory .....	3
2.1	Physical Metallurgy .....	3
2.1.1	Principal strengthening precipitates, $\gamma''$ and $\gamma'$ .....	3
2.1.2	$\delta$ -Phase .....	4
2.1.3	Laves Phase .....	6
2.1.4	Carbides.....	7
2.2	Weld Metallurgy.....	8
2.2.1	Solidification of Weld Metal.....	8
2.2.2	Solidification Cracking .....	10
2.2.3	HAZ Liquation Cracking .....	11
2.2.4	Post-Weld Heat Treatments .....	12
2.3	Electron Beam Welding.....	13
2.3.1	Electron Beam Welding Components .....	14
2.3.2	Mechanism of Welding .....	15
2.3.3	Welding Parameters .....	16
2.4	Fracture Mechanics.....	17
2.4.1	Ductile Fracture.....	18
2.4.2	Brittle Fracture .....	23
2.5	Corrosion .....	24
2.5.1	Crevice Corrosion .....	25
2.5.2	Pitting Corrosion .....	26
2.5.3	Ferric Chloride Solution Corrosion Test (ASTM G48).....	27
3	Experimental.....	28
3.1	Welding Procedures.....	29
3.2	Tensile and Corrosion Tests .....	32
3.3	Fractographic and Metallographic Preparation .....	32
3.4	Fractographic and Metallographic Analyses .....	33
3.5	Post-Weld Heat Treatments.....	35
4	Results.....	37
4.1	Corrosion Test .....	37
4.2	Tensile Tests and Fractographic Analysis .....	37
4.3	Microstructural Analysis .....	42



4.3.1	Base Metal .....	42
4.3.2	Weld Metal .....	46
4.3.3	Heat Affected Zone .....	50
4.4	Effect of Post-Weld Heat Treatments .....	53
5	Discussion .....	57
5.1	Tensile Tests and Fractographic Analysis .....	57
5.2	Microstructural Analysis .....	57
5.3	Effect of Post-Weld Heat Treatments .....	60
5.4	Suggestions for Further Work .....	60
6	Conclusion .....	61
7	References .....	62
Appendix A: Material Certificates .....		i
Inconel 718 .....		i
625 PLUS .....		iii
Appendix B: Schematic Drawings of Specimen Components .....		iv
Tensile Specimen Components .....		iv
Corrosion Specimen Components .....		vi
Appendix C: Fractographic Examination .....		viii
Fracture Paths .....		viii
Fractographs .....		x
Appendix D: Microstructural Analysis .....		xii
Inconel 718 .....		xii
625 PLUS .....		xiii
Appendix E: Vickers Hardness Measurements .....		xv

## List of Figures

Figure 1-1: HM/HS Gauge. Image courtesy of Roxar.....	1
Figure 2-1: TTT diagram for Inconel 718 [2]. .....	4
Figure 2-2: Needle shaped acicular $\delta$ -phase decorating the grain boundaries, extending into the grains of Inconel 718 [11]. .....	5
Figure 2-3: Fine globular $\delta$ -phase decorating the grain boundaries of Inconel 718 [12]. .....	5
Figure 2-4: Laves phase in a eutectic formation with $\gamma$ -austenite after solidification [13]. .....	6
Figure 2-5: Carbides at the grain boundaries in a superalloy [2]. .....	7
Figure 2-6: Solidification diagram of superalloys [2]. .....	8
Figure 2-7: Interdendritic structure containing eutectic $\gamma$ /Laves in the weld metal of Inconel 718 [12]. .....	9
Figure 2-8: Solidification crack in the weld metal of a superalloy [2]. .....	10
Figure 2-9: Liquation cracks in the grain boundaries in the HAZ of gas-tungsten-arc welded Inconel 718 [4].	11
Figure 2-10: HAZ liquation cracking mechanism in Inconel 718 [2]. .....	11
Figure 2-11: Schematic view of the electron gun [22]. .....	14
Figure 2-12: Forces maintaining the shape of the keyhole [18]. .....	15
Figure 2-13: Thermocapillary flow around keyhole [23]. .....	16
Figure 2-14: Void nucleation by a) decohesion in the particle-matrix interface, b) cracking of particle, c) decohesion of an interface associated with shear deformation or grain boundary sliding [26]. .....	18
Figure 2-15: Mechanism of ductile fracture via a) inclusions, b) void nucleation, c) void growth, d) strain on the material between voids, e) necking in the intervoid material and f) coalescence of voids leading to fracture [25]. .....	19
Figure 2-16: Mechanism leading to cup-and-cone fracture in a tensile specimen in steps of a) void nucleation, b) void coalescence and c) fracture by separation of the “shear lips” [26]. .....	20
Figure 2-17: Fractograph showing spherical dimples characteristic of ductile fracture [24]. .....	21
Figure 2-18: Fractograph of weld metal in Inconel 718 showing a dendritic fracture pattern [17]. .....	22
Figure 2-19: Fractographic image of a cleavage fracture [24]. .....	23
Figure 2-20: Illustrating a full electrochemical cell [27]. .....	24
Figure 2-21: Crevice corrosion[28]. .....	25
Figure 3-1: Tensile specimen components. ....	29
Figure 3-2: Corrosion specimen components. ....	29
Figure 3-3: Tensile specimen after electron beam welding and drilling of the weld root. The metal plug is inserted into the hollow end. ....	30
Figure 3-4: Corrosion specimen after electron beam welding. ....	31
Figure 3-5: Image of a) Fractographic specimen and b) Microstructure specimen. ....	33
Figure 3-6: Zones and points of indentations for Vickers hardness tests. ....	35
Figure 4-1: Fracture path of 625 PLUS No. 1. ....	38
Figure 4-2: Cup-and-cone fracture of 625 PLUS No. 2. ....	39
Figure 4-3: Fracture of shear lips 45° to applied tension in Inconel 718 No. 2. ....	39
Figure 4-4: Fractograph of Inconel 718 No. 2. ....	40
Figure 4-5: Fractograph of 625 PLUS No. 1. ....	40
Figure 4-6: Base metal of Inconel 718 No. 3. ....	43
Figure 4-7: Base metal of 625 PLUS No. 3. ....	43
Figure 4-8: Nb-rich MC carbide in 718 Inconel No. 3. ....	44
Figure 4-9: Fine globular $\delta$ -phase at grain boundary in Inconel 718 No. 3. ....	45
Figure 4-10: Weld metal of Inconel 718 No. 4. ....	46
Figure 4-11: Weld metal of 625 PLUS No. 4. ....	46
Figure 4-12: Constituents found in the weld metal of Inconel 718 No. 4. ....	48
Figure 4-13: Constituents found in the weld metal of 625 PLUS No. 4. ....	48
Figure 4-14: HAZ liquation cracks in Inconel 718 No. 4. ....	50

Figure 4-15: HAZ liquation cracks in Inconel 718 No. 4. ....	51
Figure 4-16: HAZ/weld metal interface of 625 PLUS No. 4. ....	52
Figure 4-17: Inconel 718 No. 3 weld metal before post-weld heat treatments. ....	54
Figure 4-18: Inconel 718 No. 3 weld metal after post-weld heat treatments. ....	54
Figure 4-19: 625 PLUS No. 3 weld metal before post-weld heat treatments. ....	55
Figure 4-20: 625 PLUS No. 3 weld metal after post-weld heat treatments. ....	55

## List of Tables

Table 2-1: Main alloying elements (wt %) in Inconel 718 and 625 PLUS [1, 2]. ....	3
Table 2-2: Elements partitioning in carbides [2]. ....	7
Table 3-1: Chemical composition (wt%) of the alloys investigated. ....	28
Table 3-2: As-delivered mechanical properties of the alloys investigated. ....	28
Table 3-3: List of tensile and corrosion specimens. ....	30
Table 3-4: Welding parameters for radial butt welds used on tensile and corrosion specimens. ....	30
Table 3-5: Welding parameters for axial butt welds used on corrosion specimens. ....	31
Table 3-6: Test parameters of the ASTM G48 ferric chloride solution corrosion test. ....	32
Table 3-7: List of microetchants used for metallographic preparation. ....	32
Table 4-1: Results of ASTM G48 ferric chloride corrosion test. ....	37
Table 4-2: Results from tensile tests. ....	37
Table 4-3: X-ray analysis of the major partitioning elements (wt%) in MC particles. ....	44
Table 4-4: Estimated area fraction of interdendritic constituents. ....	47
Table 4-4: Chemical composition (at%) of the dendritic and interdendritic constituents in Inconel 718. ....	49
Table 4-5: Chemical composition (at%) of the dendritic and interdendritic constituents in 625 PLUS. ....	49
Table 4-6: Segregation Coefficients for Nb. ....	50
Table 4-8: Chemical composition (at%) of the HAZ liquation crack constituents. ....	51
Table 4-9: Effect of post-weld heat treatments on the hardness of Inconel 718. ....	56
Table 4-10: Effect of post-weld heat treatments on the hardness of 625 PLUS. ....	56

## 1 Introduction

Monitoring of down-hole temperature and pressure is important in order to ensure ideal performance of wells in the petroleum industry. The information is used to optimize oil recovery, accelerate production rate and reduce the risk of unplanned shutdowns. Roxar's Permanent Down-hole Monitoring Systems (PDMS) is developed for continuous, real-time measurements of the conditions down-hole in production- or injection wells.

A vital component of this system is the HM/HS Gauge, seen in Figure 1-1. The instrument is installed in the lower part of the well to measure and transmit information regarding temperature and pressure. Longevity is a requirement as the instrument is designed to function the entire lifetime of a well. A notable application is the permanent installation of the HM/HS Gauge at Statoil's Gullfaks C production platform, where the instrument has been operating since 1990.



*Figure 1-1: HM/HS Gauge. Image courtesy of Roxar.*

The work environment of the HM/HS Gauge is characterized by high pressure, and temperatures can reach 225°C. The instrument may be used in “sour service” wells, containing significant amounts of corrosive compounds such as chlorides and sulfides. Materials used in these inhospitable environments are required to have exceptional mechanical properties and corrosion resistance at elevated temperatures.

Alloys known as “superalloys” are commonly used in down-hole instruments. Superalloy is a term used for nickel-base alloys that is precipitation strengthened by age hardening. They exhibit excellent strength and corrosion resistance at higher temperatures [1]. The principal precipitation strengthening phases in these alloys are  $\gamma'$  and  $\gamma''$  that forms in the  $\gamma$ -austenite matrix after aging. Although the superalloys are generally known for having good weldability, post-weld heat treatments are required to dissolve undesirable secondary phases and restore

the strengthening phases in the weld metal [2, 3]. Hence, most studies conducted on these alloys are on samples that have received some form of post-weld heat treatment.

The use of post-weld heat treatments is restricted in our case as the required temperatures will damage the electronic components installed within the HM/HS Gauge. Electron beam welding is used to seal the instrument with the electronics inside. Performance of alloys as-welded needs to be evaluated to find the most suitable candidate.

One of the most commonly used superalloys across various sectors is Inconel 718 (UNS N07718). Its introduction represented a major advancement in nickel-base superalloys because of its high resistance to cracking during post-weld heat treatments, a common problem in earlier superalloys [4]. The alloy exhibits high corrosion resistance and tensile strength at higher temperatures. The general weldability is known to be good as a result of the sluggish precipitation kinetics of its principal strengthening phase,  $\gamma''$  [3]. However, use of Inconel 718 is limited to sour service at moderate temperatures and in the absence of free sulfur [5]. The alloy is currently used in HM/HS Gauges produced by Roxar.

Custom Age 625 PLUS Alloy (UNS N07716), from here referred to as 625 PLUS, is proposed as an alternative to Inconel 718 for use in the HM/HS Gauge. The alloy is a derivative of the well-known Alloy 625. However, unlike its derivative, it is age hardenable and does not require cold work to obtain its high strength. As in Inconel 718, age hardening is used to form the alloys principal strengthening phase,  $\gamma''$ . The resistance to stress-corrosion cracking, pitting and crevice corrosion of 625 PLUS is known to be superior to Inconel 718 [1]. The tensile strength and hardness of the two alloys investigated are equivalent. However, the weldability of 625 PLUS is known to be preferable to Inconel 718 as a result of the low volume fraction of eutectic constituents in the weld metal [6].

The scope of this dissertation is to investigate electron beam welded Inconel 718 and 625 PLUS in the as-welded condition. Comparisons are made with respect to microstructure, mechanical properties and corrosion resistance to find the most suitable alloy in a case where the use of post-weld heat treatments is restricted. Post-weld heat treatments were conducted after the examination of the alloys as-welded in order to evaluate the effect of solution annealing and aging on the two alloys.

## 2 Theory

### 2.1 Physical Metallurgy

Ni-base superalloys consist of a  $\gamma$ -austenite matrix with an FCC crystal structure. The main reason for using Ni as a base is the elements ability to hold high concentrations of alloying elements in a solid-solution, due to its nearly filled third electron shell [7]. Superalloys are typically highly alloyed with other elements to increase both corrosion resistance and strength [8]. The alloying elements generally present in the two alloys investigated is presented in Table 2-1.

Large amounts of alloying elements often results in complex microstructures. A number of both beneficial and detrimental secondary phases may be present in as-delivered solution annealed and aged superalloys. Heat treatments and welding is made complicated by various solidification mechanisms and phase transformations.

*Table 2-1: Main alloying elements (wt %) in Inconel 718 and 625 PLUS [1, 2].*

<b>Element</b>	<b>Inconel 718</b>	<b>625 PLUS</b>
Ni	50.00-55.00	59.00-63.00
Cr	17.00-21.00	19.00-22.00
Fe	Balance (~19.00)	Balance (~5.00)
Nb	4.75-5.50	2.75-4.00
Mo	2.80-3.30	7.00-9.50
Ti	0.65-1.15	1.00-1.60
Al	0.20-0.80	0.35 max.
C	0.08 max.	0.03 max.

#### 2.1.1 Principal strengthening precipitates, $\gamma''$ and $\gamma'$

Nb is added as an alloying element to promote the formation of the main strengthening phase,  $\gamma''$  with the chemical composition  $\text{Ni}_3\text{Nb}$ . The precipitate is a body centered tetragonal precipitate which is coherent with the matrix. Strengthening is caused by relatively large mismatch strains between the precipitates and the matrix (~3%) [2].

The small, disc shaped precipitate is formed when Nb-bearing alloys is age hardened at around 650°C. Because of the slow precipitation kinetics of  $\gamma''$ , there is a certain delay upon aging before any significant increase in strength [7]. This “sluggish” precipitation kinetics provides these alloys with a reduced tendency for cracking during post-weld heat treatments.  $\gamma''$  is the principal strengthening precipitate in both alloys investigated.

Formation of the other strengthening precipitate common in superalloys,  $\gamma'$ , requires additions of Al and Ti. The alloys investigated only contain small amounts of both elements, as seen in Table 2-1. As a result, the volume fraction of  $\gamma'$  is expected to be low. Also note that there is no phase sequence between the two precipitates  $\gamma'$ ,  $\gamma''$  or the  $\gamma$ -austenite matrix.

### 2.1.2 $\delta$ -Phase

The main strengthening phase  $\gamma''$  is a metastable precipitate. High temperature heat exposures over long periods of time will lead to the formation of the stable, but deleterious  $\delta$ -phase. Unlike  $\gamma''$ ,  $\delta$ -phase is incoherent with the  $\gamma$ -austenite matrix and is associated with reduction in creep strength and ductility. The fastest rate of this phase transformation occurs at around 900°C, as shown in the TTT diagram in Figure 2-1. However, use of these alloys is often restricted to service temperatures under 650°C because of the precipitation of  $\delta$ -phase at long temperature exposures [9, 10].

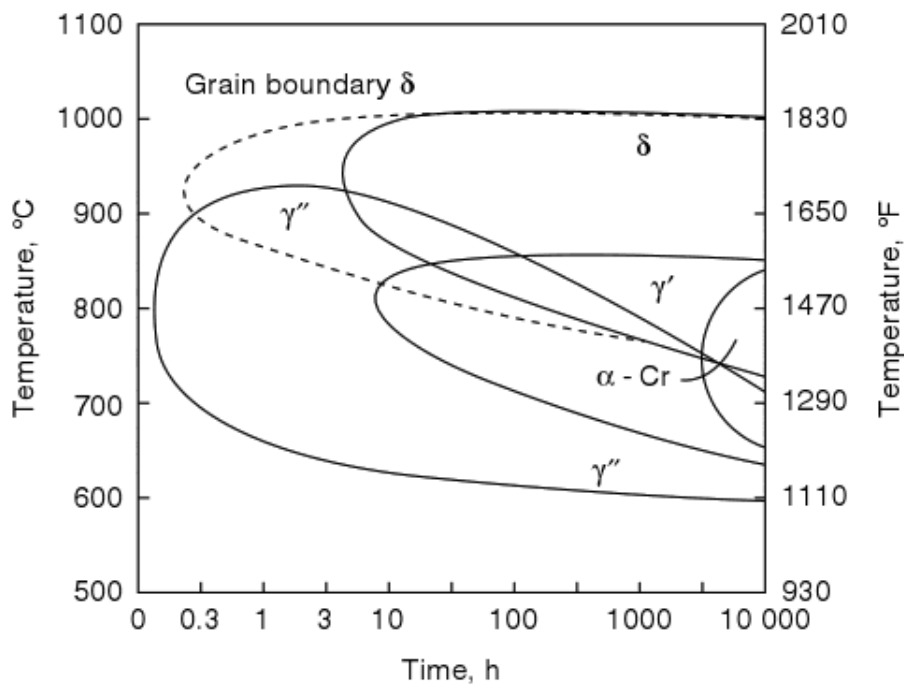
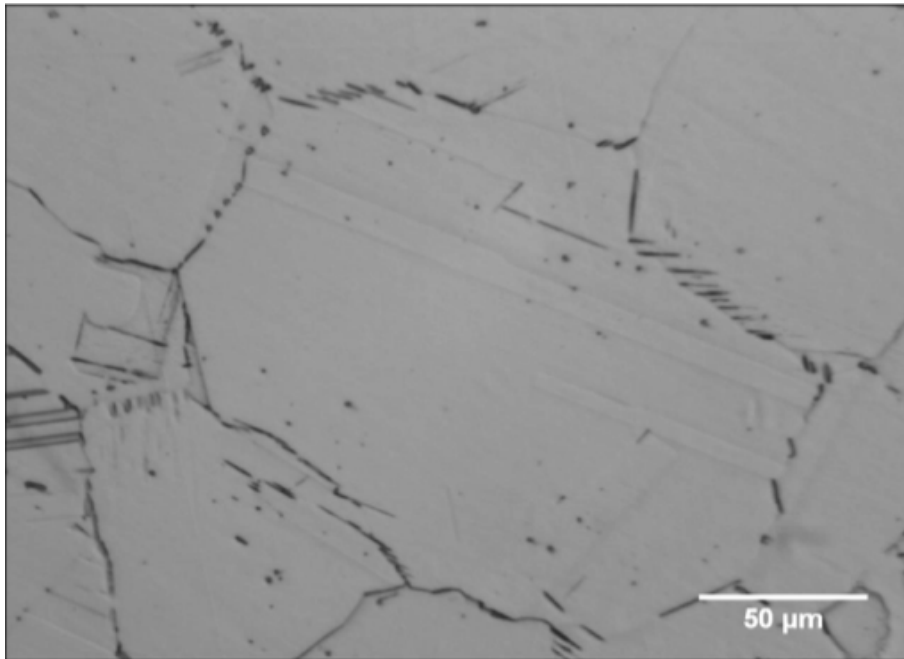


Figure 2-1: TTT diagram for Inconel 718 [2].

$\delta$ -phase has the same  $\text{Ni}_3\text{Nb}$  chemical composition as  $\gamma''$ , with an orthorhombic crystal structure. The phase can form intergranularly in “needle shaped” acicular form under the presence of  $\gamma''$ . These “needle shaped” precipitates are commonly found decorating the grain boundaries, extending into the grain in severe cases [9].

Standard 6A718 [11] from the American Petroleum Institute (API) is used to ensure that Inconel 718 used for pressure-containing or pressure controlling components in the petroleum industry is not embrittled by the presence excessive amounts of deleterious phases like  $\delta$ -phase. Low amounts of particles formed at isolated grain boundaries are accepted according to the standard. However, continuous networks of secondary phases along grain boundaries are deemed unacceptable.

Figure 2-2 shows an image of the characteristic needle shaped  $\delta$ -phase associated with an unacceptable microstructure, according to API’s standard.



*Figure 2-2: Needle shaped acicular  $\delta$ -phase decorating the grain boundaries, extending into the grains of Inconel 718 [11].*

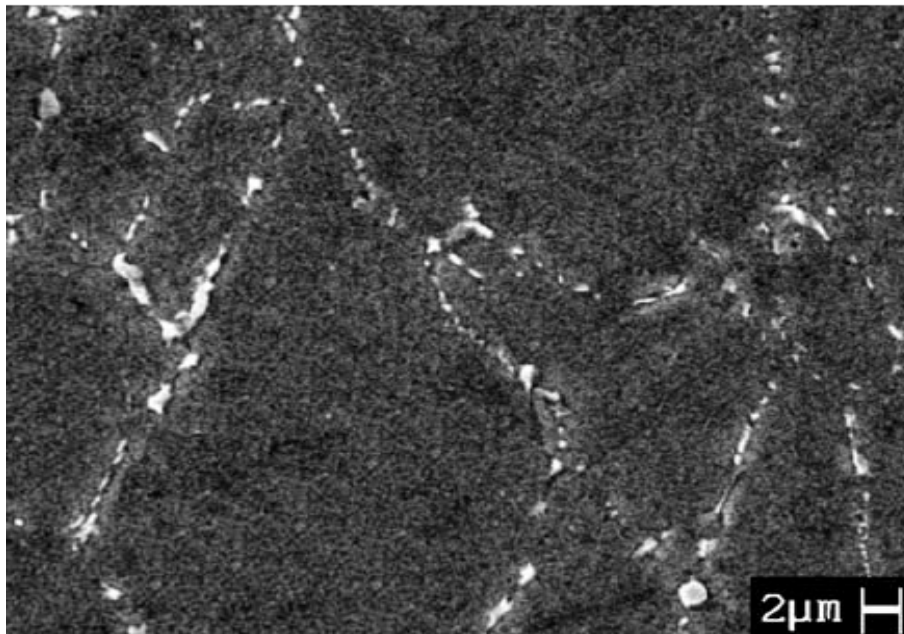


*Figure 2-3: Fine globular  $\delta$ -phase decorating the grain boundaries of Inconel 718 [12].*

The phase can also exist as strings of circular or slightly elongated, relatively coarse particles termed globular  $\delta$ -phase as shown in the scanning electron microscope (SEM) image in Figure 2-3. These particles originate from the fragmentation of the larger needle-shaped  $\delta$ -phase [9].  $\delta$ -phase is known to form and accumulate after repair welding of weldments that



have received some form of post-weld heat treatments in order to restore the  $\gamma''$  precipitate in the weld metal [2].

Heat exposure from welding could form  $\delta$ -phase in the base material and HAZ of as-welded alloys. However,  $\delta$ -phase transformation in these regions is not expected due to the short time of heat exposure from welding, in particular electron beam welding.

### 2.1.3 Laves Phase

Laves phase is an intermetallic topologically close-packed phase. It is commonly present in precipitation strengthened Ni-base alloys due to strong the segregation behavior of the alloying element Nb during solidification. The crystal structure of Laves phase is hexagonal with  $A_2B$  stoichiometry where “A” may represent elements Fe, Ni, Cr and “B” may represent “Nb, Mo, Si” [2, 8].

Both Si and Fe are known to promote the formation of Laves during solidification [2]. The formation of Laves is common in the interdendritic regions during weld metal solidification. The embrittling phase is detrimental to weld mechanical properties such as ductility and tensile strength as the plate-like morphology aids in crack initiation and propagation. In addition, formation of Laves consumes valuable alloying elements, such as Nb. Solution annealing is commonly used to dissolve the Laves phase in as-solidified superalloys.

**Feil! Fant ikke referansebildet.** shows the eutectic formation of a  $\gamma$ /Laves section in the gray  $\gamma$ -austenite matrix during solidification. The image is from specimen heavily alloyed with Fe to increase the segregation behavior of Nb and the formation of the bright appearing, continuous Laves sheets.



*Figure 2-4: Laves phase in a eutectic formation with  $\gamma$ -austenite after solidification [13].*

### 2.1.4 Carbides

Carbides commonly found in superalloys are MC, M<sub>6</sub>C and M<sub>23</sub>C<sub>6</sub>, where M is the partitioning metal element. These precipitates are dense, closely packed compounds with an FCC crystal structure. Metal elements partitioning in the different carbides is listed in Table 2-2.

Table 2-2: Elements partitioning in carbides [2].

Carbide	Metal Element
MC	Ti, Nb, Mo, W
M <sub>6</sub> C	Mo, W
M <sub>23</sub> C <sub>6</sub>	Cr, Mo, W

The only carbide containing the element Nb is the MC carbide. Hence, the carbides containing the element is often referred to as NbC. Carbides rich in these two elements precipitate above 982°C, and minimize the precipitation of undesirable intergranular M<sub>6</sub>C and M<sub>23</sub>C<sub>6</sub> during subsequent aging treatments [1]. They are also known to have a beneficial effect on tensile strength at high temperature service environments by restricting grain boundary sliding [2, 7, 14].

The MC carbides may form at grain boundaries or in the interdendritic regions at the end of solidification of the metal in a eutectic-type reaction. MC carbides may be observed as discrete particles, or as strings of a few particles. These carbides vary in size between 0.01-10 μm and appear as rounded precipitates with a dark or slightly shining appearance, as seen in Figure 2-5. MC carbides may decompose into both M<sub>6</sub>C and M<sub>23</sub>C<sub>6</sub> at the grain boundaries during thermal processing or under high temperature service.

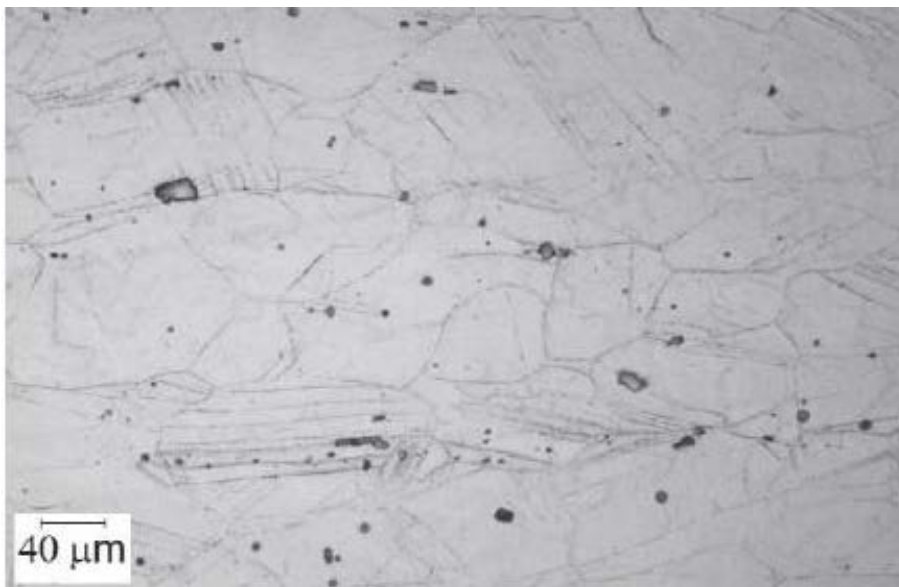


Figure 2-5: Carbides at the grain boundaries in a superalloy [2].

## 2.2 Weld Metallurgy

The weld metallurgy of superalloys is often complex as a result of the segregation behavior of the alloying elements, in particular Nb. The segregation leads to eutectic type constituents and secondary phases in the solidified weld metal. The constituents are usually not present in the base metal to the same degree, as a result of solution annealing of as-delivered material. Other issues related to welding of these alloys include solidification cracking in the weld metal and liquation cracking in the heat affected zone (HAZ) [2].

The weldability of 625 PLUS is generally considered to be superior to Inconel 718. The combination of low C, Si and Nb content in 625 PLUS results in comparatively lower volume fractions of detrimental secondary phases in the weld metal upon solidification [6].

### 2.2.1 Solidification of Weld Metal

The solidification in Nb-bearing superalloys is usually a three-step process. Solidification initiates with the formation of the  $\gamma$ -austenite matrix in a dendritic structure following the reaction  $L \rightarrow \gamma$ .

As alloying elements such as Nb and C is rejected from dendritic regions during solidification, the remaining liquid becomes progressively enriched with these elements until it reaches the line between  $\gamma$  and NbC, as seen in Figure 2-6. Solidification of the interdendritic regions ensues with the eutectic-like reaction  $L \rightarrow \gamma + \text{NbC}$ , when the solid solubility of the liquid is reached. The liquid composition continues to be depleted of C as  $\gamma/\text{NbC}$  solidifies, until the chemical composition of the liquid area consists of approximately 19.1 wt% Nb and 0.03 wt% C. At this point the remaining liquid in the interdendritic region solidifies into eutectic  $\gamma$  and stoichiometric Laves phase in the reaction  $L \rightarrow \gamma + \text{Laves}$ . Higher volume fractions of Laves phase in the  $\gamma/\text{Laves}$  eutectic constituents is associated with an increase of segregation of Nb to the interdendritic areas [2, 13].

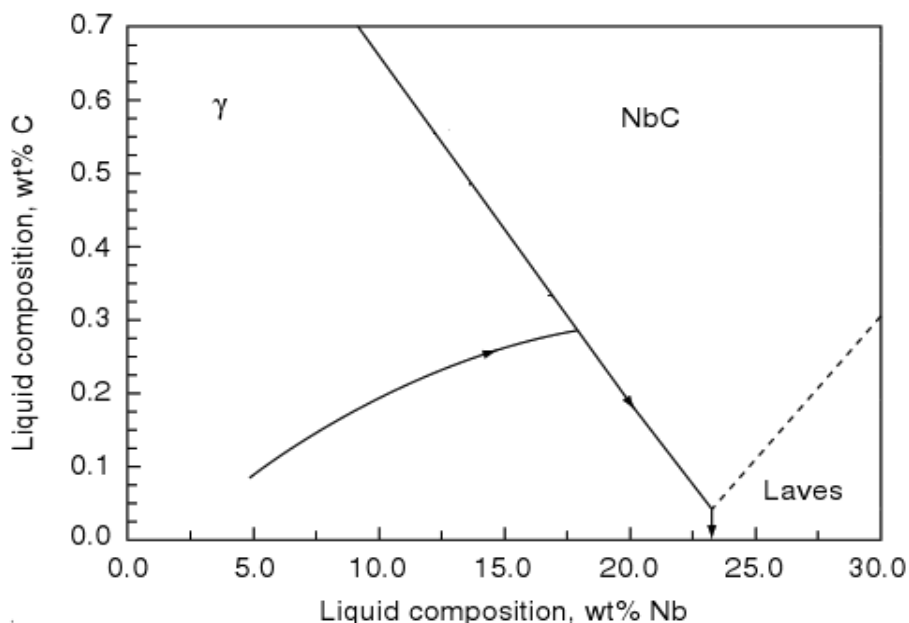
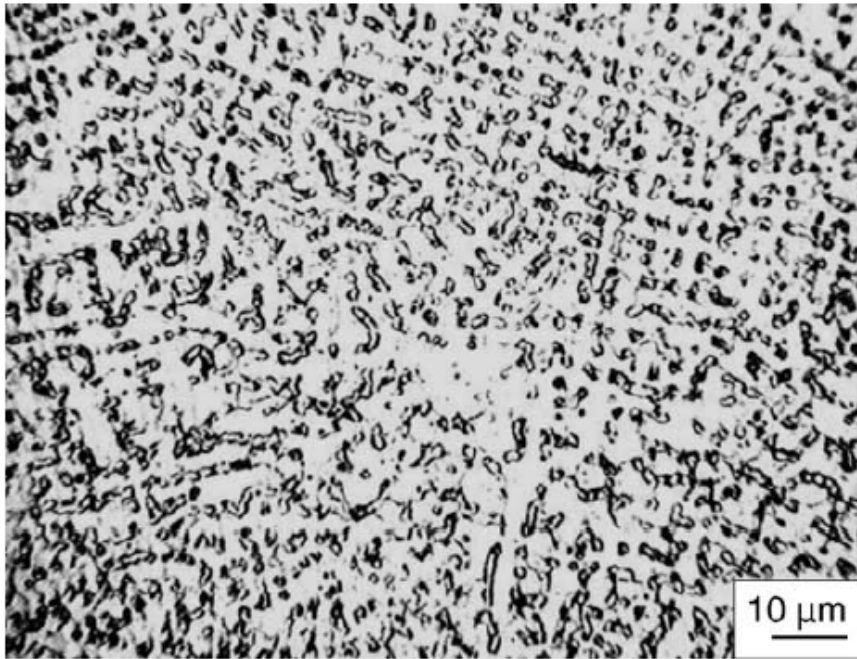


Figure 2-6: Solidification diagram of superalloys [2].

Previous investigations on the microstructural evolution of fusion welds [2, 6] found that  $\gamma$ /Laves was the major interdendritic constituent in both Inconel 718 and 625 PLUS, because of the alloys low C levels. NbC was only found in small quantities. This is associated with the low carbon levels of both alloys. **Feil! Fant ikke referansebildet.** shows an image of the typical interdendritic structure of the dark appearing  $\gamma$ /Laves constituents in the smooth appearing  $\gamma$  dendrites.



*Figure 2-7: Interdendritic structure containing eutectic  $\gamma$ /Laves in the weld metal of Inconel 718 [12].*

Addition of Fe is well-known to promote the formation of Laves phase in Ni-base Nb-bearing alloys. The alloying element increases the segregation potential of Nb to the remaining liquid upon solidification [2]. As the segregation of Nb increases in the presence of Fe, larger volume fractions of interdendritic  $\gamma$ /Laves constituents are expected in the weld metal of alloys containing significant amounts of Fe, such as Inconel 718. The alloy contains considerably more of the alloying element (~19 wt % Fe) than 625 PLUS (~5.00 wt % Fe). Cieslak *et al.* [6] found relatively small amounts of eutectic constituents in the weld metal of 625 PLUS compared to similar weld specimens of Inconel 718. An increase in the element Nb itself would yield a higher volume fraction of interdendritic constituents, as the secondary phases, NbC and Laves, is highly enriched in the element [2].

Segregation occurs for several elements during solidification. The elements Nb and Mo are known to segregate to the interdendritic constituents during dendritic solidification. Higher percentages of these elements are expected in the eutectic  $\gamma$ , and a noticeable depletion may be observed in the  $\gamma$  dendrites as a result. [6].

### 2.2.2 Solidification Cracking

Solidification cracking may occur in the weld metal upon solidification. The cracking susceptibility of Nb-bearing alloys is considerably higher when compared to most engineering alloys. This is attributed to by the formation of eutectic type constituents like  $\gamma$ /Laves and  $\gamma$ /NbC during solidification, which expands the temperature range of solidification and promotes cracking. Cracking of the weld metal may form during the stages of solidification when liquid films are distributed along the grain boundaries or at the interfaces of the interdendritic regions. Shrinkage across the partially solidified boundaries induces strains that lead to the formations of cracks [2].

A previous investigation [6] found that Inconel 718 was more susceptible to solidification cracking than 625 PLUS. Figure 2-8 shows the appearance of a solidification crack in an optical light microscopy.

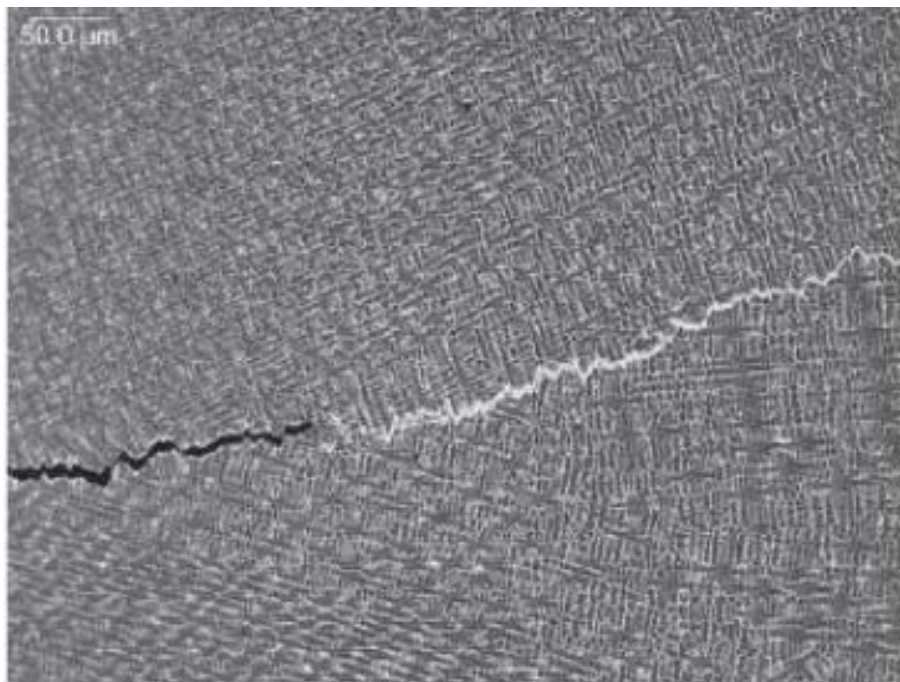


*Figure 2-8: Solidification crack in the weld metal of a superalloy [2].*

### 2.2.3 HAZ Liquefaction Cracking

A general problem with Inconel 718 is the solidification of liquid films along grain boundaries in the HAZ, resulting in detrimental Laves sheets at the grain boundaries [2, 3]. Heat exposure from welding procedures causes the formation of the liquid films along the grain boundaries in the area of HAZ closest to the weld metal, which solidifies in a eutectic reaction. The formation of these microfissures is known as HAZ liquation cracking. An example of the microstructure associated with the liquation cracking is found in Figure 2-9.



Figure 2-9: Liquation cracks in the grain boundaries in the HAZ of gas-tungsten-arc welded Inconel 718 [4].

R.G Thompson and S. Genculu [15] postulated that HAZ liquation cracking in Inconel 718 is associated with the liquation of NbC on the grain boundaries during welding. The postulated mechanism is illustrated in Figure 2-10. The intergranular liquid films solidified in eutectic Laves constituents in the HAZ adjacent to the weld metal.

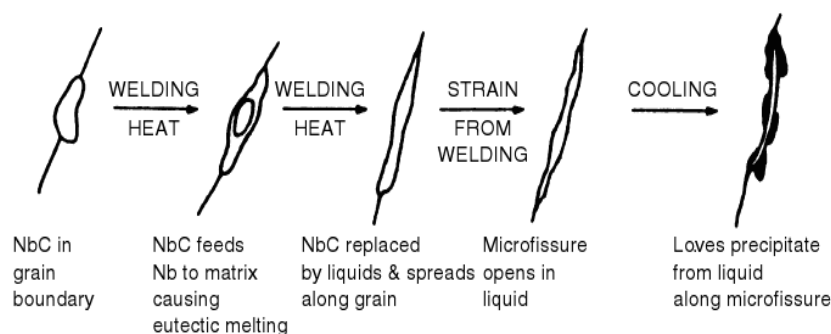


Figure 2-10: HAZ liquation cracking mechanism in Inconel 718 [2].

The HAZ liquation cracking susceptibility is known to be considerable in Inconel 718 [3, 4, 15]. Electron beam welding is known to be a more demanding welding technique in avoiding HAZ liquation cracking in comparison with more traditional welding techniques. The liquation cracks tend to form in near the top of the weld bead, in the “nail head” area. Welding parameters should be adjusted to avoid the “nail head” shape of the weld bead [4].

#### **2.2.4 Post-Weld Heat Treatments**

Most precipitation strengthened superalloys require full solution anneal and aging treatments following welding in order to restore the alloys mechanical properties. Direct aging is not sufficient as this increases the risk of overaging of the base metal. In addition, the microstructure in the HAZ and weld metal may still contain the detrimental phases associated with welding [2]. Solution annealing is used to dissolve the detrimental interdendritic constituents and make the chemical composition more uniform. The treatment increases the diffusion of Nb, which becomes more equally distributed throughout the metal and available for precipitation strengthening [16]. Hence, subsequent age hardening leads to more uniform distribution of the  $\gamma''$  precipitate.

Solution annealing is conducted at various temperatures depending on the circumstances. However, temperatures are always kept under the solid solubility of the alloy in order to avoid liquation [2]. Temperature ranges between 980°C-1080°C are frequently used for Inconel 718. Aging treatments subsequent to solution annealing is used to promote the precipitation of the principal strengthening precipitate  $\gamma''$ . Inconel 718 has been found to have the superior aging response compared to 625 PLUS, as a result of its high additions of Nb [1].

### **2.3 Electron Beam Welding**

Electron Beam Welding (EBW) utilizes a high energy electron beam to melt and fuse metal workpieces together. The high heat density of EBW results in a lower net heat input when compared to other welding processes. The rapid cooling from the low heat input results in less Nb segregation and lower concentration of the element in the interdendritic areas. This has been shown to be more beneficial for control of the formation of Laves phase in the weld metal [17]. Less dissipation of the metal and a lower risk of solidification cracking are associated with the low heat input of this welding technique [12, 18].

Some of the main characteristics of EBW include:

- High welding speed which results in narrow welds and a small HAZ, with little distortion of the workpiece [19].
- No shielding gas, filler metal or applied pressure is required [19, 20].
- Consistent welds of high quality, as the welding procedure is an automated process performed in a vacuum.

EBW is known for its excellent penetration ability. The kinetic energy of accelerated electrons in the beam is converted into thermal energy upon collision with the workpiece. As temperatures directly under the beam can reach 14 000°C, the metal is vaporized instantaneously. The electron beam penetrates metal vapor with more ease than solid metal, leading to further penetration into the workpiece. The result is narrow, deep welds where the depth-to-width ratio can exceed 20:1 [20, 21].



### 2.3.1 Electron Beam Welding Components

The electron gun is the component creating the electron beam. It consists of a high voltage power supply, connected to an anode and a cathode. The cathode is usually a tungsten filament. Heat is generated in the filament by passing low current through it. The heat causes electrons in the filament to be emitted through thermionic emission [20].

Electrons are accelerated from the cathode to the anode by a difference in electric potential, known as the *accelerating voltage*. Electrons are focused through a hole in the anode. Both magnetic and electrostatic lenses are used for further focus of the beam towards the workpiece [22]. A schematic drawing of an electron gun is shown in Figure 2-11.

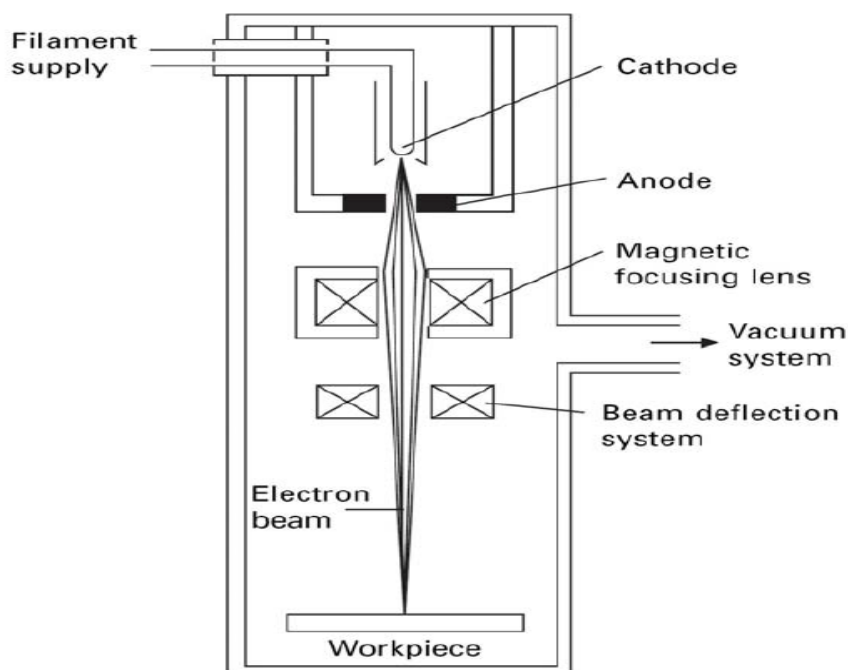


Figure 2-11: Schematic view of the electron gun [22].

The workpiece is welded inside a vacuum chamber to reduce collisions between molecules in the air and the electron beam. Collisions would cause scattering and dissipation of the beam [20]. A positive side effect is that this creates a clean and inert environment for the weld. However, the chamber has space limitations and creating a vacuum may consume a considerable amount of time depending on the chamber size. In addition, cleanliness is essential as different oil compounds may vaporize in the vacuum conditions produced [22].

### 2.3.2 Mechanism of Welding

Because of the high temperature and vaporization of metal, a welding technique known as *keyhole welding* is used in EBW. As the high energy electron beam moves over the surface, a cavity of vaporized metal is formed directly under the heat source. This cavity of metal vapor is known as the *keyhole*. It is vital to maintain the keyhole during the welding process to ensure the quality of the weld [22].

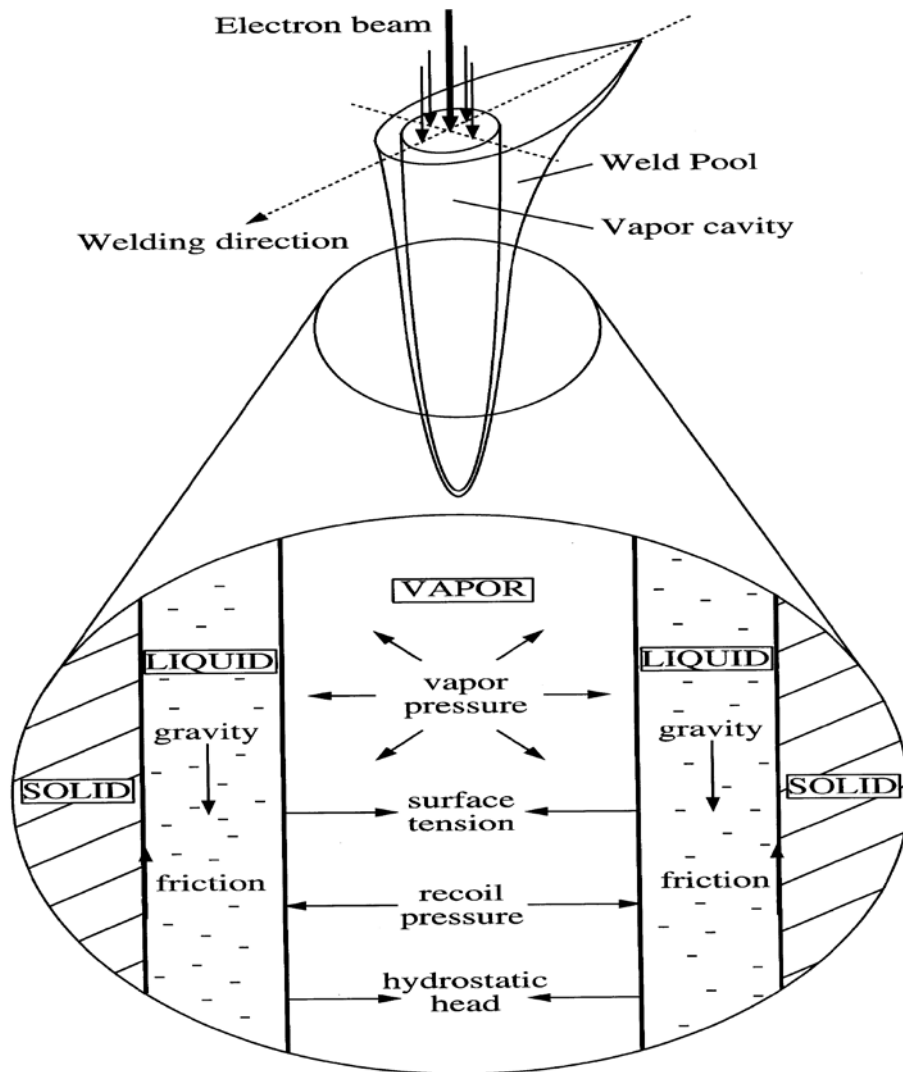


Figure 2-12: Forces maintaining the shape of the keyhole [18].

Vapor pressure and recoil pressure from the evaporating metal provides forces which expands the keyhole. These forces are countered by the keyhole-closing forces from surface tension and hydrostatic head in the molten metal surrounding the keyhole. Friction between the molten material and solid metal prevents the liquefied area from sinking under the force of gravity [18]. A schematic view of the forces maintaining the keyhole shape is found in Figure 2-12. A balance of these forces is essential in maintaining a keyhole and insuring good quality of the weld.

As the electron beam moves over the workpiece surface, molten metal from the front of the beam moves around the keyhole to the back of the beam. This is known as thermocapillary (Marangoni) flow [18, 23].

A reservoir of molten metal fills the weld from behind, where it solidifies and forms the weld bead. Figure 2-13 illustrates the thermocapillary flow seen from the cross section of the weld bead.

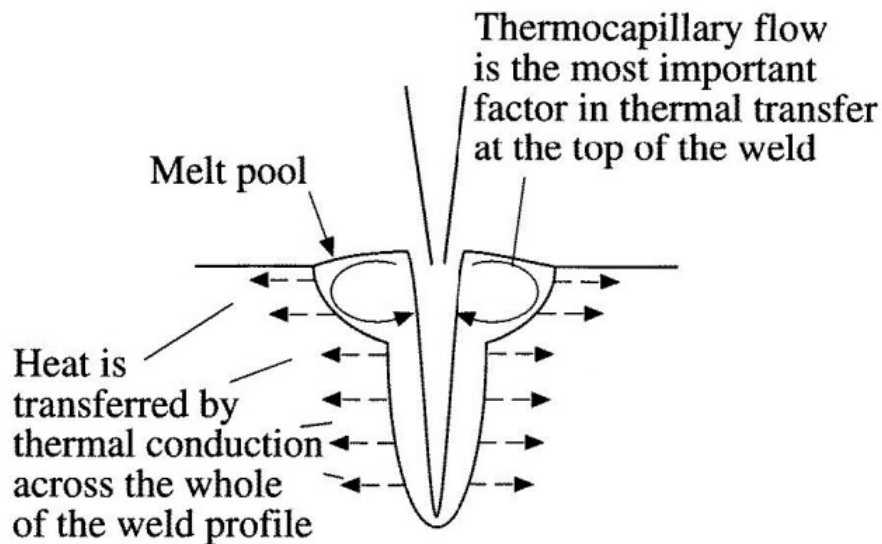


Figure 2-13: Thermocapillary flow around keyhole [23].

### 2.3.3 Welding Parameters

Automating the EBW process is a necessity because keyhole welding requires stable operating conditions and consistent welding parameters.

The different welding parameters usually affect penetration depth. For instance, an increase in power, either from voltage or current, will increase penetration depth [21]. However, excessive power can force an expanding collapse of the keyhole [18]. A balance of welding parameters is required, and companies spend time developing specific welding procedures for each relevant alloy.

#### ***Accelerating Voltage***

Accelerating voltage is the difference in potential between the anode and the cathode. This difference accelerates the electrons, providing them with kinetic energy. It is more convenient and flexible to operate with a set voltage while using the beam current as an adjustable parameter [18, 21].

#### ***Beam Current***

For a given voltage, an increase in beam current will result in an increase in penetration depth. However, overuse of beam current will melt more metal than the recoil and vapor pressure can hold, resulting in a collapse of the keyhole and sinkage of the weld [18, 21].

### ***Lens Current (Focus)***

Focus is achieved by the use of current through electromagnetic lenses in the electron gun. Focus can be adjusted for different effect. Placing the focus point inside the workpiece creates a sharp and narrow weld. Focusing over or under the workpiece will increase the spot diameter and reduce the power density [21]. Intentional de-focusing, that is placing the focus point either above or below the workpiece surface, is the easiest way to control the keyhole maintaining forces. The amount of de-focus is often expressed in terms of mA, and is determined by trial welds on the relevant alloy [19].

### ***Welding Speed***

Welding speed is the velocity of the beam as it moves over the surface of the material. It is common to keep the electron gun stationary, while moving the workpiece. Penetration is reduced as welding speed is increased [20].

## **2.4 Fracture Mechanics**

For engineering purposes, two modes of fracture are possible; ductile and brittle. Ductile fracture is preferred because plastic deformation of a structure may serve as a warning before fracture, allowing for corrections to be made. Distinguishing between the two modes can be problematic in cases with low amounts of plastic deformation. Some characteristics of the two modes discussed in this section.

Common for both fracture modes are the two steps before fracture; *crack formation* and *crack propagation*, in response to an imposed stress [24].

Inconel 718 and 625 PLUS have similar tensile strength as-delivered. However, the weldability and amount of interdendritic constituents present after solidification of the weld metal in each alloy will be the determinate factor for the comparison of tensile strength in the as-welded condition.

### 2.4.1 Ductile Fracture

Ductile fracture is defined as a fracture involving noticeable plastic deformation in the fractured area. The mechanism of ductile fracture can be described in four steps [25, 26]:

1. *Void nucleation* at inclusions or second phase particles.
2. *Void growth* by means of plastic strain and hydrostatic stress.
3. *Crack propagation* by the coalescence of voids.
4. Separation at the *shear lips*.

Voids form around inclusions or second phase particles when sufficient stress is applied to break the interfacial bonds between the particles and the matrix [25]. Void nucleation develops either by a) decohesion at the interface between the particle and matrix, b) fracture of the particle or c) decohesion of an interface as a result of shear deformation or grain boundary sliding [26], as seen in Figure 2-14. Larger particles are more likely to crack when plastic strain is applied, because they are more likely to contain small defects [25].

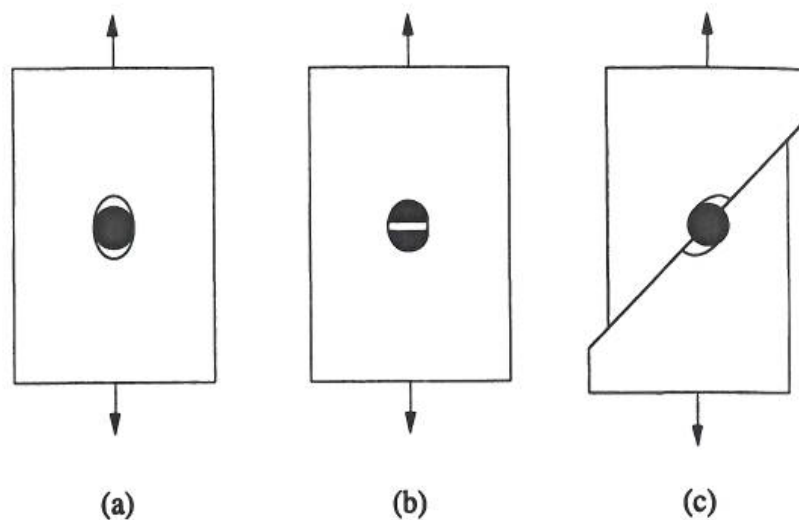


*Figure 2-14: Void nucleation by a) decohesion in the particle-matrix interface, b) cracking of particle, c) decohesion of an interface associated with shear deformation or grain boundary sliding [26].*

A descriptive expression of ductile fracture is “hole-joining fracture”. Plastic strain and hydrostatic stress cause the formed voids to grow. The applied tensile stress causes deformation of the intervoid material. The voids coalesce with adjacent voids to form a crack [26]. This mechanism is illustrated in Figure 2-15.

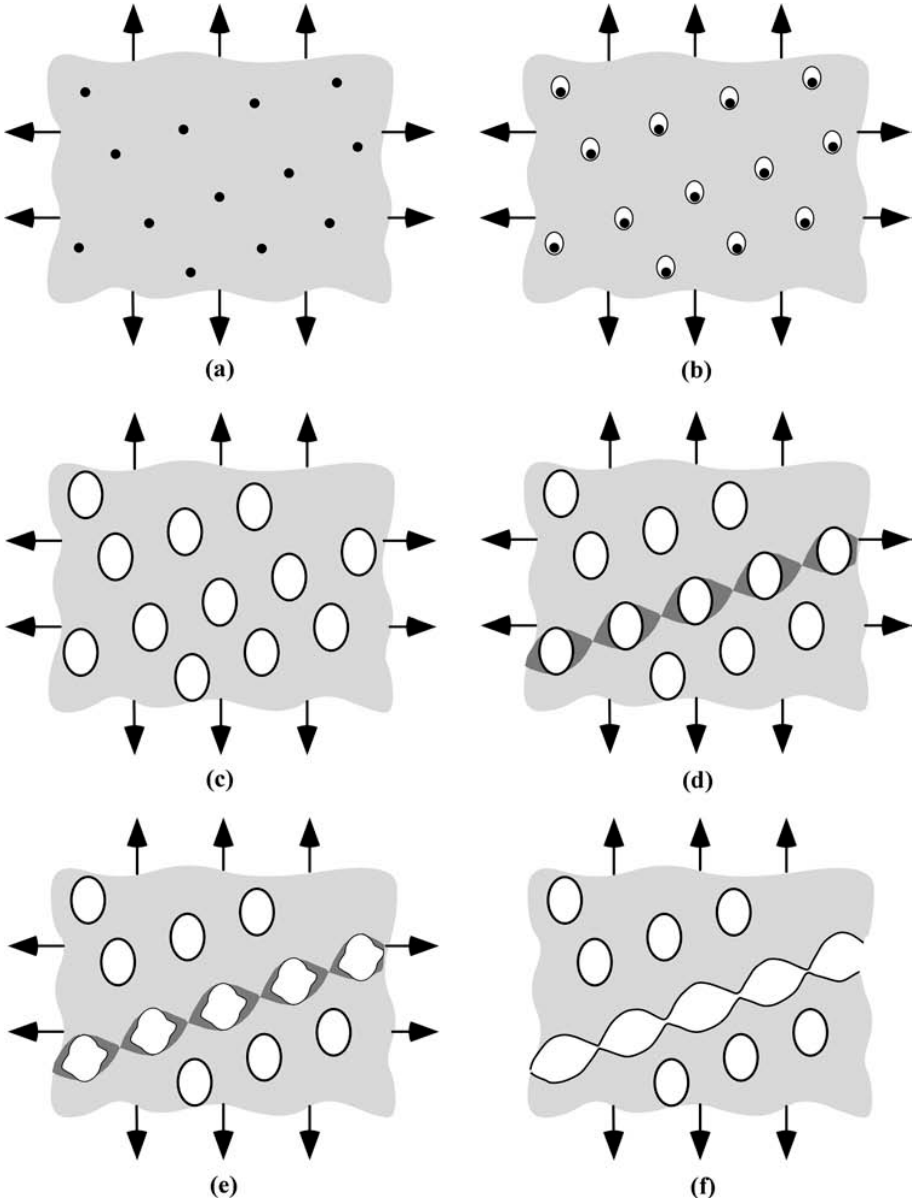


*Figure 2-15: Mechanism of ductile fracture via a) inclusions, b) void nucleation, c) void growth, d) strain on the material between voids, e) necking in the intervoid material and f) coalescence of voids leading to fracture [25].*

### ***Cup-and-Cone Formation***

Formation of a fracture surface known as *cup-and-cone* is a common characteristic of ductile fracture in cylindrical tensile specimens [24]. Axi-symmetrical necking occurs after some uniform deformation. The hydrostatic stress field in the cross-section of the neck is highest at the center of the specimen. The outer ring of specimen contains relatively few voids since the hydrostatic stress is lower than in the center [25, 26]. Hence, the mechanism of void nucleation, growth and coalesce will mainly occur in the center of the specimen. This mechanism is dominated by plane strain, which causes the crack to form  $90^\circ$  to the tensile axis. The initial fracture propagates from the center and forms a fracture surface perpendicular to the tensile axis. The initial fracture propagates from the center and forms a fracture surface perpendicular to the tensile axis.

The final fracture ensues by rapid propagation of the crack around the un-fractured outer area of the fracture surface. It is dominated by plane stress which is at its highest  $45^\circ$  to the applied pressure, and so the fracture surface is  $45^\circ$  to the tensile axis. This sloped material at the outer edge is known as the *shear lip* [24]. The mechanism is illustrated in Figure 2-16.

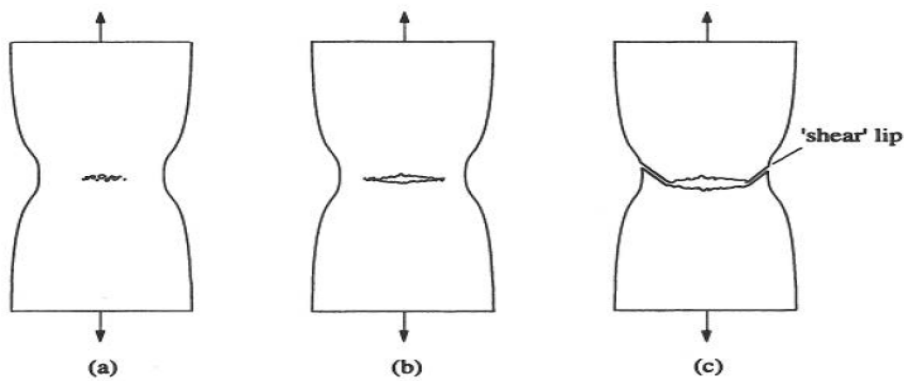


*Figure 2-16: Mechanism leading to cup-and-cone fracture in a tensile specimen in steps of a) void nucleation, b) void coalescence and c) fracture by separation of the “shear lips” [26].*

Formations known as dimples can be observed upon high magnification fractographic examination in SEM microscopes. The dimples are half of a void that formed before final fracture. The preferential fracture paths of dimples are usually in the direction parallel to the tensile axis in the initial crack area. An image of dimples showing a preferential fracture path is found in Figure 2-17.

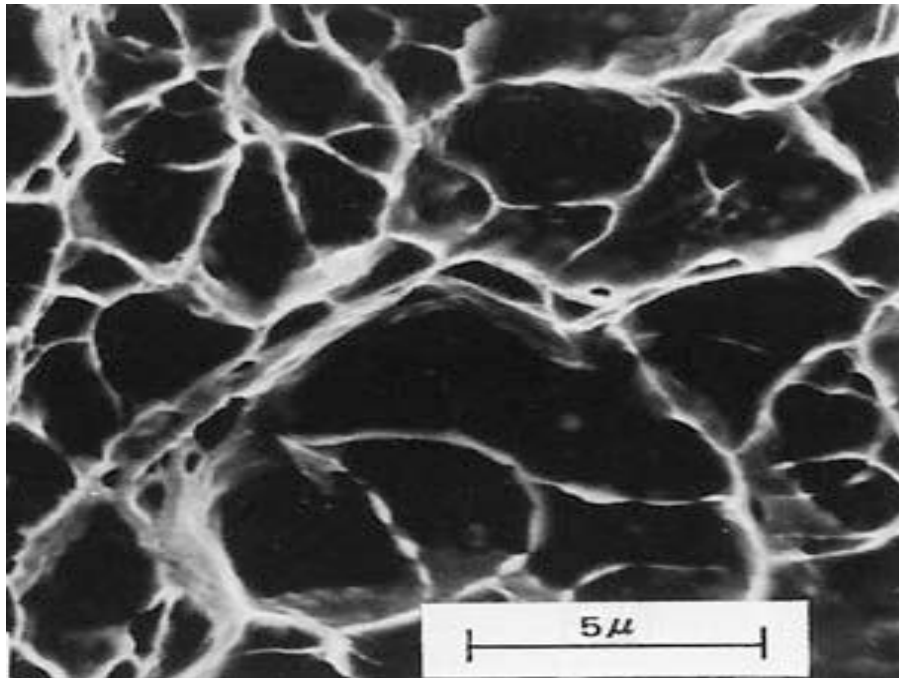


*Figure 2-17: Fractograph showing spherical dimples characteristic of ductile fracture [24].*



Previous fractographic examinations of Inconel 718 [12, 17] resulted in ductile fractures with relatively small amounts of plastic deformation. Fractographs revealed a fracture surface with a distinct dendritic structure as a result of the solidification behavior of the alloy. The shallow dimples showed no preferential fracture path, as seen in Figure 2-18.

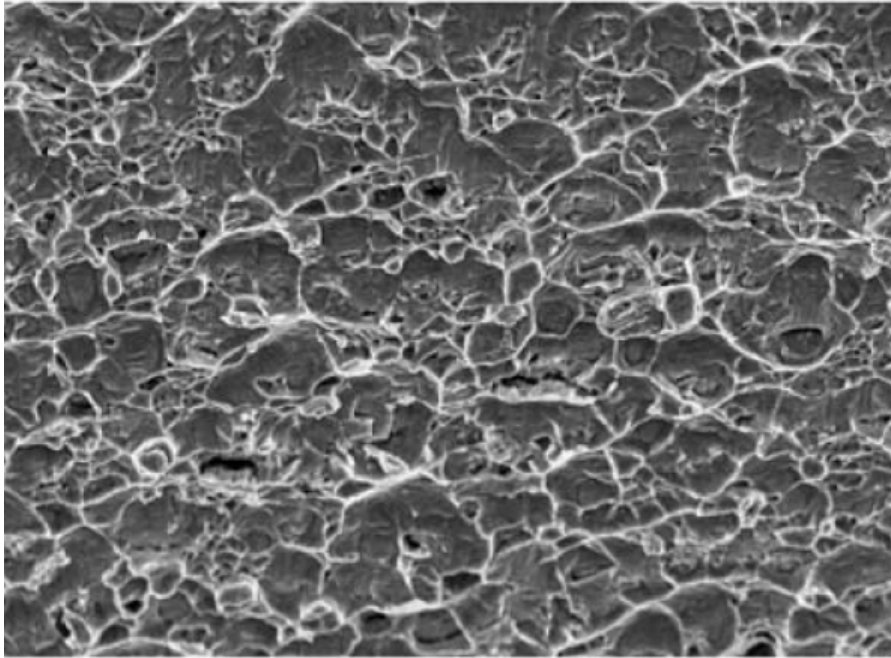


*Figure 2-18: Fractograph of weld metal in Inconel 718 showing a dendritic fracture pattern [17].*

### 2.4.2 Brittle Fracture

Brittle fracture develops by rapid crack propagation without any appreciable plastic deformation. The entire fracture surface is perpendicular to the tensile axis [24].

The most common form of brittle fracture is cleavage, or transgranular cracking. It is characterized by successive and repeated breaking of atomic bonds along specific crystallographic planes. The planes with the lowest packing densities are preferred. The crack may change direction over a grain boundary to find the plane with the least resistance [24, 25].

Macroscopically the cleavage surface appears grainy or faceted. Fractographic examinations also reveal the faceted nature of the surface, where each facet corresponds to a single grain. Lines known as “river patterns” can be seen as thin bright lines on each facet. These lines are caused as the crack encounters a grain boundary, and the nearest cleavage plane is located at a slight twist angle from the current cleavage plane [24, 25]. The faceted nature and formed “river patterns” associated with cleavage fracture can be seen in Figure 2-19.

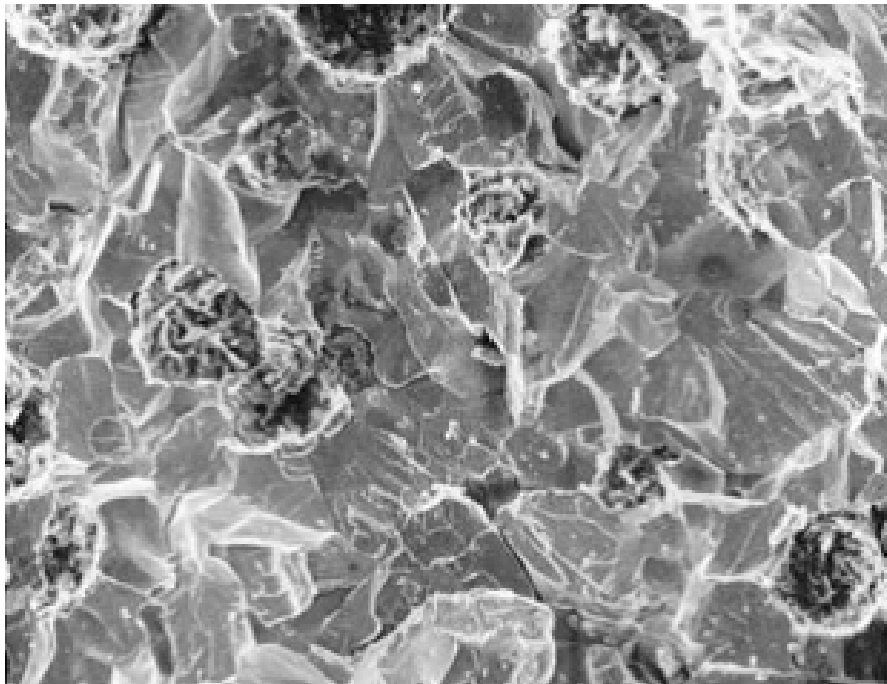


*Figure 2-19: Fractographic image of a cleavage fracture [24].*

Cleavage is common in materials where plastic flow is restricted. Metals with FCC structure, like the  $\gamma$ -austenite matrix in Ni-base alloys, are usually not affected by cleavage as the numerous slip planes of the FCC unit cell always allows for ductile behavior before fracture [25].

## 2.5 Corrosion

Corrosion is an electrochemical oxidation process where metal transfers electrons to the environment and changes valence, shifting into positive ions [27]. The electrons are consumed by reactions on the interface between the metal and the environment.

A full electrochemical cell needs to be established for corrosion to occur. A complete cell is dependent on three elements: 1) an anode to provide electrons 2) a cathode to consume electrons and 3) an electrically conductive electrolyte often referred to as the environment. The illustrative drawing of a hypothetical cell is shown in Figure 2-20. Cathodic and anodic areas are established in various places on the metal surface, depending on the corrosion form.

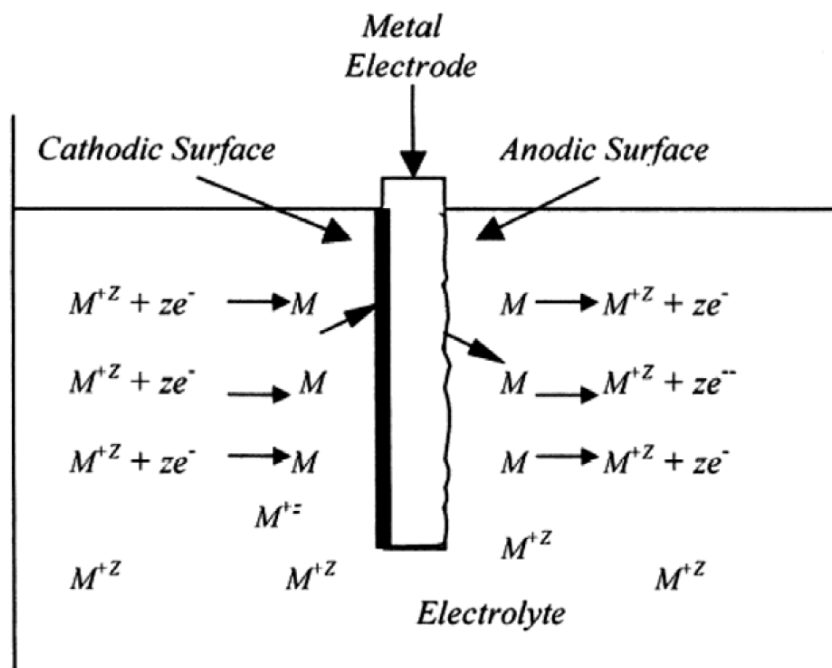
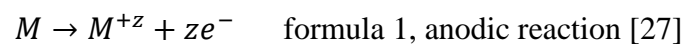


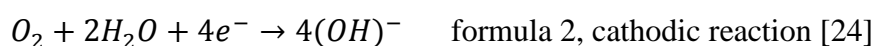
Figure 2-20: Illustrating a full electrochemical cell [27].

Electrons are transmitted from the anode through an anodic reaction. The typical anodic reaction formula is stated in formula 1,



where  $M$  is the corroding metal. The positive metal ions,  $M^{n+}$ , dissolve into the environment and the material is dissolved.

There is no net accumulation of the electrons transmitted from the anodic reaction [24]. A continuously consumption of electrons through cathodic reactions is necessary for corrosion to be sustained. Different cathodic reactions are involved depending on the environment. An example of a typical cathodic reaction for a neutral or basic aqueous solution is stated in formula 2.



Nickel-base superalloys are passivated alloys. A thin oxide film forms on the surface of the metal, protecting from further corrosion. Passivated alloys are prone to localized corrosion, like pitting or crevice corrosion. Different alloying elements, like chromium and molybdenum, increase the resistance to localized corrosion.

625 PLUS contains more alloying elements resisting localized corrosion than Inconel 718. 625 PLUS has been shown to have superior corrosion resistance in several sour service corrosion tests[1], and performed than Inconel 718 against both crevice and pitting corrosion.

### 2.5.1 Crevice Corrosion

Crevice corrosion is a localized form of corrosion occurring in gaps of the material containing a stagnant solution environment. The size of the gap plays a significant role. The gap has to be narrow enough for the solution to become stagnant, yet wide enough for the solution to enter [24, 28]. A practical example of a typical crevice corrosion site is the gap between washers and bolts. The mechanism of crevice corrosion is illustrated in Figure 2-21.

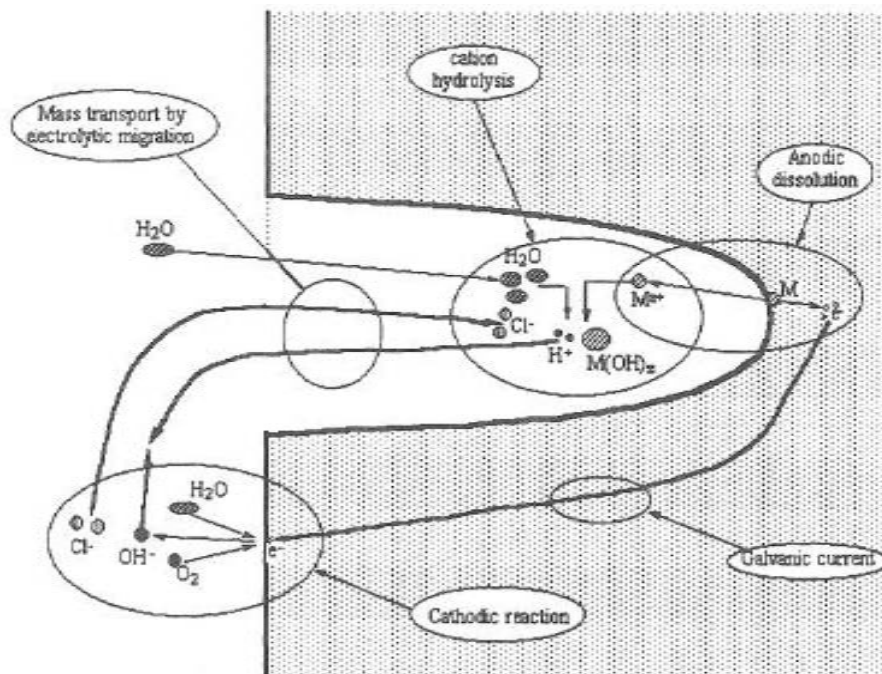


Figure 2-21: Crevice corrosion[28].

Crevice corrosion is dependent on four factors [28]:

- 1) Limited mass transport from the crevice, resulting in a *stagnant solution*.
- 2) Electrical conductivity from the metal exposed to the crevice and metal exposed to the external bulk area.
- 3) A small volume fraction of stagnant solution in contact with a, in comparison, larger crevice surface area.
- 4) Significant solution resistance between the stagnant solution and outside environment, also known as an *iR drop*.

Formation of crevice corrosion usually occurs in two steps. The first step is known as the *initiation* or *incubation period*. Little dissolution of metal occurs at this step, however the solution inside the crevice undergoes critical changes [28].

Corrosion inside the crevice takes place at the same rate as the external parts, with anodic and cathodic reactions taking place on the entire metal surface. Oxygen is depleted in the crevice as it is consumed at a higher rate than it can diffuse in. As the cathodic reaction requires oxygen, it now occurs exclusively on the external surface. A full electrochemical cell is now established. The anodic reaction occurs within the crevice, locally dissolving the metal. The large external surface provides cathodic reactions. As the external surface area is large in comparison with the crevice, large cathodic areas are in disposal to the current of electrons from the anode reaction in the crevice. The result is fast crevice propagation.

Because of the dissolution of positive metallic ions,  $\text{Cl}^-$  diffuses into the crevice to keep an electrochemical equilibrium. Metal hydroxide and hydrochloric acid forms in the crevice, gradually lowering the pH value. Breakdown of the passive layer inside the crevice occurs as a result of the increase in acidity. The surfaces inside the crevice become active after a critical point in the pH drop [28, 29].

Corrosion damage occurs during step two, the *propagation period*. Further diffusion of  $\text{Cl}^-$  into the crevice as a result of the increase in corrosion, further accelerates the corrosion. It is said that the corrosion is self-driven, and dissolution occurs at a much faster rate than during the *initiation period* [28, 29].

Design considerations should be the primary step to against crevice corrosion. Gaps and areas where the solution may become stagnant should be avoided. Welds are particularly vulnerable to crevice corrosion. Special considerations should be taken with respect to energy input to avoid cracking and fissures. Butt welds should be used instead of lap joints [29]. Material selection is another important consideration in order to avoid crevice corrosion. Metals resistant to other forms of localized corrosion, like pitting, will also have a high resistance to crevice corrosion.

### **2.5.2 Pitting Corrosion**

Pitting is a local corrosion attack on a surface due to highly localized anodic reactions [24, 27]. Pitting occurs on metals that are normally corrosion resistant due to a passive oxide film on the surface. Pits seemingly forming at arbitrary places on the metal surface are actually forming on microscopic cracks or other flaws in the material, like areas with different chemical composition as a result of phase transformations. Pitting is often hard to predict because of rapid propagation and little visible surface signs [24].

The key step of pitting corrosion is the local breakdown of passivity by aggressive anions. Anions are negatively charged ions like  $\text{Cl}^-$ . These penetrate the passive film locally at inclusions, grain boundaries or other weaknesses. The absorption of anions greatly increases the ion transfer ability of the passive film. Hence, the diffusion rate of metal ions to the environment increases, resulting in higher corrosion rates.

Propagation of an initiated pit occurs at a high rate because the small anodic area of the pit is connected to the large cathodic area of the bulk material. Repassivation of the material by reestablishment the passive film is prevented as more anions diffuse into the pit to maintain an electrochemical equilibrium.

Each local corroded area is small in size, and the corrosion or weight loss is usually not noticeable until failure. The corrosion form is not a particular threat to large structures. However, pitting is critical in components designed to isolate the inside from the environment, like pipelines or monitoring instruments [29].

Material selection is the best prevention of pitting corrosion. Alloys containing chromium will have a high resistance to localized corrosion in most environments because of the slow dissolution of Cr(III)-salt in water [28]. Molybdenum will increase pitting resistance, especially in Ni-base alloys [29].

### **2.5.3 Ferric Chloride Solution Corrosion Test (ASTM G48)**

The ASTM G48 corrosion test is increasing in popularity, much due to simple instrument requirements and ease of performance. The test solution containing ferric chloride is similar, although not equivalent, as the environment found in initiated corrosion crevices in ferrous alloys. There is a correlation between performance in the test solution and performance in chloride-rich environments, such as seawater at ambient temperature, making the test results relevant to performance in practice [30].

The test procedure has received some criticism in a previous study [31] regarding the low reproducibility of test results, and a high standard deviation when comparing equivalent materials from different reports. The test cannot be used to evaluate the performance in environments not containing chlorides [30].

The purpose of the test is to decrease the time for pitting or crevice corrosion to initiate. This is achieved by immersing the specimens in a highly corrosive solution at an elevated temperature. The recommended size of the specimen is 25x50 cm. Deviation is acceptable as long as all of the specimens are the same size. "Pickling" of the specimens in acid for a few minutes is used to remove the outer layer of metal along with any contamination.

The test solution is made of 100g ferric chloride is mixed with 900mL of Type IV reagent water. Relevant to this dissertation is Method A of the ASTM G48-11 standard. The procedure specifies the use of a 1000 mL test beaker to hold 600 mL of the test solution. A glass cradle is used to hold the specimen in the test solution [30]. The gap between the specimen and the glass cradle is acts as a crevice for stagnant solution where crevice corrosion may initiate. Pitting corrosion may occur in weaknesses in the weld metal, HAZ or base metal.

The welding standard NORSOK M-601[32] specifies a test solution temperature of 40°C for an exposure time of 24 hours for nickel-base alloys, using ASTM G48. The pass criteria of the NORSOK standard are a weight loss less than 4.0 g/m<sup>2</sup>, and no visible pitting for examinations using ×20 magnifications.

### 3 Experimental

Two precipitation strengthened Ni-base superalloys have been investigated; Inconel 718 and 625 PLUS. The chemical compositions and relevant mechanical properties of the two alloys are presented in Table 3-1 and Table 3-2, respectively. The material certificate for both alloys can be found in Appendix A.

*Table 3-1: Chemical composition (wt%) of the alloys investigated.*

<b>Element</b>	<b>Inconel 718</b>	<b>625 PLUS</b>
Ni	53.30	61.79
Cr	18.35	20.84
Fe	18.71	4.21
Nb	5.09	3.40
Mo	2.91	8.09
Ti	0.96	1.20
Al	0.53	0.19
Co	0.04	-
Si	0.04	0.14
Mn	0.02	0.07
Cu	0.01	0.04
C	0.023	0.015
B	0.0044	0.0020

*Table 3-2: As-delivered mechanical properties of the alloys investigated.*

<b>Mechanical Property</b>	<b>Inconel 718</b>	<b>625 PLUS</b>
Tensile Strength	1242 MPa	1241 MPa
Hardness	345 HV	380–400 HV

### 3.1 Welding Procedures

Components for tensile and corrosion specimens were delivered milled and drilled from a forged bar in the solution annealed and aged condition. Illustrations of the tensile and corrosion specimen components are found in Figure 3-1 and Figure 3-2, respectively. Schematic drawings of all the specimen components are found in Appendix B. Table 3-4 contains a list of all specimens welded.

Each specimen consisted of two cylindrical components; a solid axle with a stepped end made to fit inside a hollow tube. Four tensile specimens and four corrosion specimens was electron beam welded, two of each of the alloys investigated.

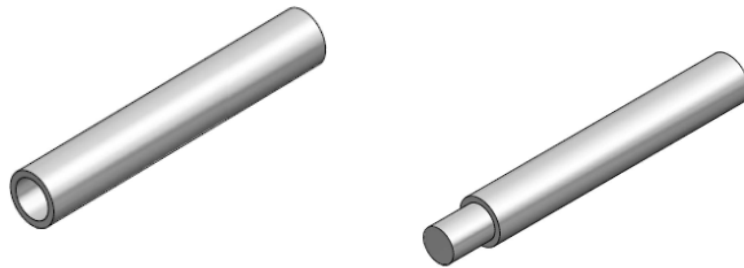


*Figure 3-1: Tensile specimen components.*



*Figure 3-2: Corrosion specimen components.*



*Table 3-3: List of tensile and corrosion specimens.*

<b>Material</b>	<b>Tensile Specimens</b>	<b>Corrosion Specimens</b>
Inconel 718	Inconel 718 No.1	Inconel 718 No. 3
Inconel 718	Inconel 718 No.2	Inconel 718 No. 4
625 PLUS	625 PLUS No.1	625 PLUS No. 3
625 PLUS	625 PLUS No. 2	625 PLUS No. 4

Electron beam welding of all specimens was performed by Roxar, in accordance with the welding procedures developed by the company. The gap separating the two components in the middle was measured to be less than 0.05 mm for every specimen when assembled. Radial butt welds were used to fuse this gap, joining the two components together. The welding parameters of the radial butt welds are stated in Table 3-4.

*Table 3-4: Welding parameters for radial butt welds used on tensile and corrosion specimens.*

<b>Accelerating Voltage</b>	70 kV
<b>Beam current</b>	16 mA
<b>Focus Set Point</b>	1565 mA
<b>Height from Reference Point</b>	396,5 mm
<b>Weld Speed</b>	600 mm/s
<b>Penetration depth, P<sub>D</sub></b>	4.4 mm

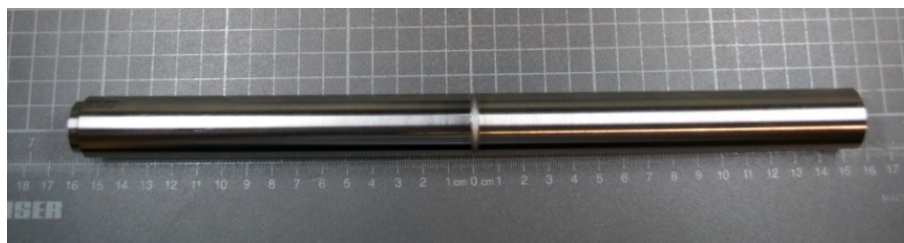


*Figure 3-3: Tensile specimen after electron beam welding and drilling of the weld root. The metal plug is inserted into the hollow end.*

Figure 3-3 shows a welded tensile specimen. The specimens measured 300 mm in length with an external diameter of 25 mm. The motivation for performing the tensile tests was to measure the tensile strength of weld joints exclusively. To achieve this, the stepped end of the solid axle, including the root of the weld bead, was drilled out via the hollow side of the specimens. The hollow part of the specimens extended approximately 30 mm past the weld after drilling, leaving a hollow 7 mm thick weld area to be tested.

A custom made metal plug was placed inside the hollow ends as structural support to avoid deformation of the tensile specimens from the grips of the tensile testing machine.



*Figure 3-4: Corrosion specimen after electron beam welding.*

Figure 3-4 shows a welded corrosion specimen. The specimens measured 40 mm in length with an external diameter of 25 mm. The stepped end of the axle extended through the full length of the hollow tube to form a flat surface at the top of each assembled specimen. The circular gap separating the two components on top could have acted as a site for stagnant solution resulting in crevice corrosion. Miniscule differences in the production of the corrosion specimens could have led to substantial differences in the corrosion in these crevices, skewing the results of the test. To avoid this, the gap was fused using axial butt welds following the welding parameters stated in Table 3-5.

*Table 3-5: Welding parameters for axial butt welds used on corrosion specimens.*

<b>Accelerating Voltage</b>	70 kV
<b>Beam Current</b>	8 mA
<b>Focus Set Point</b>	1565 mA
<b>Height from Reference Point</b>	393 mm
<b>Weld Speed</b>	600 mm/s
<b>Penetration Depth, P<sub>D</sub></b>	2.0 mm

### 3.2 Tensile and Corrosion Tests

The tensile and corrosion tests were performed by Quality Lab in Forsand, Rogaland.

The tensile tests were performed in accordance with standard ISO 6892-1:2009. A tensile test machine from Galdabini with additional software was used measure the tensile strength for both alloys.

The ferric chloride solution corrosion test was performed in accordance with Method A of the ASTM G48 standard. Corrosion specimens were pickled in acid to remove any surface contamination. All specimens were weighed before being exposed to the pre-heated ferric chloride solution and held for the full exposure time. The specimens were rinsed and weighed after the corrosion test in order to observe any weight loss as a result of initiated corrosion. The test parameters that are listed in Table 3-6 is in accordance with NORSOK M-601.

*Table 3-6: Test parameters of the ASTM G48 ferric chloride solution corrosion test.*

Surface Preparation	Test Solution	Solution Temperature	Exposure Time
Pickled in 5 min in 60°C (20% HNO <sub>3</sub> +5% HF)	Ferric Chloride (10% FeCl <sub>2</sub> ·6H <sub>2</sub> O)	40°C	24 hours

### 3.3 Fractographic and Metallographic Preparation

All specimens used for fractographic and metallographic examinations were cut with a Struers Discotom-5 using ample amounts of cooling liquid to prevent heat generation in the metal.

Two different microetchants were used, depending on the objective of the specific examination. The composition and procedure of both etchants are listed in Table 3-7, as well as the etchants application in this dissertation.

Kalling's No. 2 is recommended as a etchant for general purposes by API's standard 6A718 [11], where it is used on as-delivered Inconel 718 for examination of grain boundaries and secondary phases. 10% Chromic Acid has been used in previous experiments by J. N. DuPont [13] for examinations of the dendritic and interdendritic constituents in the weld metal.

*Table 3-7: List of microetchants used for metallographic preparation.*

Etchant	Composition	Procedure	Applications
Kalling's No. 2	200 mL methanol, 200 ml HCl, 10 g CuCl <sub>2</sub>	Swab for 1 min	Investigation of base metal, cross sections of tensile specimens and effect of post-weld heat treatments
10% Chromic Acid	10 mL CrO <sub>3</sub> , 90 mL distilled water	Electroetch at 3 V for 5 sec	Investigation of HAZ and weld metal

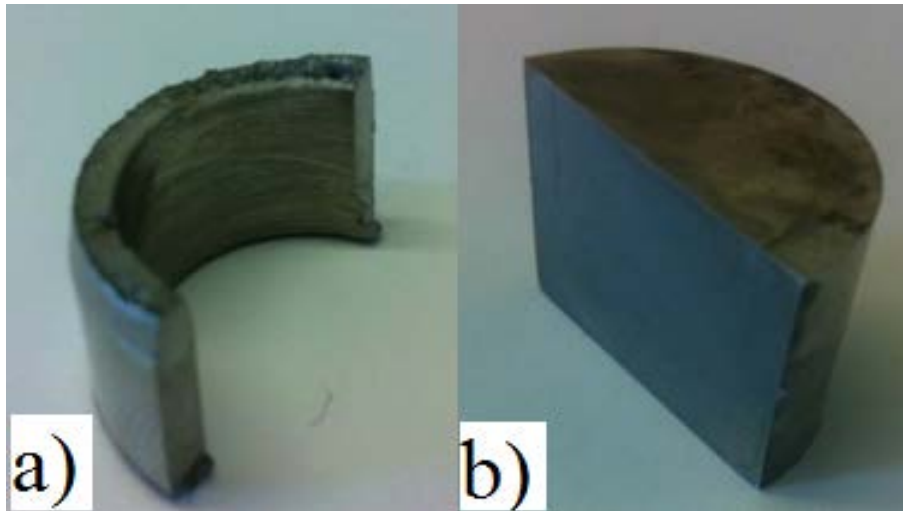


*Figure 3-5: Image of a) Fractographic specimen and b) Microstructure specimen.*

Fractographic specimens were made from fractured tensile specimens. Each specimen were cut 20 mm below the fractured surface, before being cut in half as shown in Figure 3-5a, in order to expose the cross section. The fracture surface was examined before the fracture path. The fractographic specimens were molded in epoxy resin and the cross section was etched to expose the weld metal and HAZ in order to study the fracture path.

Microstructure specimens were made from corrosion specimens after the corrosion test. The microstructure specimens were used for microstructural analysis and hardness measurements. Corrosion specimens were cut in half to expose cross sections of the weld beads on both sides of the specimen, as shown in Figure 3-5b. The specimens were wet-grinded and polished using a Struers Planopol Pademax-2 automatic grinder. Grit 80, 120, 220, 600, 800 and 1000 paper was applied for each grinding step, carefully rinsed with water and soap between. Ethanol was used to remove water from the specimens after the last grinding step. The samples were polished using MD Dur, Mol and Nap cloth for 6 $\mu$ m, 3 $\mu$ m and 1 $\mu$ m diamond particles respectively, while lubricated by Struers DP-Lubricant Blue. Distilled water and ethanol was used to rinse the specimens between each polishing step.

### **3.4 Fractographic and Metallographic Analyses**

A Reichert-Jung MeF3 optical light microscope and a Zeiss Supra 35 VP SEM equipped with an Ametek EDAX spectrometer was used in the fractographic and metallographic analyses.

The fracture surfaces of the fractographic specimens were examined using the secondary electron detector of the SEM. Long work distances (35–40 mm) was used to decrease the beam divergence and increase the depth of focus. The fracture path was examined through an optical light microscopy using low magnification.

The base metal, HAZ and weld metal of each microstructure specimen was examined using the optical light microscope. The weld metal was inspected for signs of solidification cracks and interdendritic constituents. The base metal and HAZ was investigated for any forms of

precipitates or secondary phases like carbides or  $\delta$ -Phase. In addition, the HAZ was investigated for liquation cracks close to the weld metal.

The backscattered electron detector of the SEM was used to investigate the weld metal, HAZ and base metal of the microstructure specimens. The amount of interdendritic constituents was estimated from three consecutive SEM images taken in a straight line using the same magnification down the centerline of the weld metal. A standard image editing program was used to increase the contrast between the dendritic and interdendritic constituents. The software ImageJ was used to adjust the *Threshold* to exclude the dendritic constituents. *Analyze Particles* was used to find the area fraction of interdendritic constituents for each image. The average area fraction was used as an estimate of the total volume fraction of interdendritic constituents in the center of the weld metal for each alloy.

Analysis of characteristic X-ray waves was used for phase identification using the spectrometer installed on the SEM.  $L_{\alpha}$  lines were used for the heavier Mo and Nb elements.  $K_{\alpha}$  lines were used for all other elements as these lines were more comparable with the  $L_{\alpha}$  lines for Mo and Nb.

### 3.5 Post-Weld Heat Treatments

The same post-weld heat treatment procedure was performed on Inconel 718 No. 3 and 625 PLUS No. 3. The specimens were solution annealed at 1040°C for 1 hour before being air cooled to room temperature. A two-step aging procedure was used to promote the formation of the strengthening precipitate  $\gamma''$ . The specimens were held at 720°C for 8 hours, before being furnace cooled at a rate of 50°C/hour to the temperature 620°C. The specimens were held at 620°C for another 8 hours before being air cooled.

Hardness was measured using the Vickers hardness test before and after post-weld heat treatments. Hardness measurements were performed in accordance with ISO 22826 – “Hardness testing of narrow joints welded by laser or electron beam”[33]. Relevant for this dissertation is test type E of the standard. The points of indentation specified in the test type are illustrated in Figure 3-6.

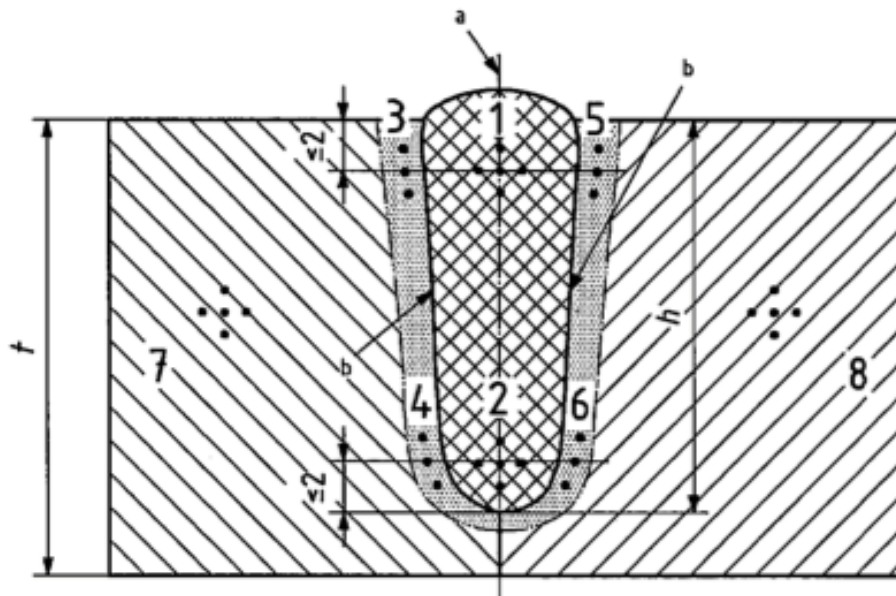


Figure 3-6: Zones and points of indentations for Vickers hardness tests.

The zone configuration is used when the penetration depth of the weld  $h$  is greater than 4 mm. This was the case with our radial butt welds where the penetration depth  $P_d$  was 4.4 mm, as was shown in the welding parameters listed in Table 3-4. The test type defines 8 zones in and around the weld. 5 measurements were taken per zone in a star shape pattern in the weld metal (zone 1 and 2) and base metal (zone 7 and 8). 3 measurements were taken per zone in a straight line following the weld beads longitudinal direction in the HAZ (zones 3-6). The middle indentation of each zone was specified to be no more than 2 mm from the top or bottom of the weld bead, as indicated in Figure 3-6.

The distance,  $L$ , between each indentation was specified to be at least three times the mean diagonal length,  $d_v$ , of the indentations,  $L > 3d_v$ . To accommodate for the dense indentation configuration of the test type, HV1 (1000g) was chosen, as the test force produced indentations with the most appropriate diameter  $d_v$ .

A Struers DuraScan Vickers hardness testing machine was used to perform hardness measurements on three weld areas for both the respective alloys before and after post-weld heat treatments. The specimens were polished and etched to make the identification of weld metal, HAZ and base metal possible.

## 4 Results

### 4.1 Corrosion Test

The results from the ASTM G48 ferric chloride corrosion test are given in Table 4-1. There was no weight loss as a result of the test, and no pitting was visible for either of the alloys. Both welded alloys are approved according to NORSOK M-601.

*Table 4-1: Results of ASTM G48 ferric chloride corrosion test.*

<b>Specimen</b>	<b>Weight Loss</b>
Inconel 718 No.3	0 g
Inconel 718 No.4	0 g
625 PLUS No.3	0 g
625 PLUS No.4	0 g

### 4.2 Tensile Tests and Fractographic Analysis

The results from the tensile tests are stated in Table 4-2. Loss in tensile strength is calculated using the tensile strength stated in the material certificate from each respective alloy.

The tensile strength of the 625 PLUS specimens was consistently higher than the Inconel 718 specimens. On average, 625 PLUS had 73% higher tensile strength than Inconel 718. However, the tensile strength of specimen 625 PLUS No. 1 was measured to almost twice the value of 625 PLUS No. 2, leading to doubts in the statistical precision of the small sample group used.

*Table 4-2: Results from tensile tests.*

<b>Specimen</b>	<b>Tensile Strength</b>	<b>Loss in Tensile Strength</b>
Inconel 718 No. 1	214 MPa	82,77%
Inconel 718 No. 2	142 MPa	88,57%
625 PLUS No. 1	888 MPa	28,44%
625 PLUS No. 2	450 MPa	63,73%

The fracture path was investigated from both fragments of each fractured tensile specimen. The fracture initiated and passed through the weld metal for all specimens. Figure 4-1 shows the typical fracture path of a tensile specimen after etching to expose the weld metal, HAZ and base metal. Typical fracture paths from all specimens are found in the first part of Appendix C.



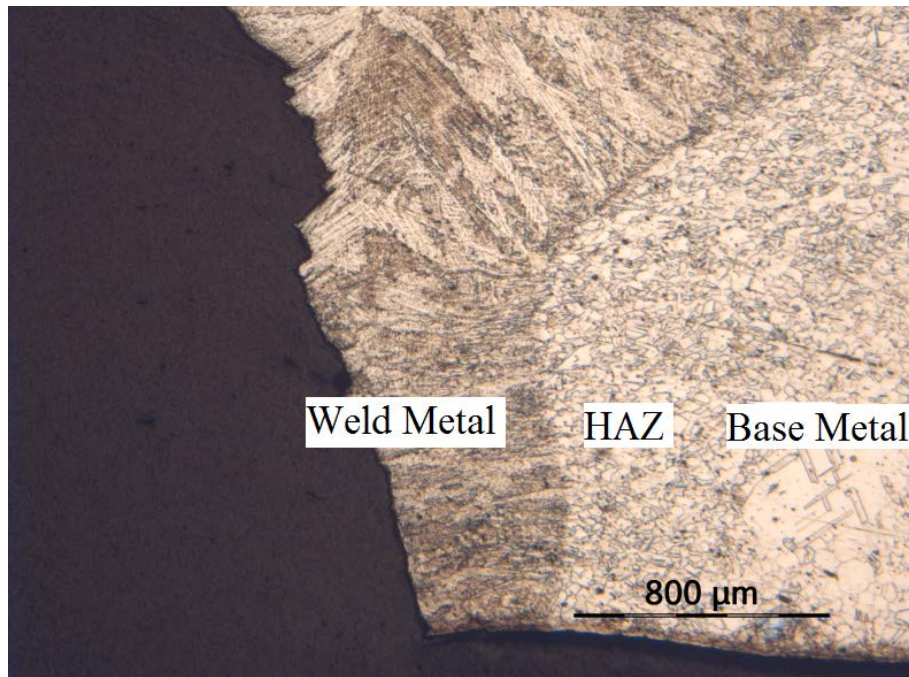


*Figure 4-1: Fracture path of 625 PLUS No. 1.*

The fractographic specimens were investigated using the secondary electron detector of the SEM. Cup-and-cone fractures characteristic of ductile fracture mode was observed for all specimens. The initial fracture initiated on the inner diameter of the specimen and the fracture surface severed perpendicular to the applied tension. This can be seen in Figure 4-2 where the initial fracture appears as a relatively flat surface on the inner diameter visible in the upper end of the figure. Shear lips were visible close to the outer edge of the specimen, where the final separation left a fracture surface 45° to the applied tension, as seen in Figure 4-3.

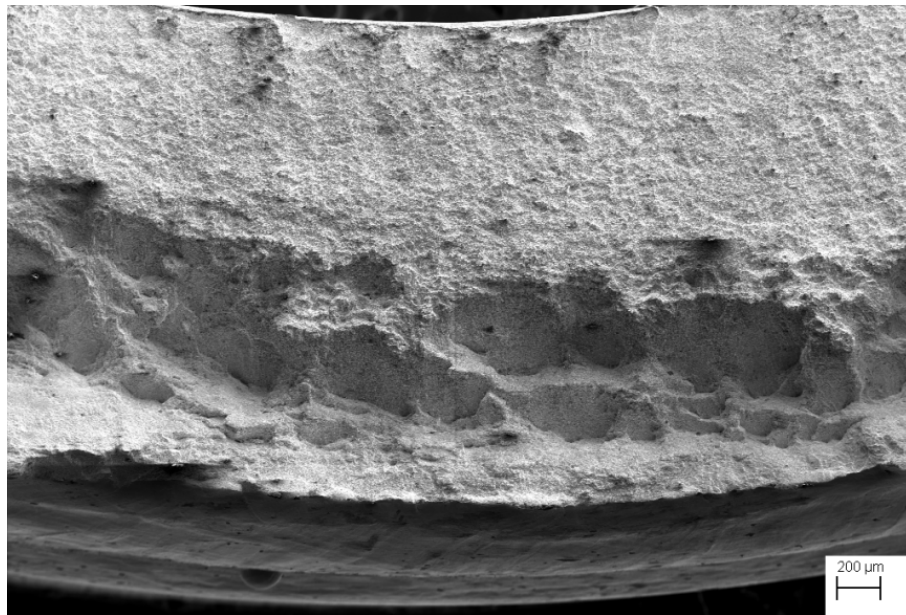


*Figure 4-2: Cup-and-cone fracture of 625 PLUS No. 2.*

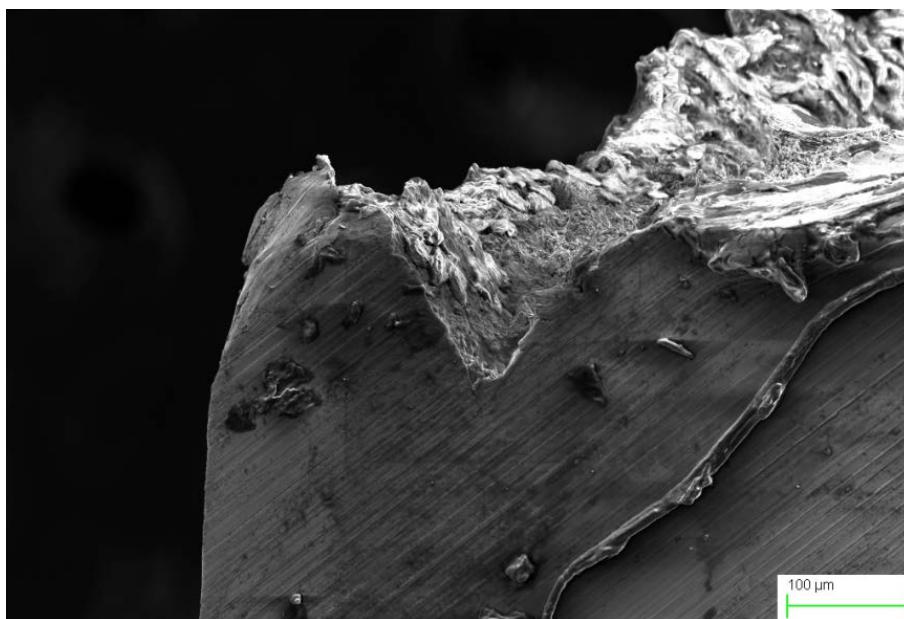


*Figure 4-3: Fraction of shear lips 45° to applied tension in Inconel 718 No. 2.*

The formation of a cup-and-cone fracture and separation of the shear lips typical for all tensile specimens confirmed a ductile fracture mode for the specimens. However, the amount of plastic deformation seen in the fractographs was low, as seen in Figure 4-4 and Figure 4-5. No preferential fracture path of the intervoid material was seen. The dendritic fracture pattern associated with fracture of as-welded superalloys was common in all fractographs. The amount of plastic deformation in the intervoid material seemed higher in the 625 PLUS specimens.

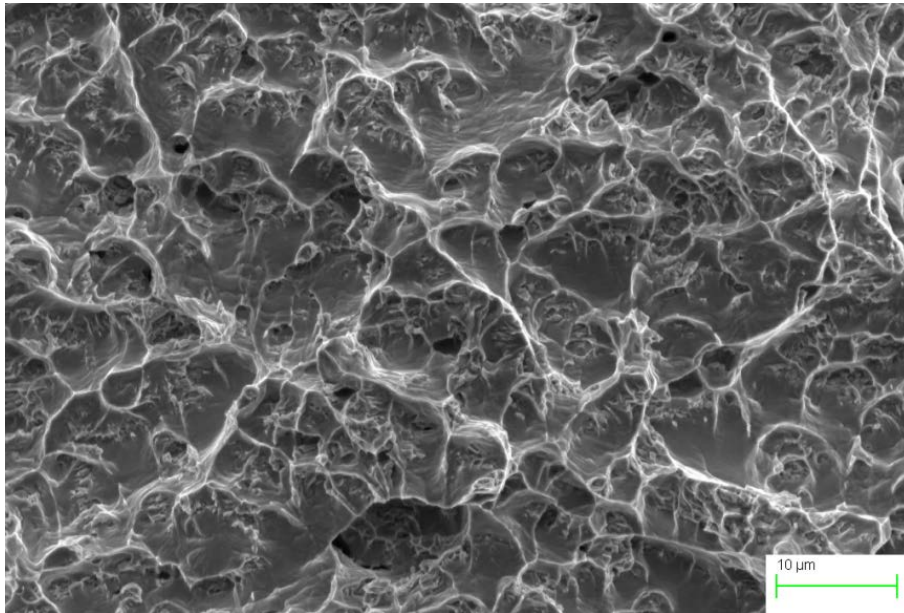


*Figure 4-4: Fractograph of Inconel 718 No. 2.*

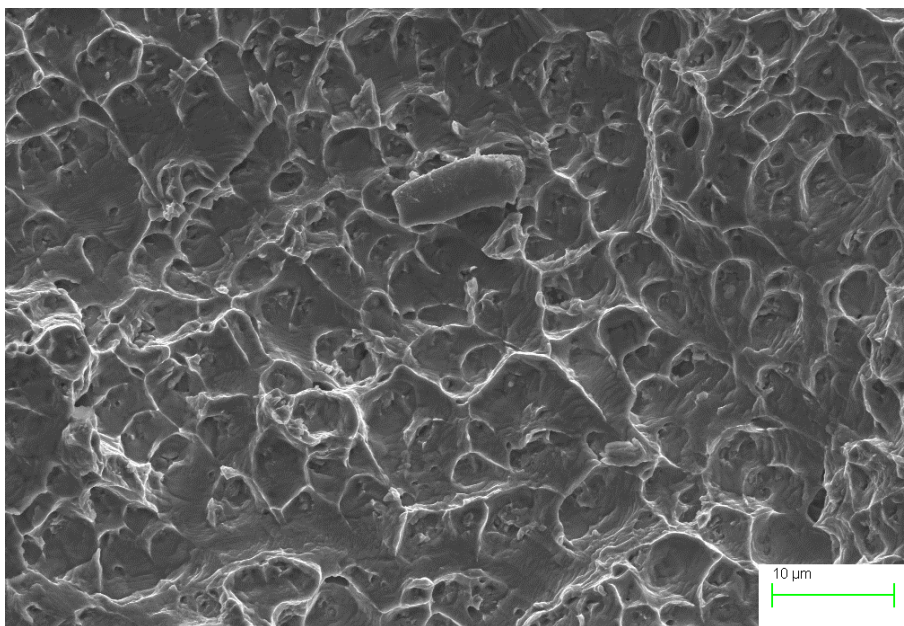


*Figure 4-5: Fractograph of 625 PLUS No. 1.*

The fractograph of Inconel 718 No. 2, found in Figure 4-4, revealed that the amount of plastic deformation of the intervoid material before fracture was particularly low. The size of the voids were also noticeably larger than the 625 PLUS specimens.

The fractograph of the 625 PLUS No. 2, found in Figure 4-5, revealed the highest amount of plastic deformation of the intervoid material before fracture. The voids were noticeably smaller in size compared to Inconel 718 No. 1. In addition, small spherical particles were found in the center of the void in both 625 PLUS fractographs. Fractographs from all tensile specimens can be found in Appendix C.

### **4.3 Microstructural Analysis**

Low magnification optical light microscope images of both alloys can be found in Appendix D.

#### **4.3.1 Base Metal**

No evidence of “needle shaped” acicular  $\delta$ -phase was found in of the base metal in either of the alloys. Carbides were found seemingly arbitrarily and evenly distributed in the base metal of the Inconel 718 specimens, as seen in the optical light microscope image in Figure 4-6. The carbides were generally small in size, around 1  $\mu\text{m}$ . Some larger isolated particles were observed, in the size range of 10  $\mu\text{m}$ .

Small carbides around 1  $\mu\text{m}$  were observed evenly distributed in the base metal of 625 PLUS as well, as seen in the optical light microscope image in Figure 4-7. However, carbides considerably larger in size, between 10  $\mu\text{m}$  and 30  $\mu\text{m}$  were observed in several strings. The strings of large carbides were orientated parallel to the axis of the cylindrical specimens.



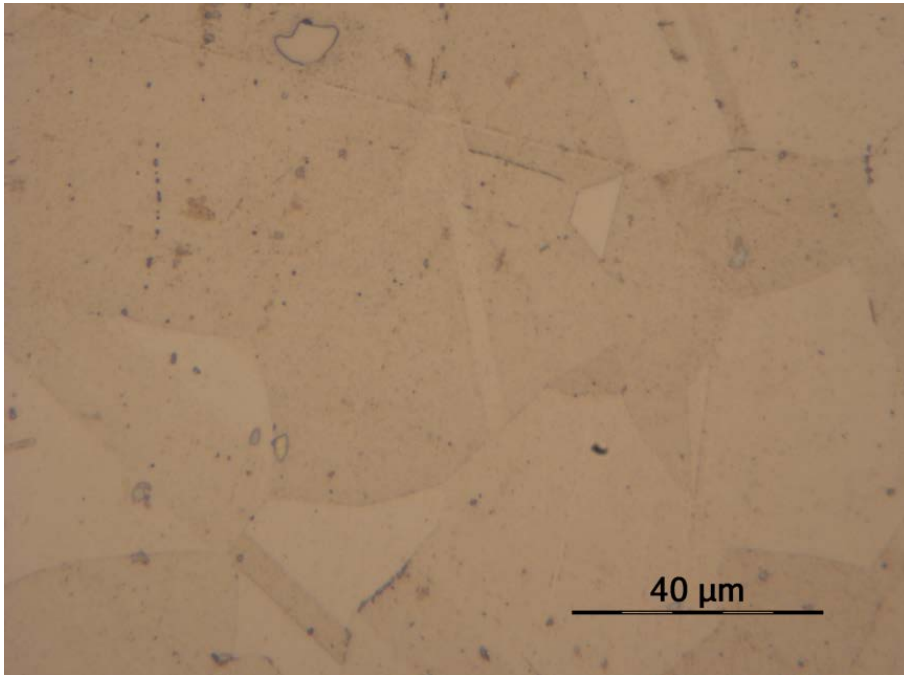


*Figure 4-6: Base metal of Inconel 718 No. 3.*

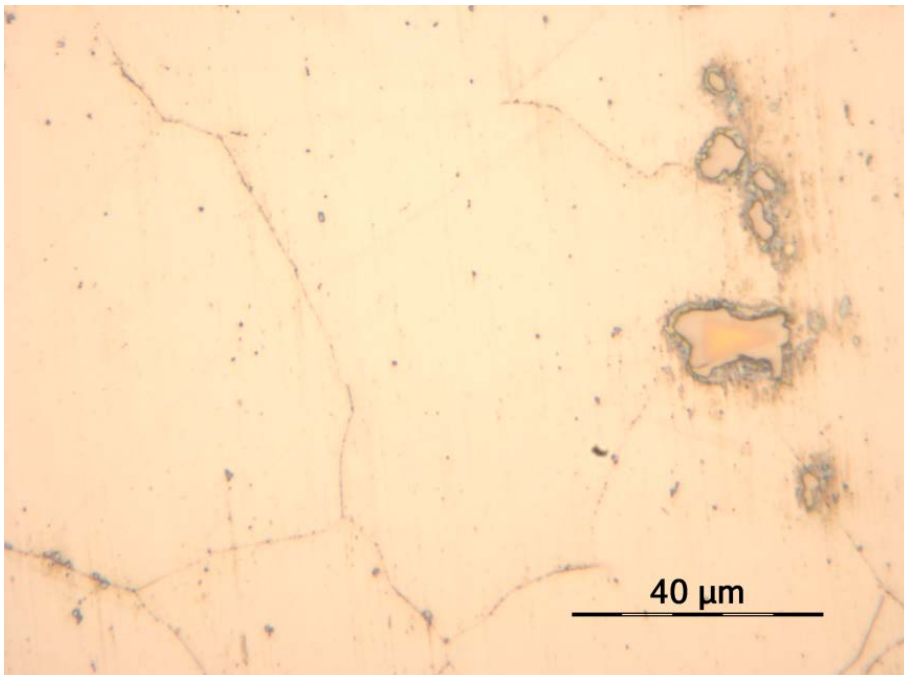


*Figure 4-7: Base metal of 625 PLUS No. 3.*

The carbides were investigated using the backscattered electron detector of the SEM. The bright appearance suggested that heavier elements partitioned in the particles, as seen in the case of Inconel 718 in Figure 4-8. An analysis of the characteristic X-ray waves from the particles was used to determine its chemical composition. The analysis revealed high amounts of Nb and Ti, typical for MC (NbC) carbides. The chemical composition of the MC carbides in both alloys is found in Table 4-3. MC (NbC) carbides were the only carbides found in either alloy.

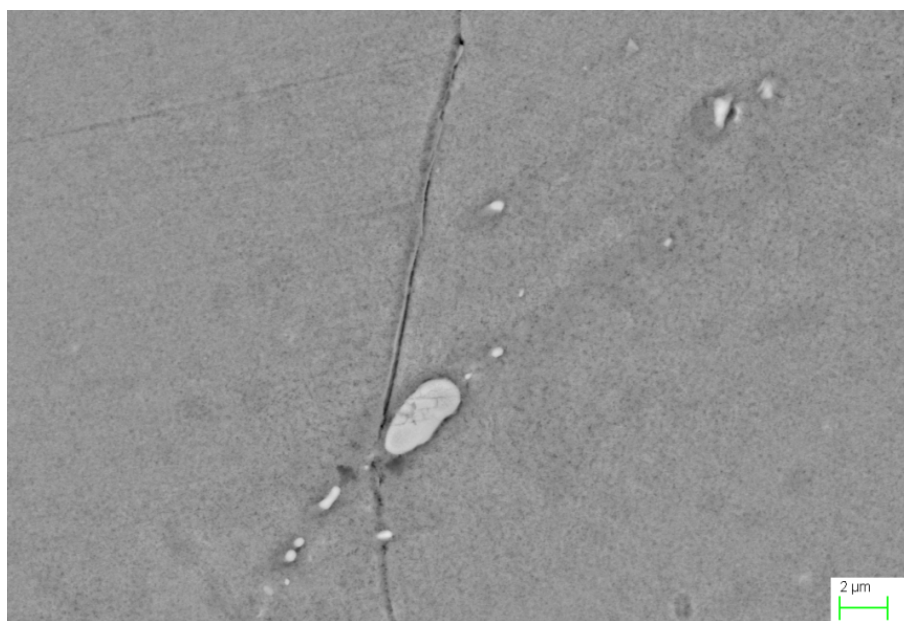


*Figure 4-8: Nb-rich MC carbide in 718 Inconel No. 3.*

*Table 4-3: X-ray analysis of the major partitioning elements (wt%) in MC particles.*

<b>Element</b>	<b>Inconel 718</b>	<b>625 PLUS</b>
Nb	87.07	65.98
Ti	6.88	9.25
Ni	3.57	10.12
Fe	1.57	1.89

Fine globular  $\delta$ -phase was occasionally observed decorating the grain boundaries of both alloys, as seen in the SEM image in Figure 4-9. The phase was identified only by use of the characteristic appearance of the phase. The amounts observed are not thought to be sufficient to inflict any detrimental effect on the mechanical properties.

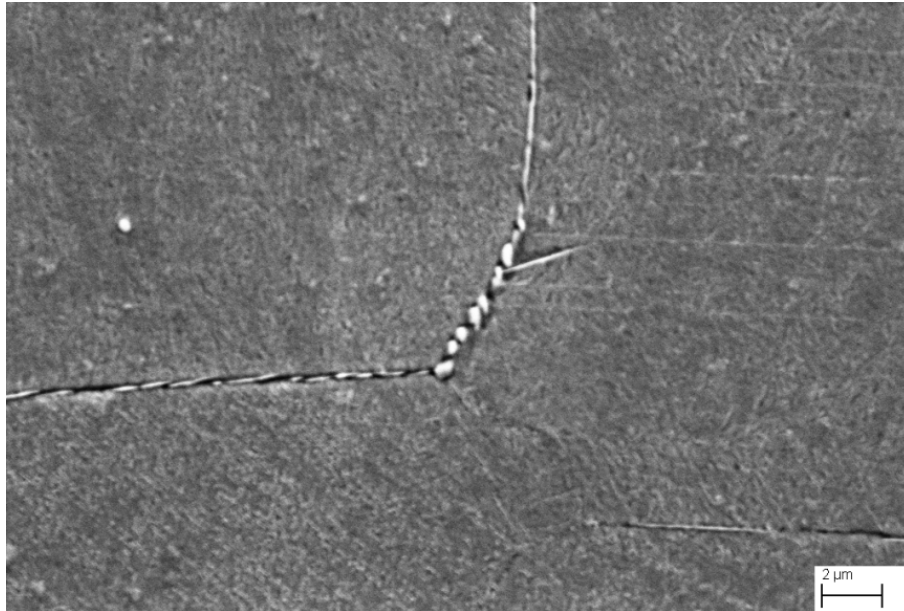


*Figure 4-9: Fine globular  $\delta$ -phase at grain boundary in Inconel 718 No. 3.*



### 4.3.2 Weld Metal

The volume fraction of interdendritic constituents in the weld metal were considerably higher in Inconel 718 when compared to 625 PLUS. The constituents formed as golden bright, thick sections next to the smooth surfaces of the dendrites in both alloys, as seen in optical light microscope images in Figure 4-10 and Figure 4-11 taken around the middle of the weld metal centerline.

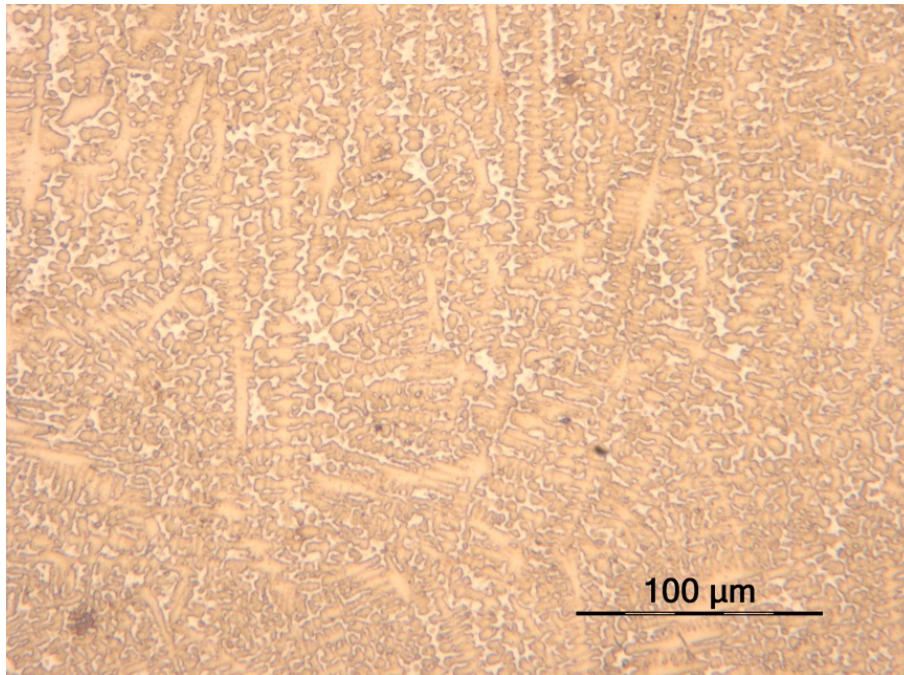


*Figure 4-10: Weld metal of Inconel 718 No. 4.*

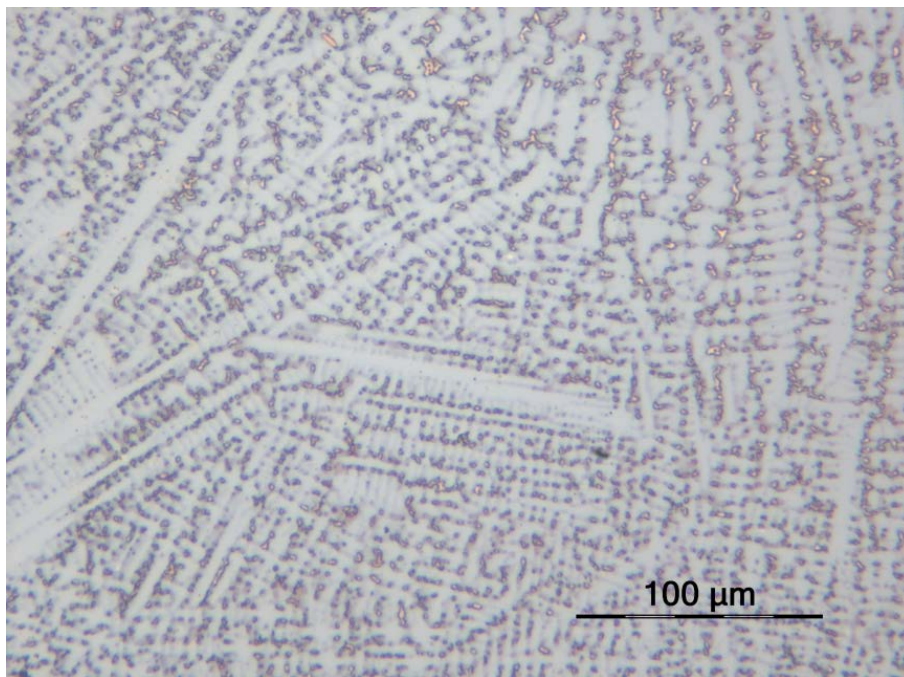


*Figure 4-11: Weld metal of 625 PLUS No. 4.*

An interesting observation is the direction in which the interdendritic constituents tended to solidify, which was in the heat flow direction towards the HAZ and base metal. The dendrites seemed to solidify in more arbitrary directions. The base metals of both alloys are located towards the top and bottom in Figure 4-10 and Figure 4-11, hence the vertical direction of the interdendritic constituents.

An estimate the volume fraction of interdendritic constituents in each alloy is found in Table 4-4. The area fractions of interdendritic constituents were estimated using the backscattered electron detector to form three consecutive images down the centerline of the weld using identical magnifications. An average of the area fraction for both alloys was calculated. Values were consistent as the standard deviation was around 2% for both alloys.

*Table 4-4: Estimated area fraction of interdendritic constituents.*

	<b>Inconel 718</b>	<b>625 PLUS</b>	<b>Difference</b>
Interdendritic Constituents (Area %)	25.6%	13.2%	12.4%

Figure 4-12 and Figure 4-13 shows the constituents present in Inconel 718 and 625 PLUS respectively. The images were taken around the middle of the weld metal centerline using the backscattered electron detector of the SEM. The images suggest a segregation behavior of heavier elements from the dark gray appearing dendritic  $\gamma$  to the brighter eutectic  $\gamma$ /Laves interdendritic constituents. The Laves phase appeared as white sheets or elongated particles in the light gray eutectic  $\gamma$  constituents for Inconel 718. In the case of 625 PLUS, Laves phase appeared in more rounded and discrete particles.

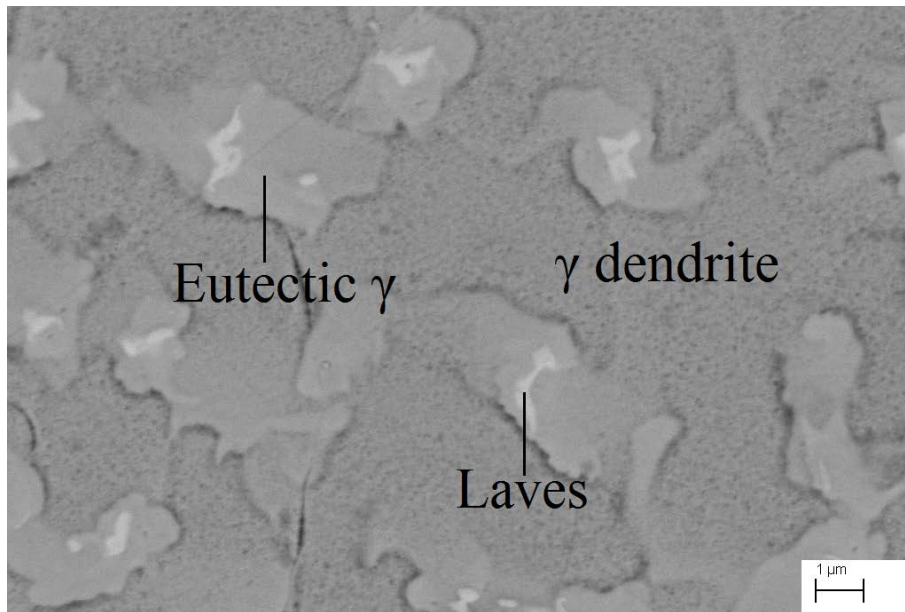


Figure 4-12: Constituents found in the weld metal of Inconel 718 No. 4.

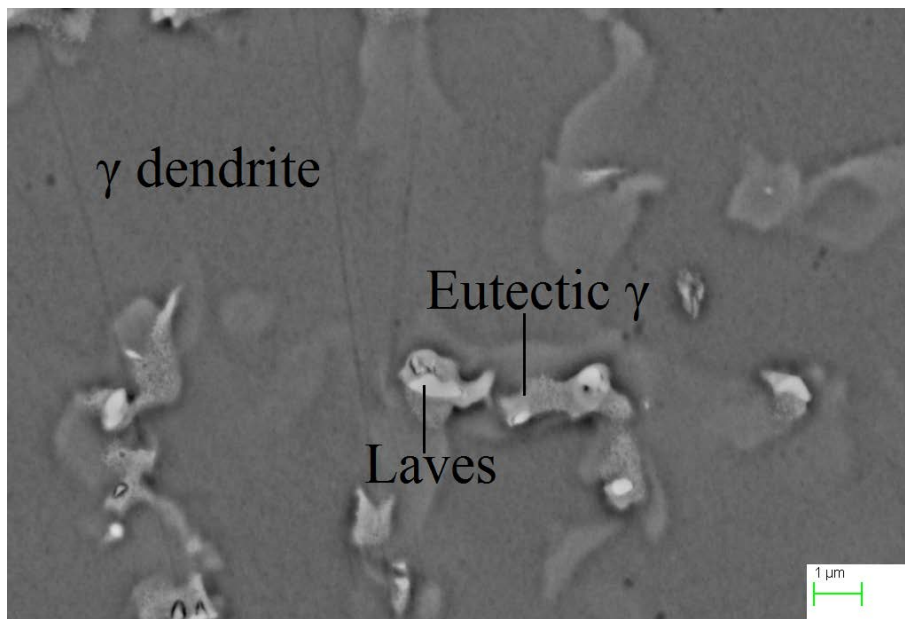


Figure 4-13: Constituents found in the weld metal of 625 PLUS No. 4.

Despite the size variation, the total volume fraction of the Laves phase did not seem to be larger in either of the alloys. However, the volume fraction of the eutectic  $\gamma$  seemed considerable larger in Inconel 718.

An interesting observation is the speckled appearance of small, dark particles in the eutectic  $\gamma$  in Figure 4-13 of 625 PLUS. A previous study [6] on gas-tungsten arc welded 625 PLUS using thin foil specimens investigated in TEM concluded that the particles was  $\gamma''$  in the weld metal.

According to the theory, solidification of the interdendritic constituents is initiated with the eutectic reaction  $L \rightarrow \gamma + \text{NbC}$ . No NbC was found in the weld metal, suggesting that the formation of this phase is low or non-existent during weld solidification.

Characteristic X-ray waves were used to estimate the chemical composition of the dendritic and interdendritic constituents in both alloys. The stoichiometric  $(\text{Fe, Ni, Cr})_2(\text{Nb, Mo, Si})$  nature of Laves made the phase easy to identify. The typical chemical compositions of the weld metal constituents in Inconel 718 and 625 PLUS can be found in Table 4-5 and Table 4-6, respectively. Note that values are given in atomic percent to predict the presence of Laves. Measurements of Si were neglected as neither alloy has appreciable amounts of the element.

*Table 4-5: Chemical composition (at%) of the dendritic and interdendritic constituents in Inconel 718.*

	<b>Ni</b>	<b>Fe</b>	<b>Cr</b>	<b>Nb</b>	<b>Mo</b>
$\gamma$ Dendrites	54.66	19.15	18.89	1.80	2.05
Eutectic $\gamma$	52.58	15.19	17.75	5.89	2.67
Laves Phase	47.63	14.02	16.23	13.10	3.99

*Table 4-6: Chemical composition (at%) of the dendritic and interdendritic constituents in 625 PLUS.*

	<b>Ni</b>	<b>Fe</b>	<b>Cr</b>	<b>Nb</b>	<b>Mo</b>
$\gamma$ Dendrites	63.93	5.15	22.28	1.65	4.70
Eutectic $\gamma$	60.33	5.20	22.23	2.16	6.10
Laves Phase	53.43	4.72	18.88	9.28	9.17

The combination of Nb and Mo in the Laves phase was 17.09 at% and 18.45 at% for Inconel 718 and 625 PLUS, respectively. The expected combined atomic percent of Nb, Mo, Si in the phase is 33 at% according to the stoichiometric  $(\text{Fe, Ni, Cr})_2(\text{Nb, Mo, Si})$  formula. The discrepancy may be due to excitation of the surrounding eutectic  $\gamma$  during the X-ray analysis.

A difference in the chemical composition of the Laves phase was observed for the two alloys, according to Table 4-5 and Table 4-6. Mo seemed to partition even stronger than Nb in the Laves phase of 625 PLUS. This was expected as the Mo content in 625 PLUS is high (8.09 wt%) compared to Inconel 718 (2.91 wt%). The Nb content in the eutectic constituents was higher for Inconel 718. This was expected as the Nb content in Inconel 718 is higher (5.09 wt%) compared to 625 PLUS (3.40 wt%).

An estimate of segregation effect of Nb was calculated. The segregation should be noticeable in a depletion of the element in the dendrite core. The segregation coefficient of Nb is the ratio of the element in the dendrite core over the Nb content of the bulk material. The average of three measurements of the weight percent of Nb in the dendrite cores were compared to the



weight percent of Nb of as-delivered material according to the material certificate. The segregation coefficients for both alloys are listed in Table 4-7.

*Table 4-7: Segregation Coefficients for Nb.*

Segregation Coefficient	Inconel 718	625 PLUS
$K_{Nb}$	0.58	0.84

The low  $K_{Nb}$  of Inconel 718 suggests a higher segregation potential of Nb in the alloy compared to 625 PLUS.

### 4.3.3 Heat Affected Zone

No evidence of “needle shaped” acicular  $\delta$ -phase was found in of the HAZ in either of the alloys. Precipitates of carbides were observed decorating the grain boundaries in the HAZ in amounts and sizes resembling the base metal for both alloys. It is thought that the carbides existed in the area before welding.

HAZ liquation cracking was observed in the entire length of the weld in Inconel 718, increasing in severity near the top of the weld bead in the “nail head” area, as seen in the optical microscope image in Figure 4-14. The image is of the HAZ/weld metal interface in the “nail head” area. The microstructure of the cracks resembles that of the interdendritic constituents in the weld metal.

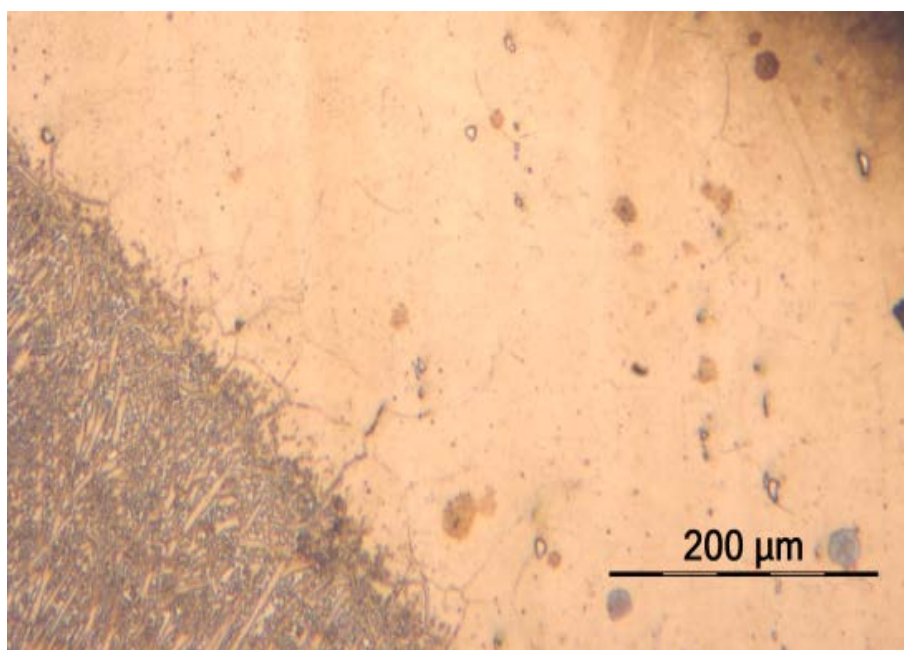


*Figure 4-14: HAZ liquation cracks in Inconel 718 No. 4.*

The liquation cracks in Inconel 718 were investigated using the backscattered electron detector of the SEM. Some crack constituents appeared brighter than the surrounding constituents, as seen in Figure 4-15. The contrast suggests a segregation of the heavier elements. Analysis of the characteristic X-ray waves of the crack constituents was performed

to examine any element segregation. The results from the X-ray analysis are stated in Table 4-8.

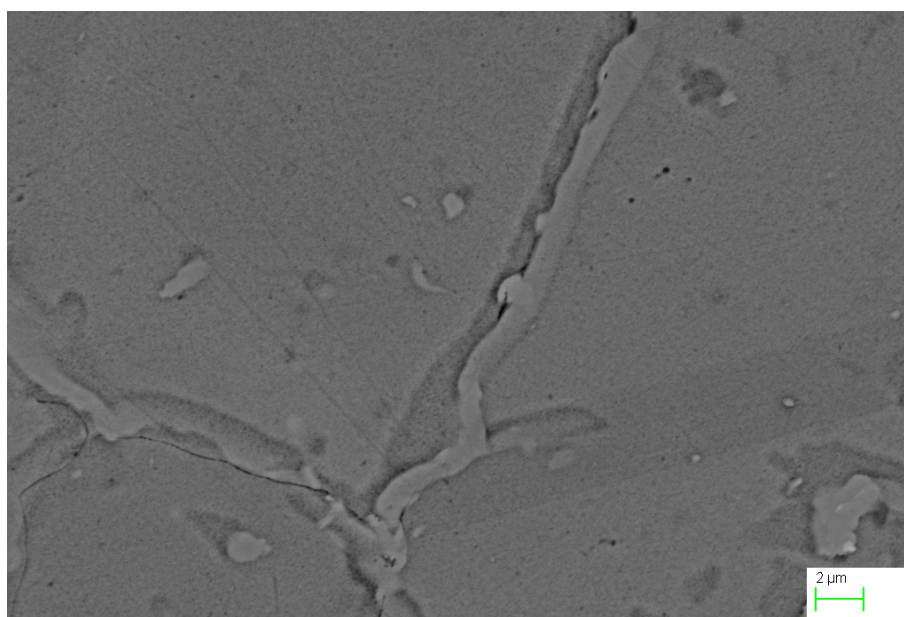


*Figure 4-15: HAZ liquation cracks in Inconel 718 No. 4.*

*Table 4-8: Chemical composition (at%) of the HAZ liquation crack constituents.*

<b>Element</b>	<b>Bright Crack Constituents</b>	<b>Dark Crack Constituents</b>
Nb	4.62	2.87
Mo	2.73	2.63
Ni	52.07	53.60
Fe	18.86	19.19

Note that values are given in atomic percent to be comparable with the weld metal constituents. The analysis of the chemical composition of the crack constituents suggests a solidification mechanism similar to that of the weld metal when compared to Table 4-5 and Table 4-6. This suggests that the bright crack constituents are eutectic  $\gamma$  and the dark constituent is the initially solidified  $\gamma$  (called dendritic  $\gamma$  in the weld metal).

Constituents resembling the brightness of Laves phase were observed on the boundaries of the cracks. However, these constituents were small in size ( $\sim 0.5\mu\text{m}$ ) and few in numbers, making analysis of the characteristic X-ray waves difficult.

The interface between the HAZ and the weld metal of 625 PLUS appeared clean and no appreciable amounts of cracks were observed, as can be seen in the optical light microscope image in Figure 4-16.

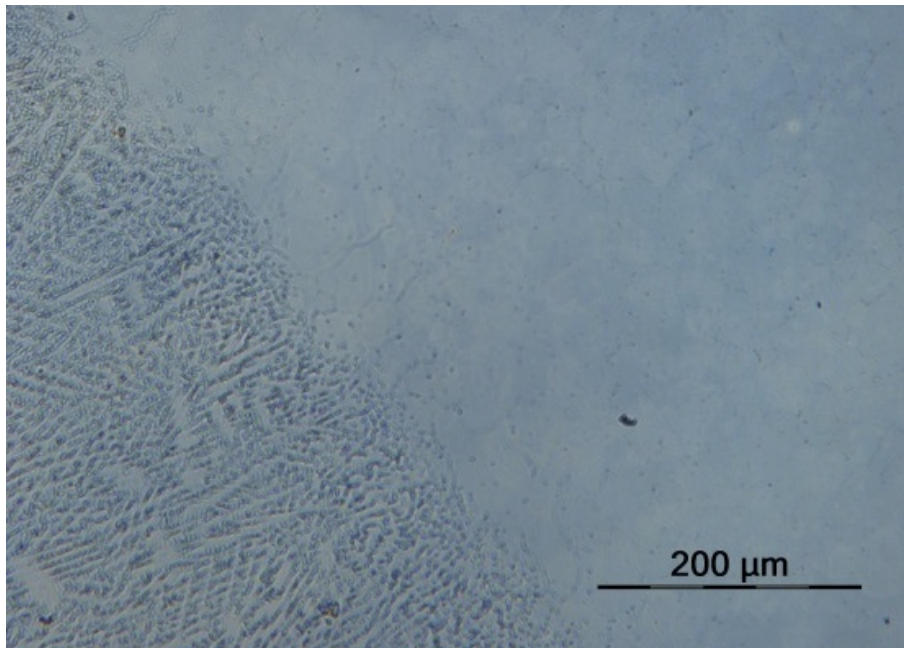


*Figure 4-16: HAZ/weld metal interface of 625 PLUS No. 4.*

#### **4.4 Effect of Post-Weld Heat Treatments**

The microstructure of the weld metal and HAZ was investigated before and after post-weld heat treatments using the optical light microscope. The comparison served as an estimate of the effect of solution annealing in removing the original weld constituents. The largest difference was found in Inconel 718 where most of the original weld metal constituents were dissolved, as seen in Figure 4-17 and Figure 4-18. In addition, the grain sizes were similar to the base metal. A larger amount of carbides was visible after post-weld heat treatments in Inconel 718. The carbides were between 1  $\mu\text{m}$  and 10  $\mu\text{m}$  in size.



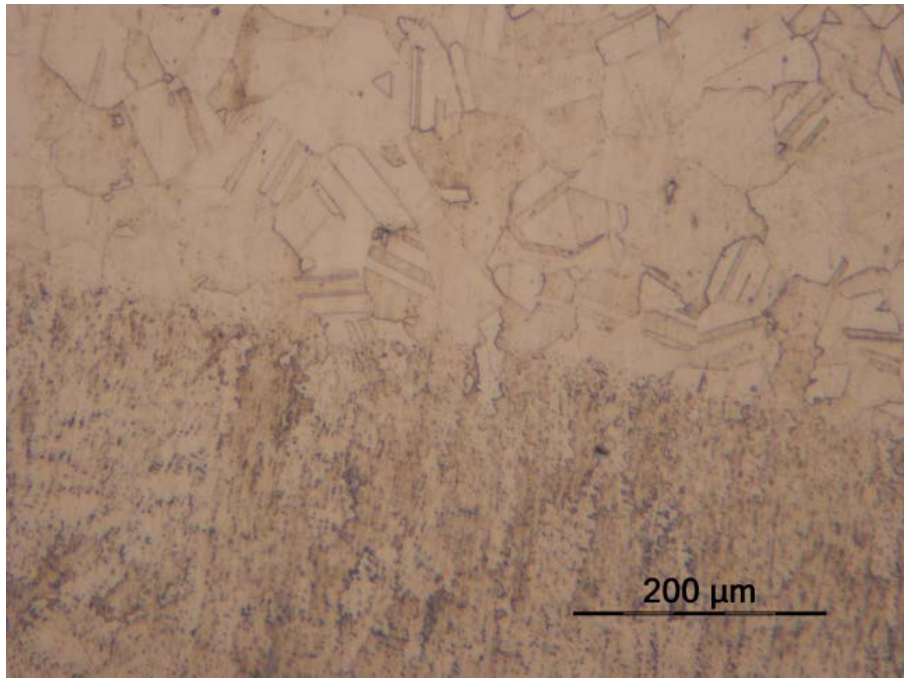


*Figure 4-17: Inconel 718 No. 3 weld metal before post-weld heat treatments.*

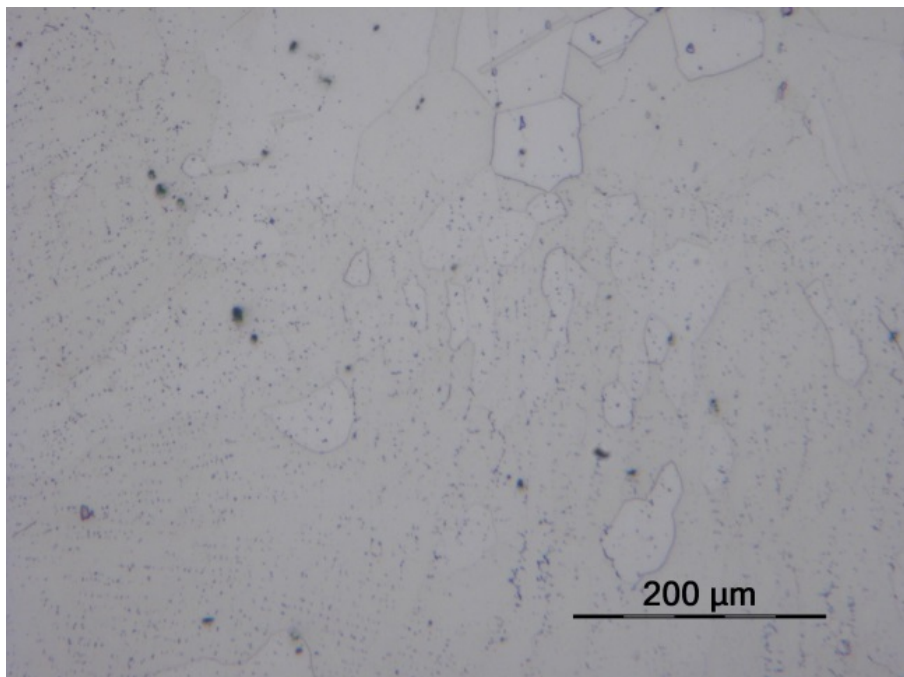


*Figure 4-18: Inconel 718 No. 3 weld metal after post-weld heat treatments.*

The solution annealing dissolved less of the weld metal constituents of 625 PLUS compared with Inconel 718. 625 PLUS before and after post-weld heat treatments can be found in Figure 4-19 and Figure 4-20. The grains in the former weld metal seemed to form in a dendritic pattern, and were inconsistent with the rest of the microstructure. In addition, large amounts precipitates were found on the grain boundaries in the former HAZ and base metal of the post-weld heat treated specimen. The precipitates resemble  $\delta$ -phase.

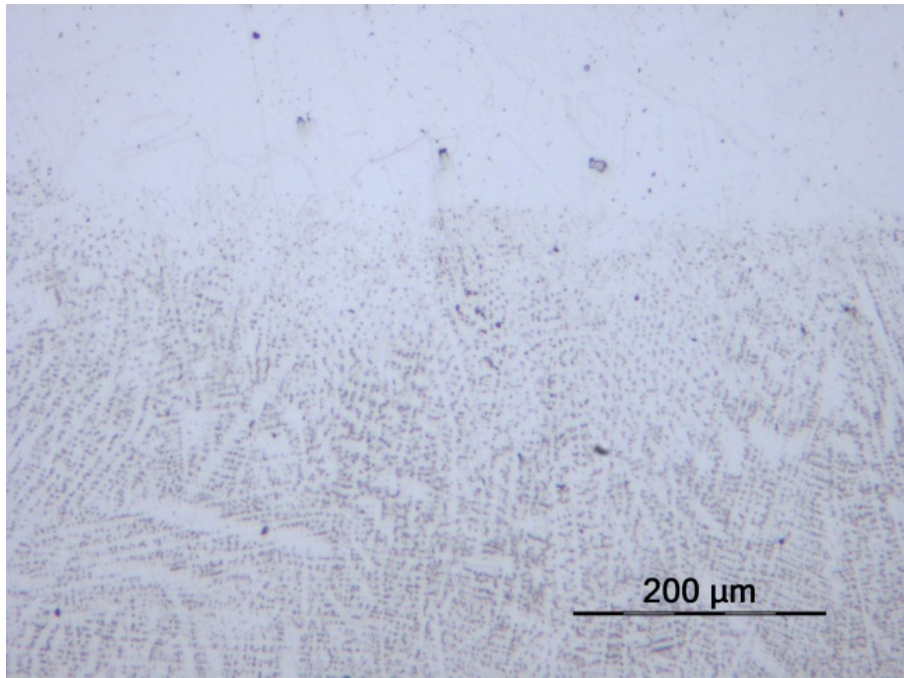


*Figure 4-19: 625 PLUS No. 3 weld metal before post-weld heat treatments.*

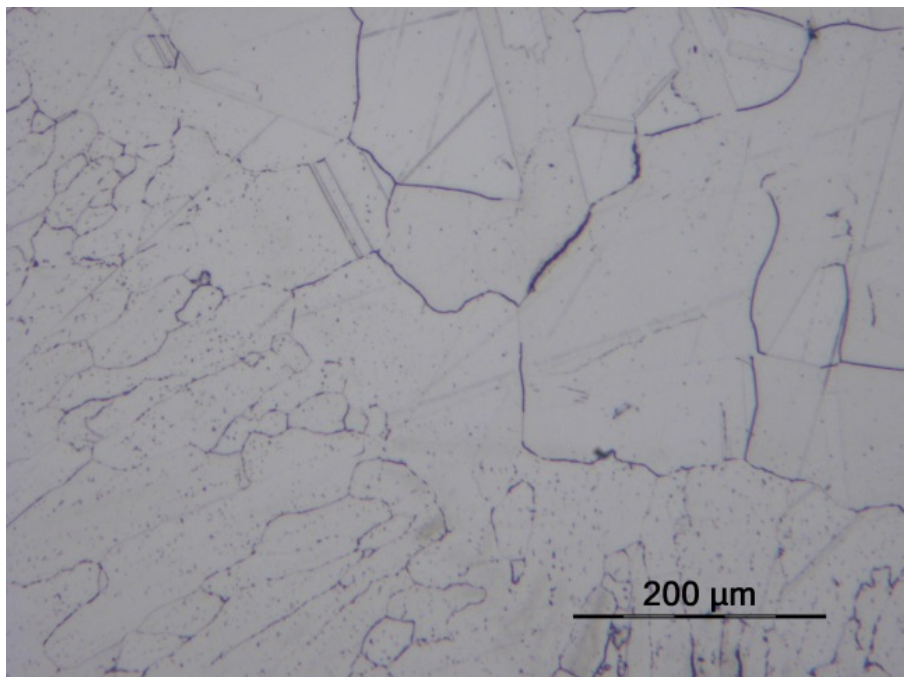


*Figure 4-20: 625 PLUS No. 3 weld metal after post-weld heat treatments.*

The effect aging had on the precipitation of the strengthening phase  $\gamma''$  in the microstructure was estimated using Vickers hardness test measurements before and after the post-weld heat treatments. Hardness values found in Table 4-9 and Table 4-10. Inconel 718 had a higher increase in hardness of the weld metal than 625 PLUS, without losing the hardness in the base metal. A loss in base metal hardness was observed in 625 PLUS. The hardness measurements are presented in accordance with standard ISO 22826 in Appendix E.

Table 4-9: Effect of post-weld heat treatments on the hardness of Inconel 718.

<b>Inconel 718</b>			
<b>Position of indentations</b>	<b>Hardness As-Welded</b>	<b>Hardness Post-Weld Heat Treated</b>	<b>Increase in Hardness</b>
Weld Metal, Top	231.0 HV	385.4 HV	154.4 HV
Weld Metal, Bottom	263.4 HV	413.3 HV	149.9 HV
Base Metal	395.3 HV	396.9 HV	1.6 HV

Table 4-10: Effect of post-weld heat treatments on the hardness of 625 PLUS.

<b>625 PLUS</b>			
<b>Position of indentations</b>	<b>Hardness As-Welded</b>	<b>Hardness Post-Weld Heat Treated</b>	<b>Increase in Hardness</b>
Weld Metal, Top	237.1 HV	347.3 HV	110.2 HV
Weld Metal, Bottom	267.0 HV	354.8 HV	87.8 HV
Base Metal	394.7 HV	339.5 HV	-55.2 HV

## 5 Discussion

### 5.1 Tensile Tests and Fractographic Analysis

The fracture initiated and propagated through the weld metal for all tensile specimens. The fracture surface exhibited the formation of cup-and-cone, a key characteristic of ductile fractures. This was expected as FCC matrixes generally fractures in a ductile manner as a result of the density in slip planes in the crystal structure.

The high tensile strength of 625 PLUS compared to Inconel 718 may be associated with the relatively low volume fraction of interdendritic constituents in the weld metal of the alloy. The fractographs revealed no preferential fracture paths of the voids, but a characteristic dendritic pattern for all tensile specimens. This suggests that the fracture occurred in the interface between the eutectic  $\gamma$  and the  $\gamma$  dendrites.

The embrittling phase Laves is known to be deleterious to tensile strength in superalloys. Crack initiation may have occurred around the Laves phase in the eutectic  $\gamma$ . Although the total volume fraction of the phase seemed similar using the backscattered electron detector, a noticeable difference was found in the morphology of the phase in both alloys. Laves occurred as elongated particles or sheets in Inconel 718 and as rounded, discrete particles in 625 PLUS. The inclusions observed in some of the voids in the 625 PLUS fracture specimens may be residual Laves phase, suggesting that the void nucleated around the particle.

### 5.2 Microstructural Analysis

The large Nb-rich MC carbides found in 625 PLUS are not thought to contribute to any increase in tensile strength. The carbides were found in multiple strings along the cylinder axis in the corrosion specimens, and are thought to be remnants from manufacturing of the wrought bar that the specimens originate from. The fine globular  $\delta$ -phase observed in both alloys is not thought to be detrimental to mechanical properties. No acicular needle shaped  $\delta$ -phase associated, with more severe cases, was found in either alloy.

No solidification cracks were observed in the weld metal of either of the alloys investigated. The low net heat input associated with electron beam welding causes less distortion of the material, lowering the risk of cracking in the weld area.

No NbC was observed, suggesting that formation of the phase in the interdendritic constituents following the reaction  $L \rightarrow \gamma + \text{NbC}$  is low or non-existing during solidification. This is due to the low level of C in both alloys. Solidification terminates in the formation of eutectic  $\gamma$  and Laves phase following the reaction  $L \rightarrow \gamma + \text{Laves}$  in the interdendritic constituents when the remaining liquid contains around 0.03 wt% after the formation of NbC [2]. As both alloys contains less C than 0.03 wt% as-delivered, formation of NbC is not expected.

The volume fraction of the interdendritic constituents was estimated to be 25.6% for Inconel 718 and 13.2% for 625 PLUS. Higher amounts of eutectic  $\gamma$ /Laves in Inconel 718 were expected as a result of the relatively high 5.09 wt% Nb content of alloy, in comparison with the 3.40 wt% Nb of 625 PLUS. Solidification of the interdendritic constituents initiates when the solid solubility of Nb is exceeded for the eutectic  $\gamma$ . Hence, solidification of the interdendritic constituents initiates at an earlier stage during solidification as a result of higher Nb contents (Figure 2-6).

A depletion of Nb in the  $\gamma$  dendrite is expected, as Nb is segregated to the remaining liquid during the initial solidification reaction. However, an increase in segregation behavior of Nb was observed. Estimations of the segregation coefficients  $K_{Nb}$  was made for each alloy using the ratio of measurements of Nb content in the  $\gamma$  dendrite core over the values of the Nb content found in the material certificates. The segregation coefficients would be expected to be similar if no increase in segregation behavior was present. This was not the case in the estimates of  $K_{Nb}$  for the two alloys. The relatively low  $K_{Nb}$  of 0.58 in Inconel 718 suggest a greater segregation of Nb in the alloy, when compared to the  $K_{Nb}$  of 0.84 in 625 PLUS (Table 4-7). Comparing measured values with the material certificate is associated with some degree of error, as the chemical composition of as-delivered alloys may differ from the stated weight percent. However, to achieve equivalent  $K_{Nb}$  to Inconel 718, the weight percent of Nb in 625 PLUS is needed to be unreasonably low, around 1.66 wt%.

The increase in segregation behavior is associated with the relatively high 18.71 wt% Fe in Inconel 718, when compared to the 4.21 wt% Fe in 625 PLUS. A study by J. N. DuPont *et al.* [13] of superalloys varying in chemical composition concluded that an increase in Fe would yield an increase in segregation of Nb to the interdendritic constituents during solidification. The increase in Nb segregation results in larger volume fractions of eutectic constituents as the solid solubility of eutectic  $\gamma$  is reached at an earlier stage in the solidification.

The speckled appearance of small black particles next to the Laves phase in the interdendritic constituents have been identified as  $\gamma''$  in a previous study by M. J Cieslak *et al.* [6] using thin foil specimens examined in a TEM. The presence of the precipitate seems counterintuitive as age hardening at long exposure times is usually needed in order to promote the precipitation of the strengthening phase in the weld metal. However, the high Nb concentration of the region, combined with the relatively slow cooling rate of gas-tungsten arc weldments was sufficient to form the precipitate according to the study. TEM analysis of the 625 PLUS microstructure specimens needs to be conducted to confirm the presence of  $\gamma''$  in the weld metal. No indication of  $\gamma''$  was found in the weld metal of Inconel 718.

HAZ liquation cracking was observed in both Inconel 718 specimens. This was expected from the theory of the cracking susceptibility of Inconel 718. The sharp angle of the weld shape may have played a part in the creation of the cracks in the interface HAZ and weld metal. Welding parameters should be considered changed in order to avoid a sharp “nail head” formation in the shape of the weld.

The chemical composition of the constituents in the liquation crack is not consistent with the theory of NbC liquation at the grain boundaries in the HAZ (Figure 2-10) [15]. Higher amounts of Nb would be expected in the crack, resulting in higher volume fractions of Laves phase. Only small amounts of Laves phase were observed in the liquation cracks of Inconel 718. In addition, liquation cracks would be expected in 625 PLUS as the smaller carbides were found decorating the grain boundaries in similar amounts as Inconel 718. The cracks may be a result of liquation at the grain boundaries in the HAZ which solidifies in a similar manner as the weld metal. Additions of B has been connected to liquation cracking susceptibility [2, 3]. The difference of B in Inconel 718 (0.0044 wt% B) compared to 625 PLUS (0.0020 wt% B) may explain the difference in liquation cracking susceptibility.

### **5.3 Effect of Post-Weld Heat Treatments**

The dissolution of the original weld metal constituents was higher in Inconel 718 when compared to 625 PLUS. This suggests that Inconel 718 has a better response to the solution annealing used.

Inconel 718 had a better response to the aging treatment compared to 625 PLUS. The superior aging response is documented in a previous investigation of both alloys [1]. The superior aging response is a result of higher Nb contents available for  $\gamma''$  in Inconel 718. The loss in base metal hardness in 625 PLUS may be explained by the removal of  $\gamma''$  in the base metal as a result of solution annealing. The slow aging response of the alloy results in lower amounts of re-established  $\gamma''$ .

Different post-weld heat treatments may be more beneficial for 625 PLUS, however the poor aging response of the alloy is well known.

### **5.4 Suggestions for Further Work**

A larger sample group should be used in tensile tests to achieve higher statistical precision. The hollow tube geometry of the tensile specimens may have affected the test results. As the inside of the specimens was removed, far less surface area was left available for void nucleation and growth in the specimen center where the hydrostatic stress is at its highest. The result is less plastic deformation before fracture. Welded plate specimens should be considered as an alternative to hollow cylindrical tubes.

Method F of the ASTM G48-11 standard is designed to find the critical pitting temperature of alloys. The method can be used to distinguish the corrosion resistance of the two candidates, and find the most corrosion resistant as-welded candidate. Decisions regarding corrosion at the current time can only be made from the theory of the superior corrosion resistance of as-delivered 625 PLUS.

Oscillation of the electron beam when welding has successfully been used to control Nb segregation in as-welded Inconel 718 in a previous experiment [17]. The beam was oscillated in different patterns where elliptical oscillation was shown to be the most beneficial technique. As a result, specimens welded using an elliptical oscillated beam had far less Laves formation and improved tensile behaviors when compared to direct beam welded specimens. Oscillation of the electron beam when welding should be investigated as an alternative to cases that restricts the use of post-weld heat treatments.

## 6 Conclusion

The weldability of 625 PLUS was shown to be superior to Inconel 718. Solidification of these alloys terminates in the formation of eutectic  $\gamma$ /Laves next to the  $\gamma$  dendrites. The volume fraction of eutectic  $\gamma$ /Laves was estimated to be twice as high in Inconel 718 when compared to 625 PLUS. This is a result of the high Nb content in the Inconel 718, and the increase in segregation of Nb promoted by Fe additions. Liquation cracks were found in the HAZ of Inconel 718, increasing in severity in the “nail head” area. The constituents in the crack resembled the constituents found in the weld metal. No indication of liquation cracks were found in 625 PLUS.

The lower amount of interdendritic constituents in 625 PLUS resulted in a 73% higher average tensile strength of the weld area than Inconel 718. Cup-and-cone formation characteristic for ductile fracture mode was present in both alloys. Fractographic examination revealed smaller voids and larger amounts of plastic deformation of the intervoid material of the fracture surface of 625 PLUS compared to Inconel 718.

The response to post-weld heat treatments was found to be superior in Inconel 718 compared to 625 PLUS. Most of the original weld metal constituents in Inconel 718 were dissolved, and the grains in the former weld metal were consistent with the rest of the specimen. The alloy had a higher increase in weld metal hardness without a loss of base metal hardness. A noticeable loss in base metal hardness was found in 625 PLUS.



## 7 References

- [1] R. B. Frank, "Custom Age 625 PLUS - A Higher Strength Alternative to Alloy 625," *The Minerals, Metals & Materials Society: Superalloys 718, 625 and Various Derivatives*, pp. 879-893, 1991.
- [2] J. N. DuPont, J. C. Lippold, and S. D. Kiser, *Welding Metallurgy and Weldability of Nickel-Base Alloys*. Hoboken, NJ: John Wiley & Sons, 2009.
- [3] R. Vincent, "Precipitation Around Welds in the Nickel-Base Superalloy Inconel 718," *Acta Metallurgica*, vol. 33, pp. 1205-1216, 1985.
- [4] A. Lingenfelter, "Welding of Inconel 718 - A Historical Overview," *The Minerals, Metals & Materials Society: Inconel 718 - Metallurgicy and Applications*, pp. 673-683, 1989.
- [5] R. B. Bhavsar, A. Collins, and S. Silverman, "Use of Alloy 718 and 725 in Oil and Gas Industry," *The Minerals, Metals & Materials Society: Superalloys 718, 625 706 and Various Derivatives* pp. 47-55, 2001.
- [6] M. J. Cieslak, T. J. Headley, and R. B. Frank, "The Welding Metallurgy of Custom Age 625 PLUS Alloy " *Welding Research Supplement*, pp. 473-482, 1989.
- [7] C. T. Sims and W. C. Hagel, *The Superalloys*. New York: John Wiley & Sons, 1972.
- [8] J. Andersson, "Weldability of Precipitation Hardening Superalloys - Influence of Microstructure," Doctor of Philosophy, Materials and Manufacturing Technology, Chalmers University of Technology, Göteborg, Sweden, 2011.
- [9] S. Azadian, L. Y. Wei, and R. Warren, "Delta Phase Precipitation in Inconel 718," *Materials Characterization*, vol. 55, pp. 7-16, 2004.
- [10] M. Dehmas, J. Lacaze, A. Niang, and B. Viguier, "TEM Study of High-Temperature Precipitation of Delta Phase in Inconel 718 Alloy," *Advances in Material Science and Engineering*, pp. 1-9, 2011.
- [11] A. P. Institute, "Nickel Base Alloy 718 (UNS N07718) for Oil and Gas Drilling and Production Equipment," ed, 2010.
- [12] G. D. J. Ram, A. V. Reddy, K. P. Rao, G. M. Reddy, and J. K. S. Sundar, "Microstructure and Tensile Properties of Inconel 718 Pulsed Nd-YAG Laser Welds," *Journal of Materials Processing Technology*, vol. 167, pp. 73-82, 2005.
- [13] J. N. DuPont, C. V. Robino, J. R. Michael, M. R. Notis, and A. R. Marder, "Solidification of Nb-Bearing Superalloys: Part I. Reaction Sequences," *Metallurgical and Materials Transactions A*, vol. 29A, pp. 2785-2796, 1998.
- [14] L. R. Liu, T. Jin, N. R. Zhao, X. F. Sun, H. R. Guan, and Z. Q. Hu, "Formation of Carbides and Their Effects on Stress Rupture of a Ni-Base Single Crystal Superalloy," *Materials Science and Engineering: A*, vol. 361, pp. 191-197, 2003.
- [15] R. G. Thompson and S. Genculu, "Microstructural Evolution in the HAZ of the Inconel 718 and Correlation with the Hot Ductility Test," *Welding Journal*, pp. 337-345, 1983.
- [16] C. H. Radhakrishna and K. P. Rao, "The Formation and Control of Laves Phase in Superalloy 718 Welds," *Journal of Material Science*, vol. 32, pp. 1977-1984, 1997.
- [17] G. M. Reddy, C. V. S. Murthy, K. S. Rao, and K. P. Rao, "Improvement of Mechanical Properties of Inconel 718 Electron Beam Welds - Influence of Welding Techniques and Postweld Heat Treatment," *The International Journal of Advanced Manufacturing Technology*, vol. 43, pp. 671-680, 2009.

- [18] H. J. Stone, S. M. Roberts, and R. C. Reed, "A Process Model for the Distortion Induced by the Electron Beam Welding of a Nickel-Based Superalloy," *Metallurgical and Materials Transactions A*, vol. 3A, pp. 2261-2273, 2000.
- [19] H. Schultz, *Electron Beam Welding*. Cambridge, England: Abington Publishing, 1993.
- [20] H. B. Cary, *Modern Welding Technology*, 2 ed. New Jersey: Regents Prentice Hall, 1989.
- [21] J. Huang, "The Characterization and Modelling of Porosity Formation in Electron Beam Welded Titanium Alloys," Doctor of Philosophy, University of Birmingham, 2011.
- [22] J. Norrsih, *Advanced Welding Processes*. Bristol: Institute of Physics Publishing, 1992.
- [23] C. Lampa, A. F. H. Kaplan, J. Powel, and C. Magnusson, "An Analytical Thermodynamic Model of Laser Welding," *Journal of Physics D: Applied Physics*, vol. 30, pp. 1293-1299, 1997.
- [24] J. W. D. Callister, *Materials Science and Engineering - An Introduction*, 7th ed. New York: John Wiley & Sons, 2007.
- [25] T. L. Anderson, *Fracture Mechanics – Fundamentals and Applications*, 3rd ed. Boca Raton, FL: CRC Press, 2005.
- [26] D. Hull, *Fractography – Observing, Measuring and Interpreting Fracture Surface Topography*. Cambridge, UK: Cambridge University Press, 1999.
- [27] N. Perez, *Electrochemistry and Corrosion Science*. Hingham, USA: Kluwer Academic Publishers, 2004.
- [28] P. Marcus, *Corrosion Mechanisms in Theory and Practice*, 2nd ed. New York: Marcel Dekker, Inc, 2002.
- [29] E. Bardal, *Korrosjon og Korrosjonsvern*, 2nd ed. Trondheim: Tapir Forlag, 2001.
- [30] ASTM, "Standard Test Methods for Pitting and Crevice Corrosion Resistance of Stainless Steels and Related Alloys by Use of Ferric Chloride Solution," ed, 2011.
- [31] H. Zitter, G. Mori, G. Hochörtler, and H. Wieser, "Evaluation of CPT Values Determined by ASTM G48 Practice," *Materials and Corrosion*, vol. 53, pp. 37-43, 2002.
- [32] NORSOK, "Welding and Inspection of Piping," ed, 2008.
- [33] ISO, "Destructive Tests on Welds in Metallic Materials - Hardness Testing of Narrow Joints Welded by Laser and Electron Beam (Vickers and Knoop Hardness Test)," ed, 2005.

# Appendix A: Material Certificates

## Inconel 718

**VILLARES METALS**

SUMARÉ PLANT/HEAD OFFICE  
R. Alfredo Dumont Villares, 155  
13177-900 - Sumaré - SP - BRAZIL  
Phone: 55 19 3303-8000 - Fax 55 19 3303-8698  
e-mail: metals@villaresmetals.com.br

MS-nummer

€ - 159910

Pag. 1/ 2

### INSPECTION CERTIFICATE

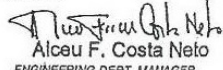
CERT. Nr. 00000619572

ACC. TO EN 10204 3.1

CUSTOMER **VILLARES METALS INTERNATIONAL B.V.**

INVOICE 0000413E12

PURCHASE ORDER Nr./ITEM/VMI-4501758630 / SH-800728- / 19.10.2011


VILLARES METALS REFERENCES									
JOB ORDER Nr (OS) 1524374			LOT Nr. 1524374			PACKAGE Nr. 1524374/01			
VILLARES GRADE VA7718A					SIMILAR GRADE ALLOY 718/UNS N07718				
SPECIFICATIONS M40910 / L,NACE MR0175 /2003									
MELTING PROCESS VM + VAR		PRODUCT LINE Hot Rolled			HEAT TREATMENT CONDITION Solution Treated and Aged			FINISHING Pepled	
NET WEIGHT 522 KG	QUANTITY 27	PRODUCT Round Bar			DIMENSIONS 25,40 (+)0,000 (+)0,130		(mm)		LENGHT RANGE (mm) 3.000 / 5.000
CHEMICAL COMPOSITION (% In weight)					HEAT Nr. 5702342				
C 0.023	Si 0.04	Mn 0.02	P <0.005	S <0.0010	Co 0.04	Cr 18.36	Mo 2.91	Ni 53.3	Cu 0.01
Ti 0.96	Nb 6.04	Al 0.63	B 0.0044	Pb <0.0001	Bi <0.00003	Se <0.0003	Ta <0.05	Mg <0.0010	Ca <0.0005
Fe 18.71 Nb+Ta 6,00000									
Visual And Dimensional Inspections Result: Approved									
Anti-Mixture Testing Result: Approved									
Ultra Sonic Test According to Specification ASTM A388 Result: Approved									
Grain Size According to Specification ASTM E112 Result: Approved : GRAIN SIZE RESULT: 2/4 ASTM									
Microstructure Result: Approved : FIG'S 1 E 2 . MICROSTRUCTURE IS FREE FROM CONTINUOUS NETWORKS OF SECONDARY PHASES ALONG GRAIN BOUNDARIES, ACICULAR DELTA PHASE AND LAVES PHASE.									
Heat Treatment Cycle According to Specification API6A Cycle 1: Solution Annealing Furnace 1: FORNO Nº 07 Load 1: CARGAN Nº 96 Temperature 1: 1040 °C Time 1: 2,0 Hours Cooling Media 1: Water Cycle 2: Aging Furnace 2: 811 Load 2: 1201 Temperature 2: 788 °C Time 2: 7,17 Hours Cooling Media 2: Air ACCORDING API6A 718.									
Macrographic Test According to Specification ASTM A804 Result: Approved Severity: 1A/2A/3A/4A INGOT TOP.									
OUR MANAGEMENT SYSTEM IS CERTIFIED ACCORDING TO ISO 9001, TS16949, NBR15100 (AS9100), ISO14001 AND NADCAP(®).							24.04.2012  Alceu F. Costa Neto ENGINEERING DEPT. MANAGER		
(*)HEAT TREATMENT AND NON DESTRUCTIVE TEST.									





SUMARÉ PLANT/HEAD OFFICE  
R. Alfredo Dumont Villares, 155  
13177-900 - Sumaré - SP - BRAZIL  
Phone: 55 19 3303-8000 - Fax: 55 19 3303-8696  
e-mail: metais@villaresmetals.com.br

**INSPECTION CERTIFICATE**

CERT. Nr. 000000619572

ACC. TO EN 10204 3.1

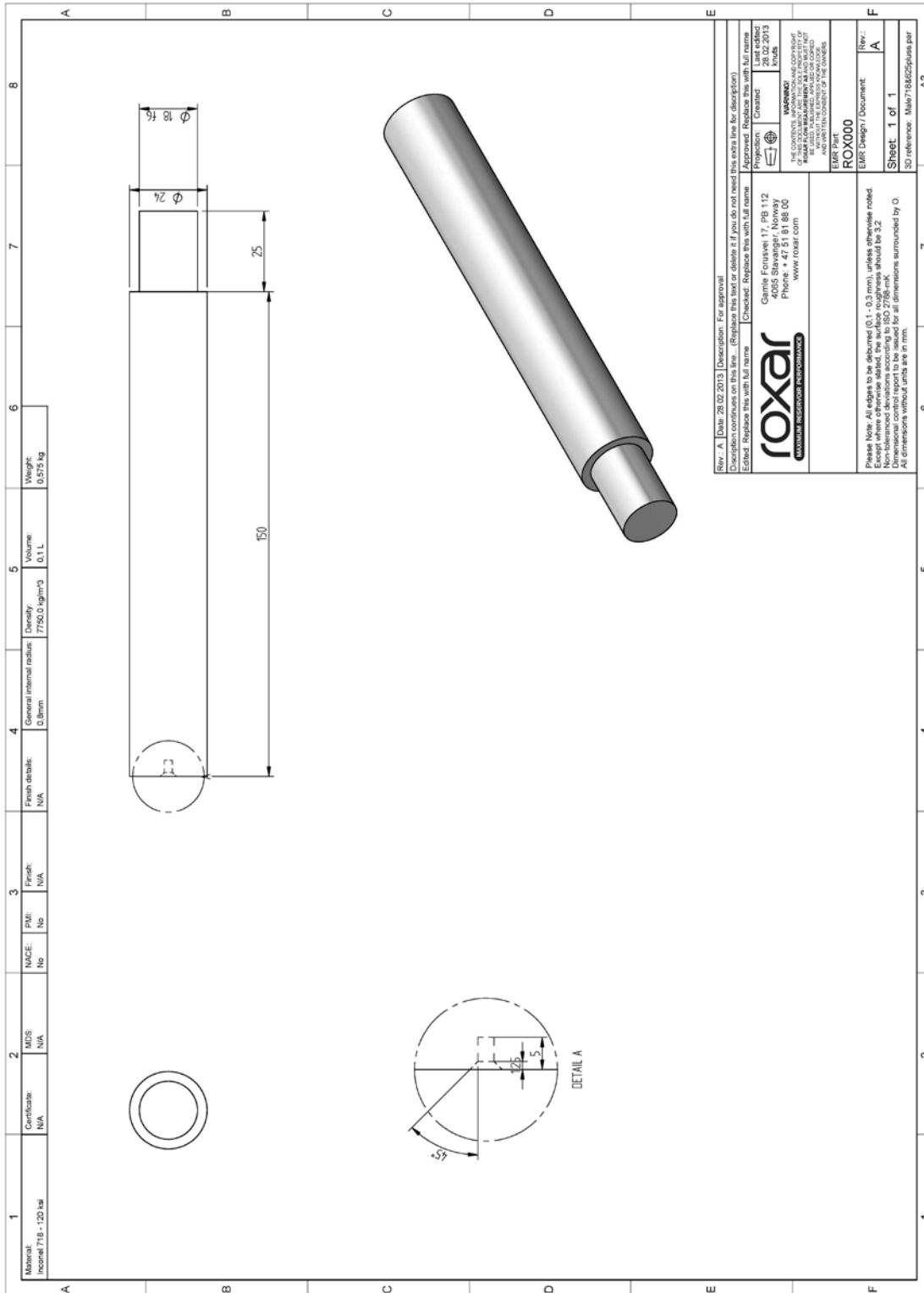
<p><b>Tensile Test - longitudinal</b> According to Specification ASTM A370</p> <p>Specimen #: 6535 Position: LONGITUDINAL Temperature: 22,50 °C Rupture strength: 16910 kgf Yield strength: 11800 kgf Dimension: 12,61 mm Final Dim.: 8,86 mm Initial Length: 60,00 mm Final Length: 65,60 mm Tensile Strength: 1242 MPa Yield Strength 0,2%: 927 MPa Reduction of Area: 60,8 % Elongation: 31,2 % ELONGATION 4D.</p>	
<p><b>Impact Test</b> According to Specification ASTM A370</p> <p>Specimen #: 6535 Test Specimen Type: Charpy-V Temperature: -60 °C Direction: Longitudinal Individual result 1A: 118,90 J Individual Result 1B: 114,50 J Individual Result 1C: 114,30 J Average Result 1: 115,90 J Lateral Expansion (mm): 1,12 mm</p>	
<p><b>Grain Size</b> According to Specification ASTM E1181</p> <p>Result: Approved</p>	
<p><b>Hardness</b> According to Specification ASTM E18</p> <p>Result: 35 HRC</p> <p>*MID-RADIUS POSITION.</p>	
<p><b>Macrographic Test</b> According to Specification ASTM A604</p> <p>Result: Approved Severity: 1A/2A/3A/4A</p> <p>INGOT BOTTOM.</p>	
<p><b>Hardness</b> According to Specification ASTM E18</p> <p>Result: 40 HRC</p> <p>*SURFACE POSITION.</p>	
<p><b>REMARKS</b></p> <p>1. CHEMICAL COMPOSITION ACCORDING TO ASTM B537.</p>	
<p>OUR MANAGEMENT SYSTEM IS CERTIFIED ACCORDING TO ISO 9001, TS16949, NBR15100 (AS9100), ISO14001 AND NADCAP(*)</p>	<p>24.04.2012</p> <p> Alceu F. Costa Neto ENGINEERING DEPT. MANAGER</p>
<p>(*) HEAT TREATMENT AND NON DESTRUCTIVE TEST.</p>	

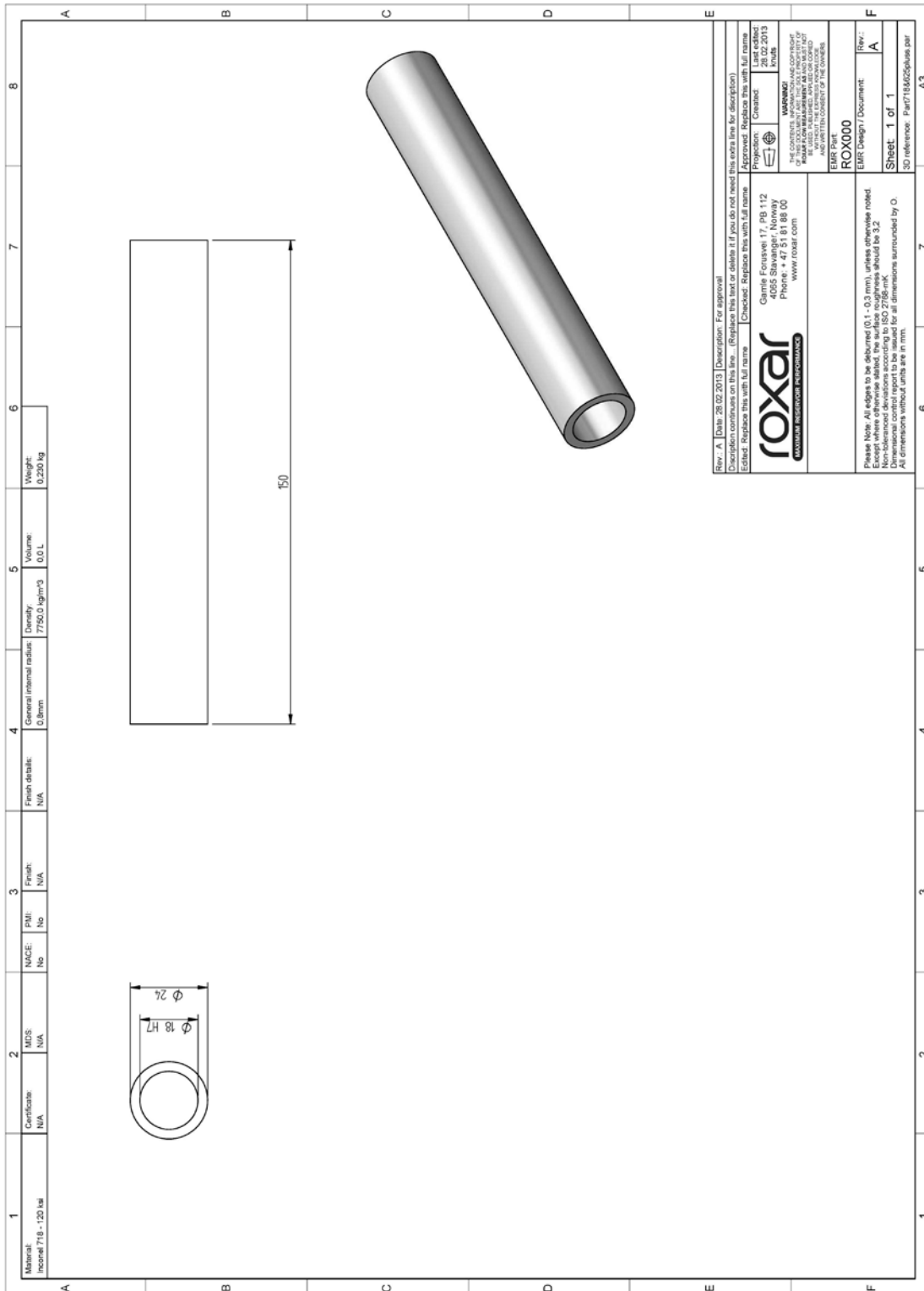
 <b>FORONI S.p.A.</b> 21055 Gorla Minore (VA) Italia		  		<b>CERTIFIED MATERIAL TEST REPORT</b> Inspection certificate EN 10204-3.1		Cert. n° 2011/1009 Rev. 0 Date 27/4/2011			
Customer Material: CUS IOM AGE 625 PLUS; UNS N07716; AF7716.		Order n°: 10 805 + Order confirmation Delivery condition: Hot worked, solution annealed, aged and peeled.		Item: 3					
Specifications: CMS-ZINGK.0 Rev.A; NACE MR0175/ISO 15156-3:2003/Cor.1:2005/Cor.2:2005/Cir.1:2007/Cir.2:2008; ES-MA-109-1 Rev.A.		Heat Treatment: Lot n°: 6967 CTT n°: 6967 - Solution annealing at 1900°F x 2 hrs 35' - water quench; - Age hardening at 1350°F x 7 hrs, furnace cool to 1150°F and held for 7 hrs - air cooling. See remarks?		Description: R.P. Bars N° of pieces: 4 Weight: 5545 Lbs Size: 5,00 inches Bar identification: 1 to 4 Forging ratio: 22.1		Length: see annex B.			
<b>Chemical analysis</b> % W Heat Product C 0,015 MN 0,07 SI 0,14 CR 20,84 NI 61,79 MO 8,09 S 0,0033 P 0,011 CU 0,04 AL 0,19 TI 1,20 B 0,0020 PB <0,0005 FE Balance NB+TA 3,40		<b>Mechanical properties</b> Test n° 2044 See remarks 1 Type M.R. Position L.N.G. Direction Temperature °F 68 Y.S. 0,2% KSI 135,5 U.T.S. 1% KSI 180,0 Elongation % 40 31,9 Red. of Area % 48,3 Hardness HB 38 HRC 39 to 41 (to ES-I-125 Rev E) Position M.R. Direction TRV Temperature °F -76 Charpy A FLLbs 41 37 Lateral expansion inches 0,016 0,020 Shear % 100 100 Temperature °F Load Ksi Load Increm. Duration hours Elongation %		<b>Tensile properties</b> HRC values S1 = 38 MR1 = 38 S2 = 37 MR2 = 38 S3 = 39 MR3 = 38		<b>Other properties</b> Specification: ASTM E112-96 Comparison method Results: 6 Predominant Grain size to Test sample hardness measurements to ASTM A370-09a method ASTM E18-08b Surface hardness testings (S1-S2-S3) performed on a smooth, clean flat to avoid work-hardening effect. Macro examination Microstructure test Inclusional content Hamilton Metals, Inc QC: EM Spec: 625 Plus RR: 7948-3 Date: 05/26/11 NDE-31 Rev AL Passed API 6A, 19th Ed. Passed PSL3 (Par. 7.4.2.3.15) Passed Dimensional check Passed P.M.I. check Passed Fatigue testing Passed		Remarks: - 1 Mechanical properties determined on specimens removed from a bar prolongation after completion of all processing; tensile test on standard 0,500 inch diameter specimen. - 2 Furnace calibration and survey in accordance with AMS 2750D.	
Material made in Italy.		No welds, no mercury and radioactive contamination.		Quality System Manual MSC Ed. 2003 Rev. 3		S.C.O. Department M. Gallina H. Gallina R.S.Q. Inspector			
The material is in compliance with the mentioned specifications. Material produced according to the Quality System described in the FORONI S.p.A. MSQ Manual.									

Fully or partial reproduction of this document without a written approval by FORONI S.p.A. is forbidden.

# Appendix B: Schematic Drawings of Specimen Components

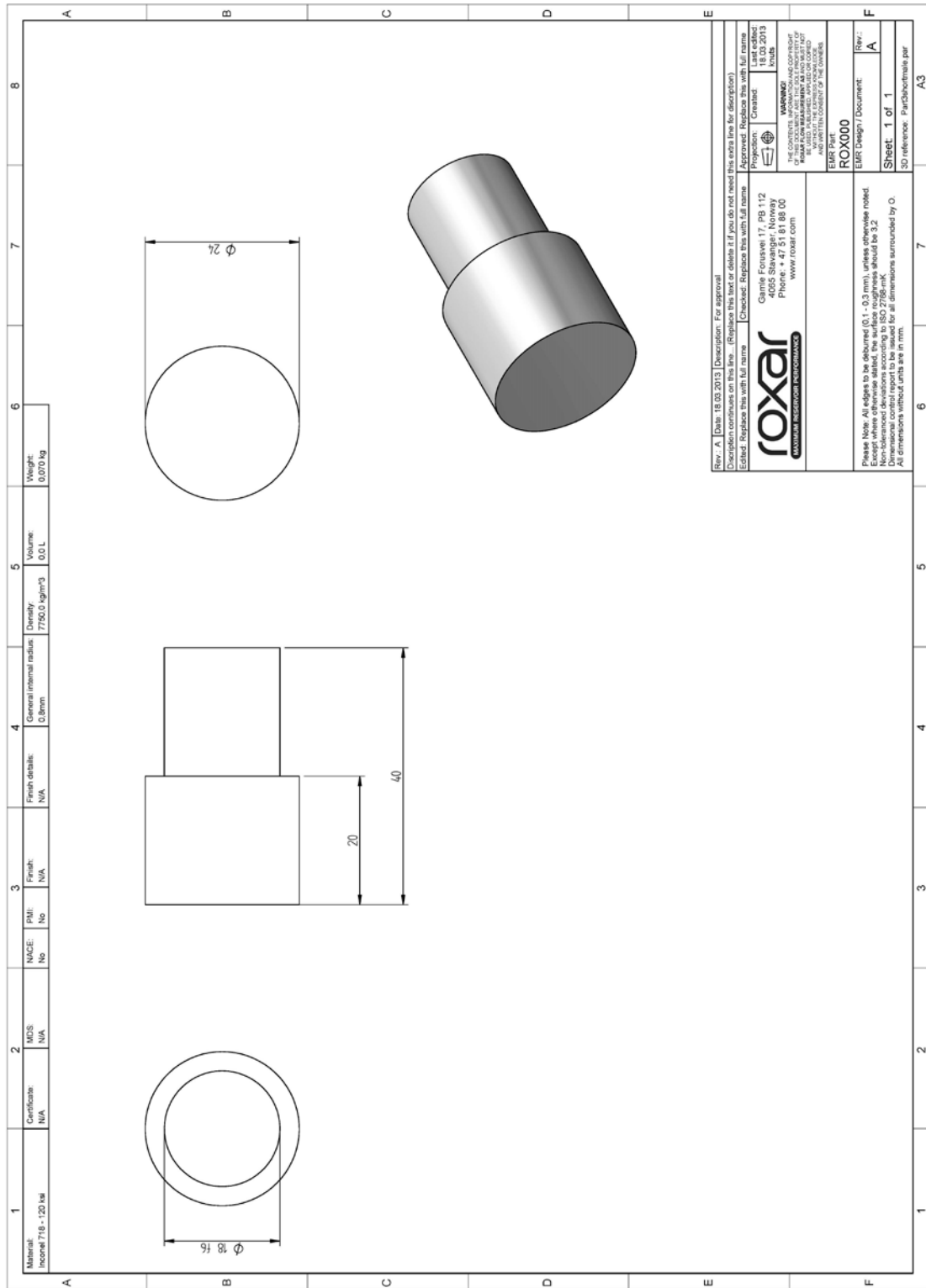
## Tensile Specimen Components



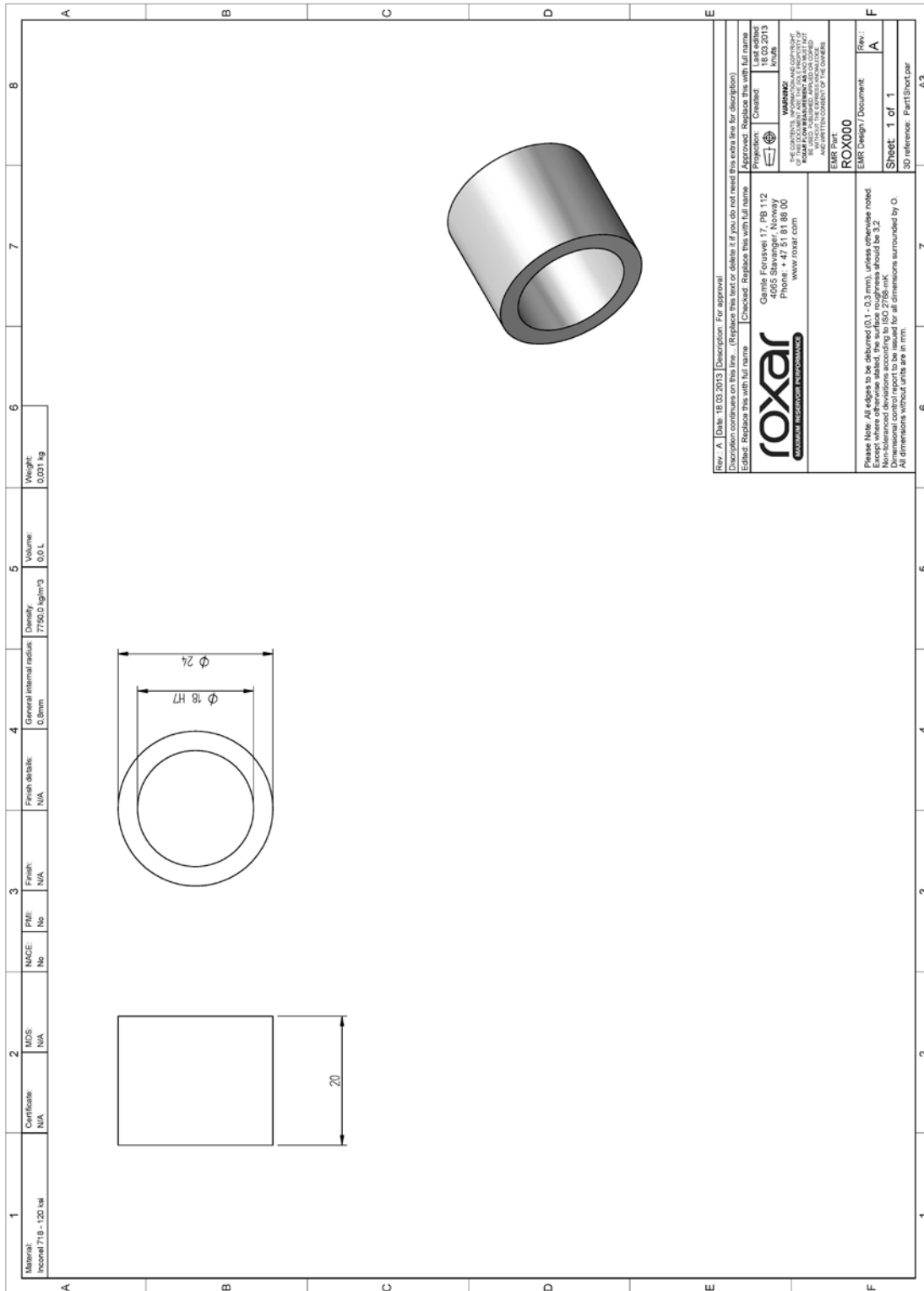


Rev: A   Date: 28.02.2013   Description: For approval Description continues on this line. (Replace this text or delete it if you do not need this extra line for description) Edited: Replace this with full name Checked: Replace this with full name	Approved: Replace this with full name Projection: Created List edited: 28.02.2013 User: knud	EIMR Part: <b>ROX000</b> EIMR Design / Document: <b>ROX000</b>
<p style="text-align: center;"><b>roxar</b></p> <p style="text-align: center; font-size: small;">MINIMUM PERFORMANCE</p>		EIMR Part: <b>ROX000</b> EIMR Design / Document: <b>ROX000</b>
Company: Eimsvægt 17, PB 112 4055 Stavanger, Norway Phone: + 47 51 81 88 00 www.roxar.com		Please Note: All edges to be deburred (0.1 - 0.3 mm), unless otherwise noted. Except where otherwise stated, the surface roughness should be 3.2. Dimensions are given in millimeters. All dimensions are in mm. Dimensional control report to be issued for all dimensions surrounded by O.
<p style="text-align: center; font-size: x-small;"> <b>WARNING!</b>          THIS DOCUMENT IS THE PROPERTY OF ROXAR AS.          IT IS TO BE USED ONLY FOR THE PROJECT AND FOR THE PARTS LISTED THEREIN.          ALL RIGHTS ARE RESERVED. UNAUTHORIZED REPRODUCTION OR DISTRIBUTION IS PROHIBITED.          AND WITHOUT LIABILITY OF THE OWNERS.       </p>		Rev.: <b>A</b> Sheet: 1 of 1 3D reference: Part718&025plate.pdf

# Corrosion Specimen Components







# Appendix C: Fractographic Examination

## Fracture Paths

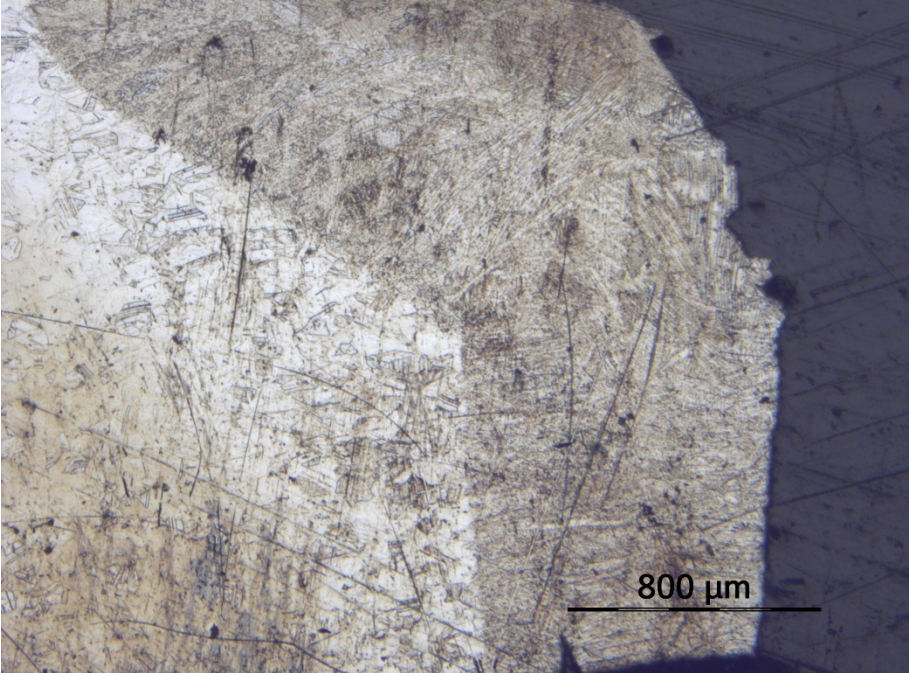


Figure C-1: Inconel 718 No. 1.

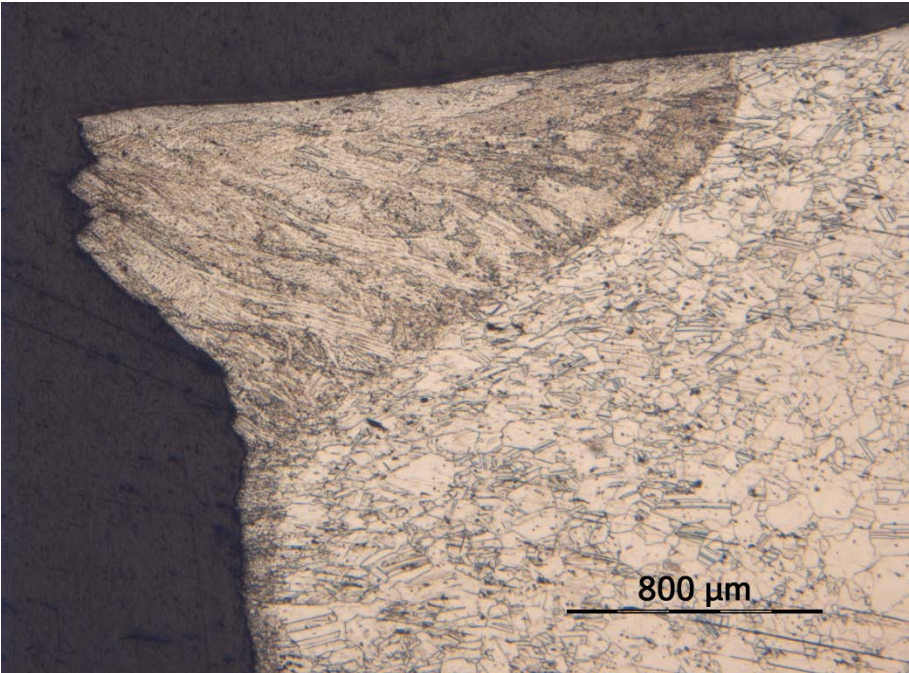
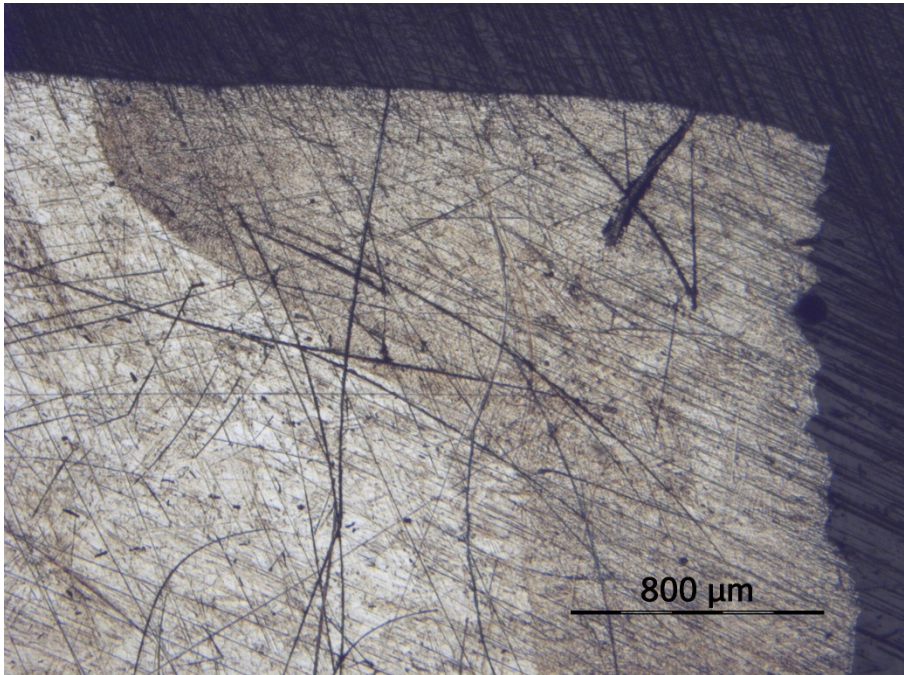
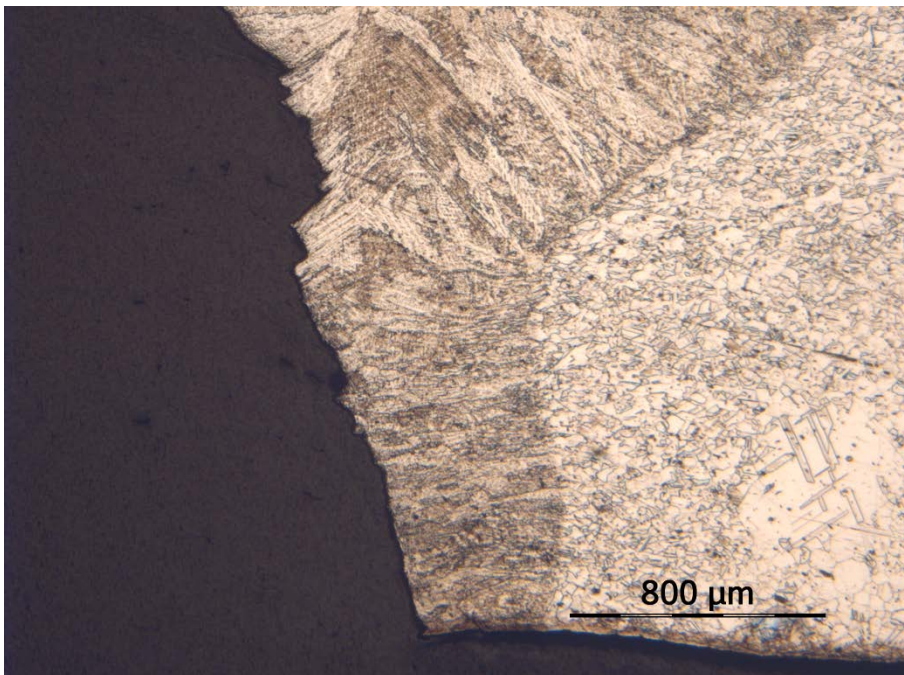


Figure C-2: Inconel 718 No. 2.



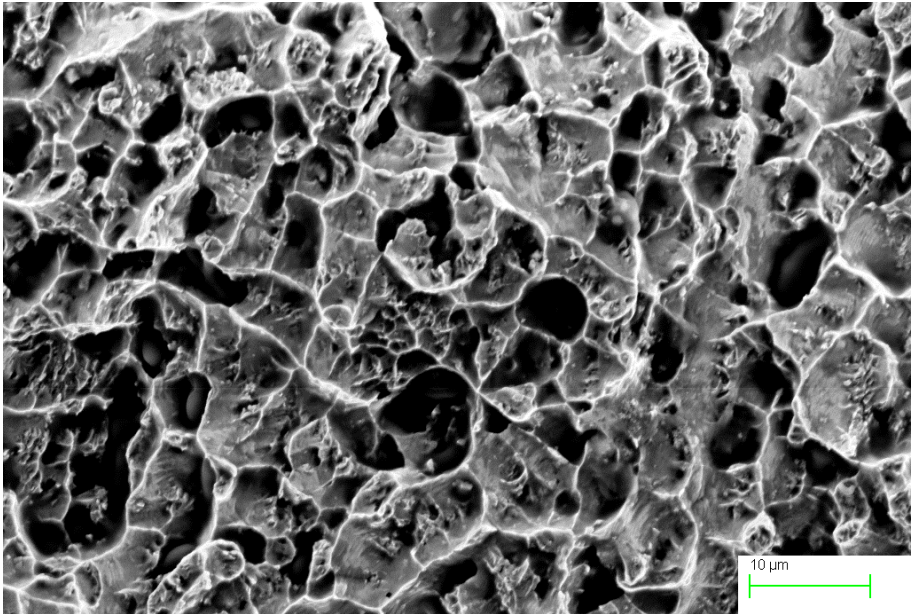


*Figure C-3: 625 PLUS No. 1.*

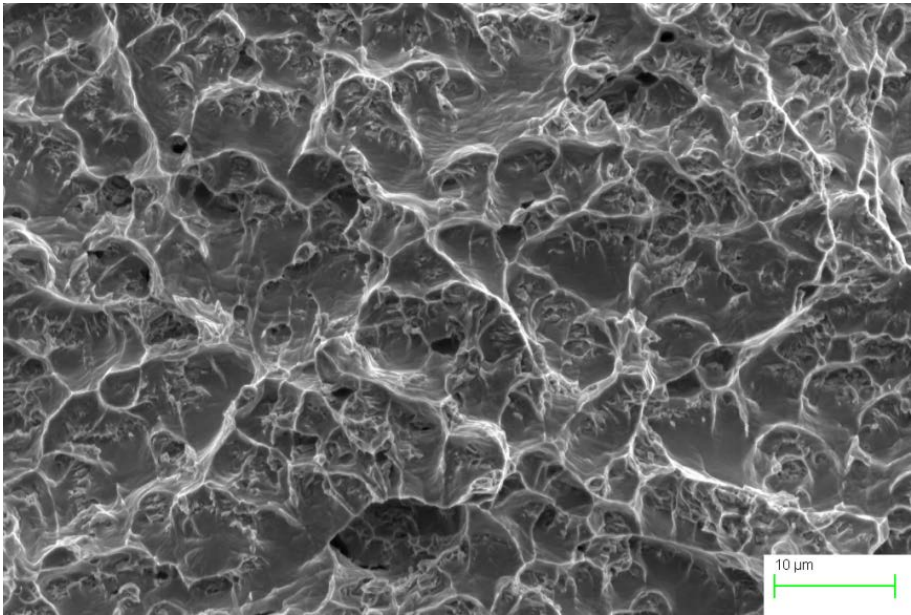


*Figure C-4: 625 PLUS No. 2.*

**Fractographs**

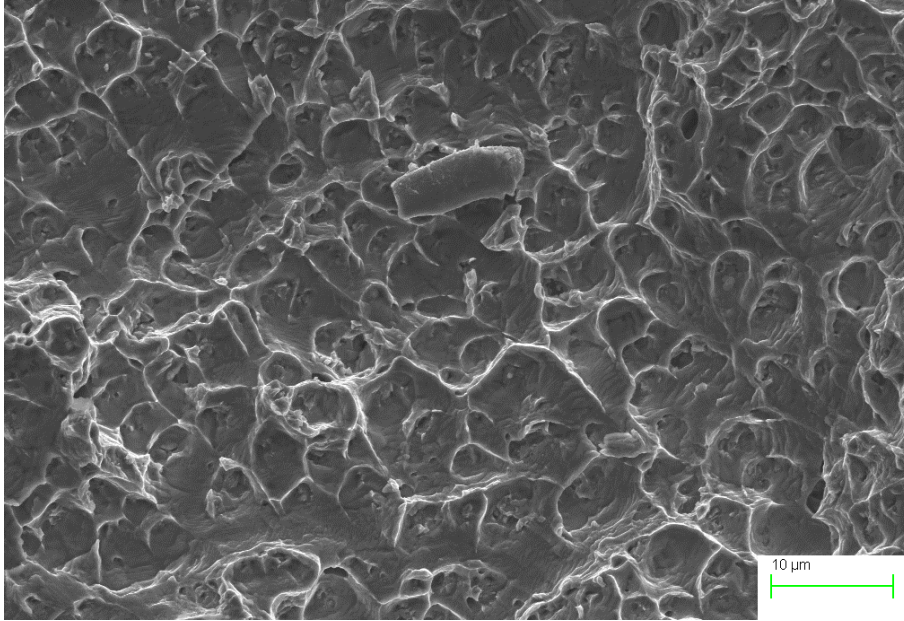


*Inconel 718 No.1*

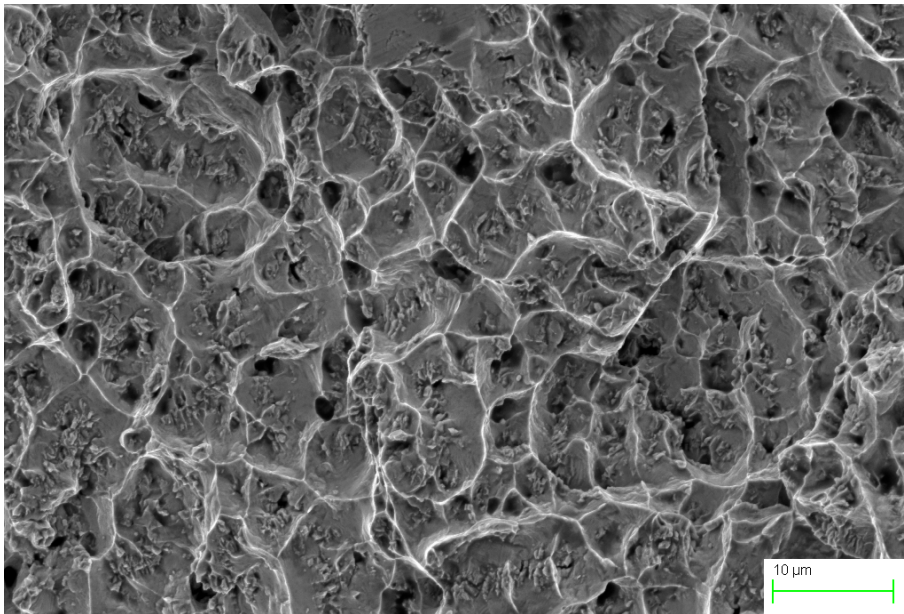


*Inconel 718 No.2*





*625 PLUS No. 1*



*625 PLUS No. 2*

**Appendix D: Microstructural Analysis**

**Inconel 718**

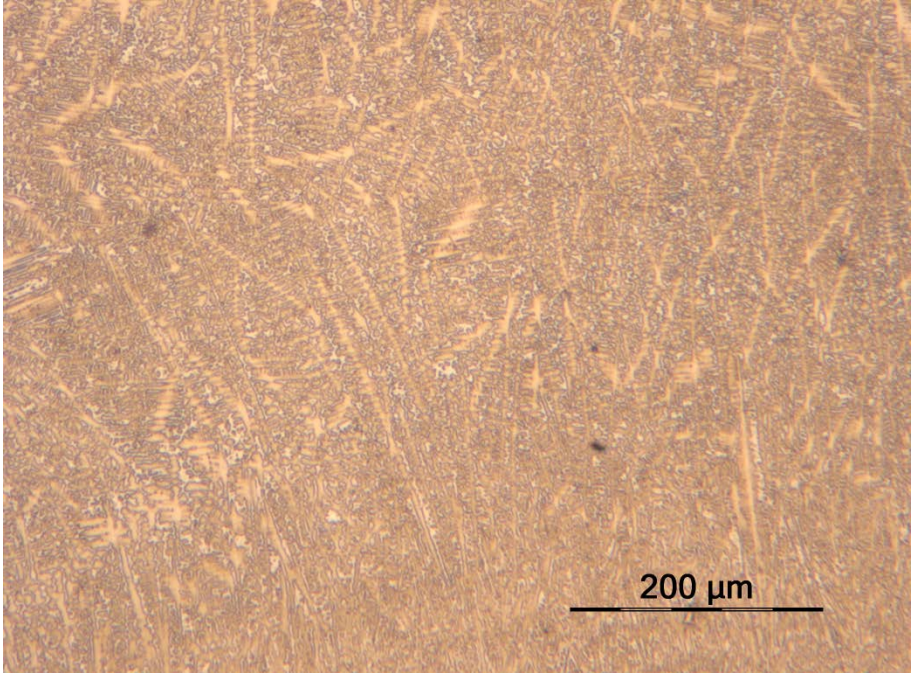


*Figure D-1: Inconel 718 No. 4 weld metal. 10% Chromic Acid.*

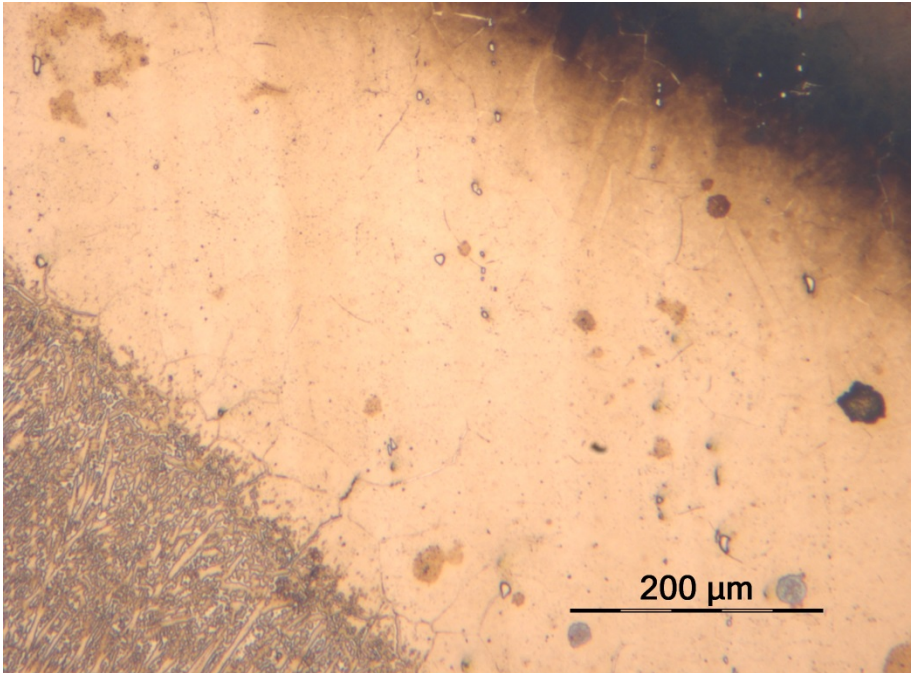


*Figure D-2: Inconel 718 No. 4 HAZ. 10% Chromic Acid.*



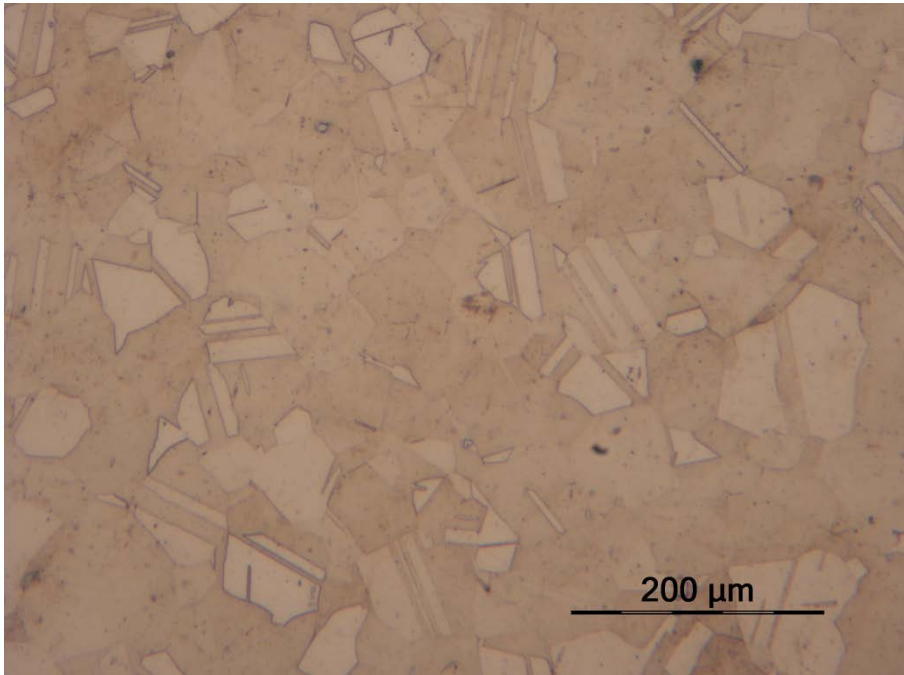


*Figure D-3: Inconel 718 No. 3 base metal. Kalling's No. 2.*

**625 PLUS**

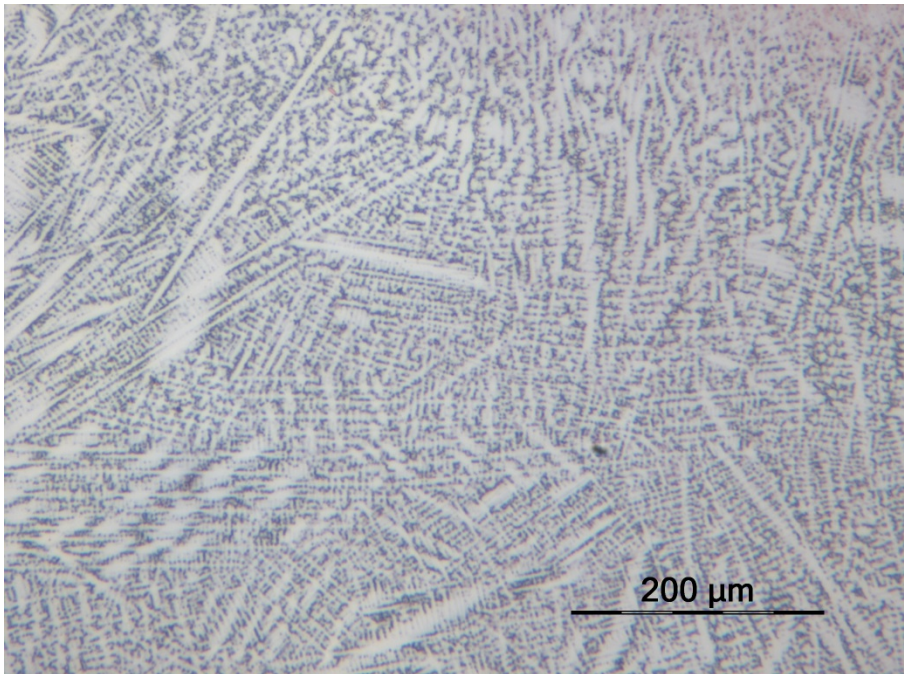


*Figure D-4: 625 PLUS No. 4 weld metal. 10% Chromic Acid.*

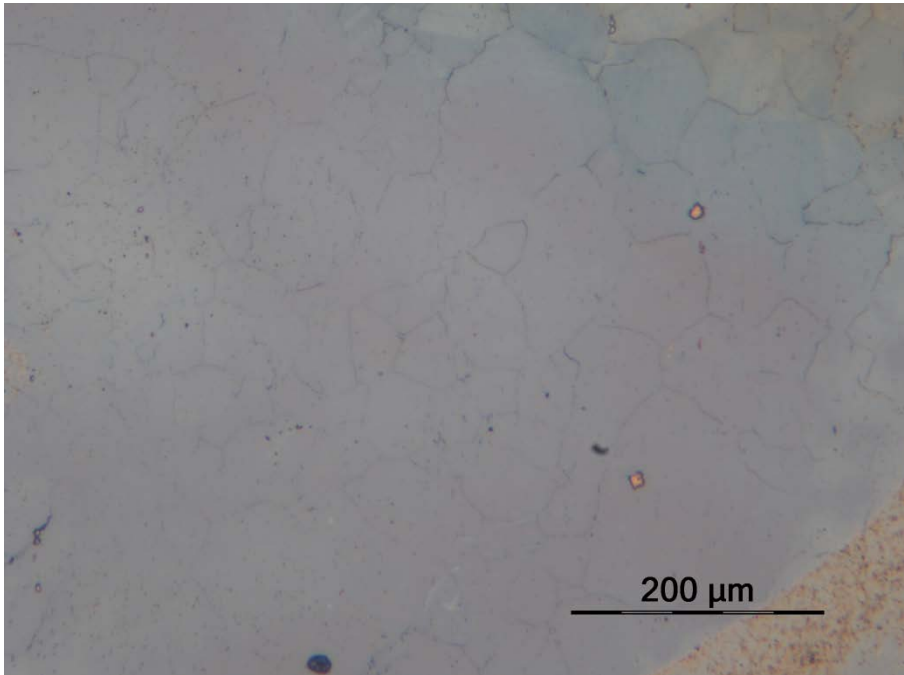


*Figure D-5: 625 PLUS No. 4 HAZ. 10% Chromic Acid.*

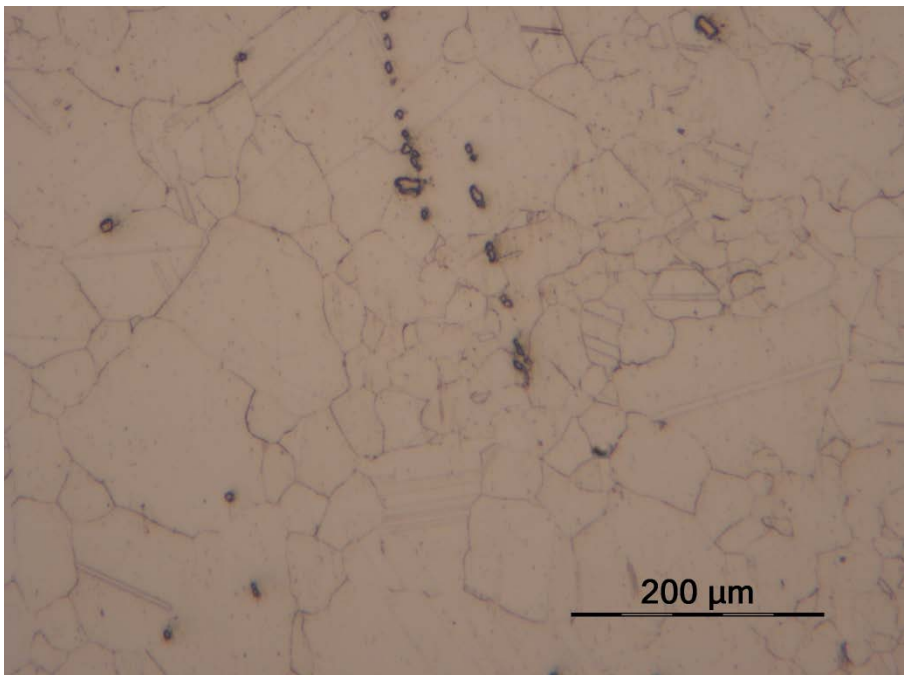


*Figure D-6: 625 PLUS No. 3. Kalling's No. 2.*



### Appendix E: Vickers Hardness Measurements

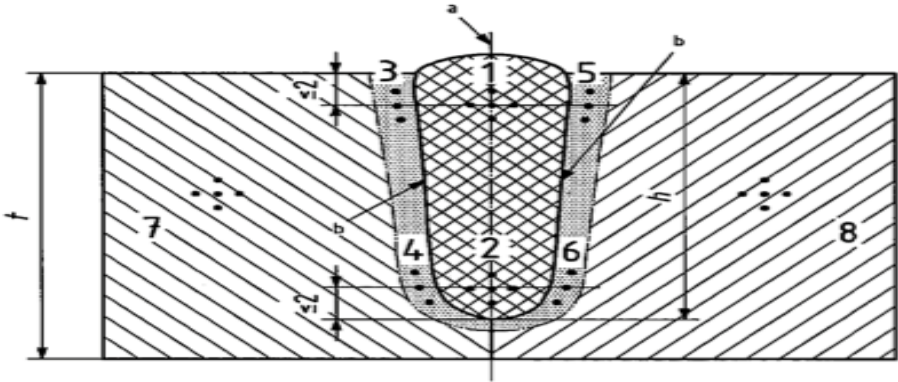


Table E-1: Harness measurements of as-welded alloys.

Zone	Position of indentations	Inconel 718		625 PLUS	
		Average	Standard Deviation	Average	Standard Deviation
1	Weld Metal, Top	231.0 HV	10.0	237.1 HV	8.2
2	Weld Metal, Bottom	263.4 HV	11.7	267.0 HV	12.0
3	HAZ, Top	221.0 HV	5.7	229.8 HV	9.2
4	HAZ, Bottom	226.5 HV	20.8	227.2 HV	10.1
5	HAZ, Top	216.3 HV	10.2	249.2 HV	10.1
6	HAZ, Bottom	219.6 HV	8.5	263.3 HV	11.4
7	Base Metal	389.0 HV	10.8	392.9 HV	18.2
8	Base Metal	401.5 HV	12.5	396.5 HV	7.1

Table E-2: Hardness measurements of post-weld heat treated alloys.

Zone	Position of indentations	Inconel 718		625 PLUS	
		Average	Standard Deviation	Average	Standard Deviation
1	Weld Metal, Top	385.4 HV	36.3	347.3 HV	15.3
2	Weld Metal, Bottom	413.3 HV	14.4	354.8 HV	19.5
7	Base Metal	392.1 HV	9.1	343.0 HV	14.2
8	Base Metal	401.6 HV	13.6	336.0 HV	14.7

\*Note that measurements in the former HAZ are neglected as the interface between the weld metal and HAZ was hard to observe. Measurements of the HAZ were not thought to be particularly relevant.